



Calhoun: The NPS Institutional Archive
DSpace Repository

Theses and Dissertations

1. Thesis and Dissertation Collection, all items

2002-06

A multidisciplinary algorithm for the 3-D design optimization of transonic axial compressor blades

Jones, James A.

Monterey, California: Naval Postgraduate School

<http://hdl.handle.net/10945/9780>

This publication is a work of the U.S. Government as defined in Title 17, United States Code, Section 101. Copyright protection is not available for this work in the United States.

Downloaded from NPS Archive: Calhoun



<http://www.nps.edu/library>

Calhoun is the Naval Postgraduate School's public access digital repository for research materials and institutional publications created by the NPS community. Calhoun is named for Professor of Mathematics Guy K. Calhoun, NPS's first appointed -- and published -- scholarly author.

Dudley Knox Library / Naval Postgraduate School
411 Dyer Road / 1 University Circle
Monterey, California USA 93943

NAVAL POSTGRADUATE SCHOOL
Monterey, California



DISSERTATION

**A MULTIDISCIPLINARY ALGORITHM FOR THE 3-D
DESIGN OPTIMIZATION OF TRANSONIC AXIAL
COMPRESSOR BLADES**

by

James A. Jones, Jr.

June 2002

Dissertation Supervisor: Raymond P. Shreeve

Approved for public release; Distribution is unlimited

THIS PAGE INTENTIONALLY LEFT BLANK

REPORT DOCUMENTATION PAGE			<i>Form Approved OMB No. 0704-0188</i>	
Public reporting burden for this collection of information is estimated to average 1 hour per response, including the time for reviewing instruction, searching existing data sources, gathering and maintaining the data needed, and completing and reviewing the collection of information. Send comments regarding this burden estimate or any other aspect of this collection of information, including suggestions for reducing this burden, to Washington headquarters Services, Directorate for Information Operations and Reports, 1215 Jefferson Davis Highway, Suite 1204, Arlington, VA 22202-4302, and to the Office of Management and Budget, Paperwork Reduction Project (0704-0188) Washington DC 20503.				
1. AGENCY USE ONLY (Leave blank)		2. REPORT DATE June 2002	3. REPORT TYPE AND DATES COVERED Dissertation	
4. TITLE AND SUBTITLE: Title (Mix case letters) A Multidisciplinary Algorithm for the 3-D Design Optimization of Transonic Axial Compressor Blades			5. FUNDING NUMBERS	
6. AUTHOR(S) CDR James A. Jones, Jr., USN				
7. PERFORMING ORGANIZATION NAME(S) AND ADDRESS(ES) Naval Postgraduate School Monterey, CA 93943-5000			8. PERFORMING ORGANIZATION REPORT NUMBER	
9. SPONSORING / MONITORING AGENCY NAME(S) AND ADDRESS(ES) N/A			10. SPONSORING / MONITORING AGENCY REPORT NUMBER	
11. SUPPLEMENTARY NOTES The views expressed in this thesis are those of the author and do not reflect the official policy or position of the Department of Defense or the U.S. Government.				
12a. DISTRIBUTION / AVAILABILITY STATEMENT Approved for public release; distribution is unlimited.			12b. DISTRIBUTION CODE	
13. ABSTRACT (maximum 200 words) A new, multidisciplinary algorithm for the CFD design optimization of turbomachinery blades is presented. It departs from existing techniques in that it uses a simple, previously-developed Bezier geometry representation (BLADE-3D) that can be easily manipulated to achieve true 3-D changes in blade shape. The algorithm incorporates zero and first-order optimization techniques including sensitivity analyses and one-dimensional search methodology. It features an iterative finite element structural analysis as well as a cold shape correction procedure to ensure that the resulting blade meets steady-stress structural requirements. The process was applied to two different transonic fan designs – the Sanger rotor designed for the NPS Turbomachinery Laboratory and NASA Rotor 67, otherwise known as the ‘NASA Fan’. The optimization objectives for the two designs were mass flow rate and polytropic efficiency respectively. Results for the Sanger rotor effort yielded an 8.1 % improvement in mass flow rate, a 5% improvement in total pressure ratio, and a 0.9 % increase in adiabatic efficiency. Application to the NASA Fan resulted in a 2.5 % increase in polytropic efficiency. The results validate the utility of the BLADE-3D Bezier geometry package for use in future development of automated optimization routines for turbomachinery blade design.				
14. SUBJECT TERMS Design Optimization, Transonic Fan Blades, Bezier Geometry Package			15. NUMBER OF PAGES 164	
			15. PRICE CODE	
17. SECURITY CLASSIFICATION OF REPORT Unclassified	18. SECURITY CLASSIFICATION OF THIS PAGE Unclassified	19. SECURITY CLASSIFICATION OF ABSTRACT Unclassified	20. LIMITATION OF ABSTRACT UL	

THIS PAGE INTENTIONALLY LEFT BLANK

Approved for public release; distribution is unlimited

**A MULTIDISCIPLINARY ALGORITHM FOR THE 3-D DESIGN OPTIMIZATION
OF TRANSONIC AXIAL COMPRESSOR BLADES**

James A. Jones, Jr.
Commander, United States Navy
B.S., United States Naval Academy, 1978
M.S., United States Naval Postgraduate School, 1985

Submitted in partial fulfillment of the
requirements for the degree of

DOCTOR OF PHILOSOPHY IN AERONAUTICS AND ASTRONAUTICS

from the

**NAVAL POSTGRADUATE SCHOOL
June 2002**

Author:

James A. Jones, Jr.

Approved by:

Raymond P. Shreeve
Professor of Aeronautics
and Astronautics
Dissertation Supervisor

Garth. V. Hobson
Professor of Aeronautics
and Astronautics

Max. F. Platzer
Distinguished Professor
of Aeronautics and
Astronautics

Richard M. Howard
Associate Professor of
Aeronautics and Astronautics

Carlos Borges
Associate Professor of Mathematics

Approved by:

Max. F. Platzer, Chair, Department of Aeronautics and Astronautics

Approved by:

Carson K. Eoyang, Associate Provost for Academic Affairs

THIS PAGE INTENTIONALLY LEFT BLANK

ABSTRACT

A new, multidisciplinary algorithm for the CFD design optimization of turbomachinery blades is presented. It departs from existing techniques in that it uses a simple, previously-developed Bezier geometry representation (BLADE-3D) that can be easily manipulated to achieve true 3-D changes in blade shape. The algorithm incorporates zero and first-order optimization techniques including sensitivity analyses and one-dimensional search methodology. It features an iterative finite element structural analysis as well as a cold shape correction procedure to ensure that the resulting blade meets steady-stress structural requirements. The process was applied to two different transonic fan designs – the Sanger rotor designed for the NPS Turbomachinery Laboratory and NASA Rotor 67, otherwise known as the ‘NASA Fan’. The optimization objectives for the two designs were mass flow rate and polytropic efficiency respectively. Results for the Sanger rotor effort yielded an 8.1 % improvement in mass flow rate, a 5% improvement in total pressure ratio, and a 0.9 % increase in adiabatic efficiency. Application to the NASA Fan resulted in a 2.5 % increase in polytropic efficiency. The results validate the utility of the BLADE-3D Bezier geometry package for use in future development of automated optimization routines for turbomachinery blade design.

THIS PAGE INTENTIONALLY LEFT BLANK

TABLE OF CONTENTS

I.	INTRODUCTION.....	1
II.	BACKGROUND.....	5
A.	BASIC CONCEPT	5
B.	OVERVIEW OF CURRENT DESIGN PROCESS	6
C.	HISTORICAL PERSPECTIVE	7
D.	NEWER DEVELOPMENTS	12
1.	Sweep.....	12
2.	CFD and Design Optimization	13
3.	3-D Inverse Methods.....	13
4.	Multidisciplinary Design Optimization (MDO)	14
III.	RESOURCES	15
A.	BLADE-3D – THE ABDELHAMID BEZIER GEOMETRY PACKAGE.....	15
B.	THE SANGER ROTOR.....	20
C.	NASA ROTOR 67.....	21
D.	RESEARCH TOOLS	22
1.	Grid Generator – TCGRID.....	22
2.	Flow Analysis Code – RVC3D.....	23
3.	Flow Visualization Software – FAST	24
4.	Structural Analysis Tools	24
a.	<i>Initial Graphics Exchange Specification – IGES 5.3.....</i>	<i>24</i>
b.	<i>I-DEAS Master Series Six</i>	<i>24</i>
IV.	METHODOLOGY.....	25
A.	OVERVIEW	25
B.	ADAPTATION OF BLADE-3D	25
C.	IMPLEMENTATION OF CFD TOOLS AND PROCEDURES.....	28
D.	AERODYNAMIC OPTIMIZATION PROCEDURE	31
1.	Random Variation of Control Points	31
2.	Effect of Forward and Aft Sweep	35
3.	One-dimensional Search Technique.....	37
a.	<i>Pressure and Suction Side Control Points</i>	<i>37</i>
b.	<i>Forward Sweep.....</i>	<i>45</i>
F.	STRUCTURAL ANALYSIS.....	47
1.	Finite Element Analysis.....	47
2.	Cold Shape Correction.....	49
G.	ROTOR 67	52
H.	OPTIMIZATION ALGORITHM	55
V.	RESULTS AND DISCUSSION.....	59
A.	THE SANGER ROTOR.....	59
1.	Overview	59
2.	Performance.....	60
3.	Geometry.....	63

4.	The Flow Field	70
5.	Structural Comparison	80
B.	ROTOR 67	82
1.	Overview	82
2.	Performance.....	84
3.	Geometry.....	86
4.	The Flow Field	91
5.	Structural Comparison	103
a.	<i>Finite Element Analysis</i>	103
b.	<i>Cold Shape Correction</i>	104
VI.	CONCLUSIONS.....	107
VII.	RECOMMENDATIONS.....	109
	APPENDIX A. MODAL ANALYSIS AND FLUTTER	111
	APPENDIX B. CALCULATION OF BASIC PARAMETERS.....	117
1.	Pressure Ratio, Mass Flow Rate and Efficiency.....	117
3.	Chord Angle, Camber Angle, Incidence and Deviation Angles..	118
3.	Blade Thickness	120
	APPENDIX C. OPTIMIZATION THEORY AND TECHNIQUE	123
	APPENDIX D. MERIDL VS. BLADE-3D	127
	APPENDIX E. INPUT FILES.....	131
1.	TCGRID.....	131
2.	RVC3D	131
3.	I-DEAS (IGES 5.3).....	132
	APPENDIX F. RVC3D OUTPUT.....	133
	APPENDIX G. COMPUTER PROGRAMS	149
	LIST OF REFERENCES.....	157
	INITIAL DISTRIBUTION LIST	163

LIST OF FIGURES

Figure 1. Velocity Changes Across a Transonic Rotor.....	5
Figure 2. Stream Surfaces in a Turbomachine (From Ref. 5).....	8
Figure 3. Throughflow Analysis Framework (After Ref. 4).....	9
Figure 4. Blade-to-Blade Stream Surface	10
Figure 5. Bezier Curve with Convex Hull (After Ref. 1).....	16
Figure 6. Subdivision of Bezier Curves (After Ref. 1)	17
Figure 7. Bezier Surface with Control Point Net (After Ref. 1)	18
Figure 8. Bezier Representation of Compressor Blade (After Ref. 1).....	19
Figure 9. The Sanger Rotor (From Ref. 3).....	21
Figure 10. NASA Rotor 67	22
Figure 11. Leading Edge Detail of a Computational C-Grid from TCGRID	23
Figure 12. Effect of Leading Edge Parameter Change	27
Figure 13. Effect of Subdivision Applied to the Pressure Surface	28
Figure 14. Moveable Control Points	32
Figure 15. Example – Random Variation of Suction Surface Control Points	33
Figure 16. Example – Random Variation of Pressure Surface Control Points	34
Figure 17. Sweep Manipulation in BLADE-3D	35
Figure 18. Effect of Sweep – Sweep 1	36
Figure 19. Effect of Sweep – Sweep 2.....	36
Figure 20. Pressure Side Radial Optimization	38
Figure 21. Sanger Rotor – Optimization Run 1	40
Figure 22. Sanger Rotor – Optimization Run 2	41
Figure 23. Sanger Rotor – Optimization Run 3	42
Figure 24. Sanger Rotor – Lack of Thickness during Run 3	43
Figure 25. Sanger Rotor – Optimization Run 4	44
Figure 26. Sanger Rotor – Optimization of Sweep	46
Figure 27. Solid Modeling of Sanger Blade with I-DEAS	48
Figure 28. Blade Iterations during Cold Shape Correction.....	51
Figure 29. Rotor 67 – Suction Side Control Point Optimization	53
Figure 30. Rotor 67 – Optimization of Sweep	54
Figure 31. The Optimization Algorithm	56

Figure 32. Sanger Rotor Performance.....	61
Figure 33. Sanger Rotor Efficiency	61
Figure 34. Sanger Rotor Geometry – Hub	63
Figure 35. Sanger Rotor Geometry – 30% Span.....	64
Figure 36. Sanger Rotor Geometry – 70% Span.....	64
Figure 37. Sanger Rotor Geometry – Tip.....	65
Figure 38. Sanger Rotor – Chord Angle	66
Figure 39. Sanger Rotor – Camber Angle.....	67
Figure 40. Sanger Rotor – Maximum Thickness Distribution	67
Figure 41. Sanger Rotor – Maximum Thickness Location	68
Figure 42. Sanger Rotor – Minimum Thickness Distribution.....	68
Figure 43. Sanger Rotor – Minimum Thickness Location.....	69
Figure 44. Sanger Rotor – Absolute Inlet Mach Number	71
Figure 45. Sanger Rotor – Relative Inlet Mach Number	71
Figure 46. Sanger Rotor – Total Pressure Ratio	72
Figure 47. Sanger Rotor – Total Temperature Ratio.....	72
Figure 48. Sanger Rotor – Adiabatic Efficiency	73
Figure 49. Sanger Rotor – Absolute Exit Mach Number.....	73
Figure 50. Sanger Rotor – Exit Relative Mach Number	74
Figure 51. Sanger Rotor – Incidence Angle.....	74
Figure 52. Sanger Rotor – Deviation Angle.....	75
Figure 53. Sanger Rotor – Geometry and Mach Number Distribution.....	77
Figure 54. Sanger Rotor – Mach Contours near the Hub.....	78
Figure 55. Sanger Rotor – Mach Contours at 30% Span	78
Figure 56. Sanger Rotor – Mach Contours at Midspan	79
Figure 57. Sanger Rotor – Mach Contours at 70% Span	79
Figure 58. Sanger Rotor – Mach Contours near the Tip	79
Figure 59. Sanger Rotor – Structural Analysis, Baseline Blade	81
Figure 60. Structural Analysis, Optimized Blade	81
Figure 61. Rotor 67 Performance.....	84
Figure 62. Rotor 67 Efficiency	85
Figure 63. Rotor 67 Geometry – Hub	86
Figure 64. Rotor 67 Geometry – 30% Span.....	87

Figure 65. Rotor 67 Geometry – 70% Span.....	87
Figure 66. Rotor 67 Geometry – Tip.....	88
Figure 67. Rotor 67 – Chord Angle	89
Figure 68. Rotor 67 – Camber Angle.....	89
Figure 69. Rotor 67 – Maximum Thickness Distribution	90
Figure 70. Rotor 67 – Maximum Thickness Location	90
Figure 71. Rotor 67 – Minimum Thickness Distribution.....	91
Figure 72. Rotor 67 – Absolute Inlet Mach Number	92
Figure 73. Rotor 67 – Relative Inlet Mach Number	92
Figure 74. Rotor 67 – Total Pressure Ratio.....	93
Figure 75. Rotor 67 – Total Temperature Ratio.....	93
Figure 76. Rotor 67 – Adiabatic Efficiency	94
Figure 77. Rotor 67 – Absolute Exit Mach Number	94
Figure 78. Rotor 67 – Exit Relative Mach Number	95
Figure 79. Rotor 67 – Incidence Angle.....	95
Figure 80. Rotor 67 – Deviation Angle.....	96
Figure 81. Rotor 67 – New vs. Baseline, Geometry and Mach Number Distribution	97
Figure 82. Rolls Royce Commercial Fan Blade (From Ref. 4)	98
Figure 83. Rotor 67 – New vs. Baseline, Mach Contours near the Hub	98
Figure 84. Rotor 67 – New vs. Baseline, Mach Contours at 30% Span	99
Figure 85. Rotor 67 – New vs. Baseline, Mach Contours at Midspan.....	99
Figure 86. Rotor 67 – New vs. Baseline, Mach Contours at 70% Span	99
Figure 87. Rotor 67 – New vs. Baseline, Mach Contours near the Tip	100
Figure 88. Rotor 67 – Final vs. Baseline, Geometry and Mach Number Distribution	100
Figure 89. Rotor 67 – Final vs. Baseline, Mach Contours near the Hub	101
Figure 90. Rotor 67 – Final vs. Baseline, Mach Contours at 30% Span.....	101
Figure 91. Rotor 67 – Final vs. Baseline, Mach Contours at Midspan.....	102
Figure 92. Rotor 67 – Final vs. Baseline, Mach Contours at 70% Span.....	102
Figure 93. Rotor 67 – Final vs. Baseline, Mach Contours near the Tip.....	102
Figure 94. Rotor 67 – Structural Analysis, Baseline Blade	103
Figure 95. Rotor 67, Structural Analysis, Final Blade.....	104
Figure 96. Rotor 67 - Cold Shape Correction	105
Figure 97. Rotor 67 - Cold Shape Correction History	105

Figure 98. Sanger Rotor - First Engine Order.....	112
Figure 99. Sanger Rotor - 27th Engine Order.....	112
Figure 100. Rotor 67 – First Engine Order	112
Figure 101. Rotor 67 – 27 th Engine Order	113
Figure 102. Flutter Boundaries in an Axial Compressor (From Ref. 43)	114
Figure 103. Chord Angle (ζ).....	118
Figure 104. Camber Angle (ϕ).....	119
Figure 105. Incidence (i) and Deviation (δ) Angles	120
Figure 106. Calculation of Blade Thickness	121
Figure 107. Location of Maximum or Minimum Thickness (d).....	121
Figure 108. Finding the Search Distance (From Ref. 45).....	125
Figure 109. The One-Dimensional Search (From Ref. 45).....	125

LIST OF TABLES

Table 1. Sanger Rotor Design Summary.....	20
Table 2. Rotor 67 Design Summary.....	22
Table 3. Sanger Rotor Sweep Optimization Scheme	45
Table 4. Rotor 67 Sweep Optimization Scheme	54
Table 5. Sanger Rotor Optimization Summary.....	59
Table 6. Rotor 67 Optimization Summary.....	83
Table 7. Normal Modes and Frequencies	111

THIS PAGE INTENTIONALLY LEFT BLANK

ACKNOWLEDGMENTS

The completion of this research effort represents the end of a long, difficult and at times exhausting journey, one that has occupied my thoughts and dreams almost exclusively for the last two years. I certainly could not have made it without the help and support of many special people. First, I would like to thank my advisor, Professor Ray Shreeve, for his guidance, advice and consistently wise counsel. It has been a true pleasure to work closely with him and I look forward to doing so in the future. I thank the other members of my committee, Professors Platzer, Hobson, Howard and Borges, for their willingness to participate in my research program and for their countless valuable suggestions during the process. I especially appreciate their upbeat and positive attitudes which have made the entire experience a very positive one for me. In addition, I would like to thank Professor Knox Millsaps from the NPS Mechanical Engineering Department, as well as Tony Strasizar and Mike Ernst from NASA Glenn for their help in understanding the structural aspects of compressor blade design. And of course, special thanks to Major Hazem Abdelhamid of the Egyptian Air Force for creating the geometry package used to carry out this study.

I would like to thank my family and friends for their ever-present love and support. My mother, parents-in-law, uncles, aunts, and cousins have all been cheerleaders during the process and have helped ensure that my motivation and morale remained high. Last but definitely not least, I thank my beautiful wife Elizabeth and my young son Max; their special brand of love, devotion, understanding, and perseverance has made this effort possible. They are the lights of my life and it is with the greatest love, pride and respect that I dedicate this work to them.

THIS PAGE INTENTIONALLY LEFT BLANK

EXECUTIVE SUMMARY

A new, multidisciplinary algorithm for the design optimization of turbomachinery blades is presented. It departs from existing techniques in that it uses a simple, previously-developed Bezier geometry representation (BLADE-3D) that can be easily manipulated to achieve true 3-D changes in blade shape. First, state-of-the-art 3-D computational fluid dynamics code is utilized to evaluate changes in blade aerodynamic performance with small changes in certain shape parameters chosen to maximize a given objective function – mass flow rate, efficiency, etc. The results of this analysis are then applied repeatedly to achieve maximum improvement in the chosen function within specified limits of constraining parameters in accordance with traditional optimization methodology. The algorithm incorporates an iterative finite element structural analysis as required to keep the optimization process from exceeding defined physical, stress and deflection limits. Once an aerodynamically optimized blade shape is achieved, a cold shape correction procedure is performed and a final stress analysis conducted to ensure that the resulting blade meets steady-stress structural requirements. Dynamic analysis and flutter prediction procedures are not included but are recommended for future incorporation. The process was applied to two different transonic fan designs – the compact Sanger rotor developed for use in the NPS Turbomachinery Laboratory and the larger, more highly-cambered NASA Rotor 67, otherwise known as the ‘NASA Fan’. The optimization objectives for the two designs were mass flow rate and polytropic efficiency respectively. Results for the Sanger rotor effort yielded an 8.1 % improvement in mass flow rate, a 5% improvement in total pressure ratio, a 0.9 % increase in adiabatic efficiency, and a reduction in blade weight of 59% (before dynamic and aeroelastic structural analysis). Application to the NASA Fan resulted in a 2.5 % increase in polytropic efficiency. The results validate the utility of the BLADE-3D Bezier geometry package for use in future development of automated optimization routines for turbomachinery blade design.

THIS PAGE INTENTIONALLY LEFT BLANK

I. INTRODUCTION

Current techniques in turbomachinery blade design involve considerable empiricism and rely heavily upon the personal expertise and judgment of the human designer to arrive at a final working design. As computer analysis tools become more sophisticated and interactive, efforts to use them to their fullest potential will undoubtedly lead to a wholly automated design process that involves the designer primarily as a sanity check at the end. Computerized design optimization for turbomachinery blading is still in a fairly primitive state, and the reasons are plentiful. Despite the fact that very sophisticated and accurate three-dimensional CFD tools exist, traditional blade designers are somewhat reluctant to trust them completely. Also, many of these codes require considerable computer time to execute and this expense is often cited as justification for using simpler and faster, albeit more primitive, flow analysis tools that involve 2-D and quasi3-D methods instead of full three-dimensional analysis. Three-dimensional flow codes that utilize Navier-Stokes solutions rely on empirical turbulence models that many designers are uncomfortable with. These are but a few of the reasons frequently given for sticking with older, tried and true design methods.

One of the biggest obstacles to the development of 3-D computerized design optimization processes has been the lack of a suitable blade geometry package which allows the efficient application of traditional computer optimization techniques. Turbomachinery blades are usually represented mathematically by stacks of 2-D airfoil data that typically require at least 11 parameters per section or hundreds of points in space for full blade shape definition. Even though 3-D flow codes are being used more and more to analyze blade performance in the design phase, design changes based upon these analyses are still performed on individual 2-D airfoil sections in a tedious process that is largely dependent upon human judgment. The development by Abdelhamid of the BLADE-3D Bezier geometry package represents a significant step forward in this area [Ref. 1]. His 32-point, two parameter method of representing complete blade geometries should greatly enhance efforts to develop automated design schemes which alter blade

shapes three-dimensionally, thereby achieving greater improvement in performance with fewer iterations.

The objective of the present study was to investigate the utility of BLADE-3D in the computerized design optimization of transonic fan blades. It was the first step in what is hoped will be a continued effort based upon Abdelhamid's work. It sought to develop a design methodology or algorithm, one that relies as little as possible on human judgment for design change decisions and validates the potential for a fully automated process. It was not the goal to address issues of computing expense, flow code accuracy or other problems contributing to the current state of blade design optimization. Computers get faster and more powerful almost on a monthly basis and flow analysis software designers are getting smarter every day. The objective was simply to demonstrate the idea that automated design optimization is possible, and that with additional work, a viable software capability to do it might be achieved.

It will be noted that the designs achieved during the study are 'point optimized', that is, the blade shape was optimized and the performance maximized for a single set of boundary conditions. Clearly, every compressor design process must consider off-design performance as well, and that requirement is acknowledged. It is probable that off-design conditions could be looked at using the same methodology and that compromise designs could be achieved iteratively, although that concept was not examined here.

The algorithm developed here includes steady, static structural analysis of interim and final blade designs using the geometry package to pass information between disciplines in the optimization process. Consequently, the algorithm is truly multidisciplinary. No attempt was made to include dynamic response, aeroelastic effects or fatigue analysis in the design methodology (although a basic examination of the modal response characteristics for the resulting blade designs was performed and is provided in Appendix A, along with a brief discussion of flutter). These are obviously areas that would need to be addressed in order to have a complete and utile optimization package.

The following chapters provide the details as to the course and outcome of the effort. First, background and historical information is presented to provide the

foundation for further discussion. The various resources used in the study including the BLADE-3D geometry package itself, other computer codes and the test fan designs are described next. The development of the algorithm is then explained in some detail followed by presentation and discussion of the results.

II. BACKGROUND

A. BASIC CONCEPT

The purpose of an axial-flow fan rotor is to increase the total pressure of the air flow by imparting additional velocity through rotation. Figure 1 illustrates this concept for the Sanger rotor, one of two transonic fan designs used in this research, at 27,000 RPM and an exit static-to-inlet total pressure ratio of 1.19 [Ref. 2,3].

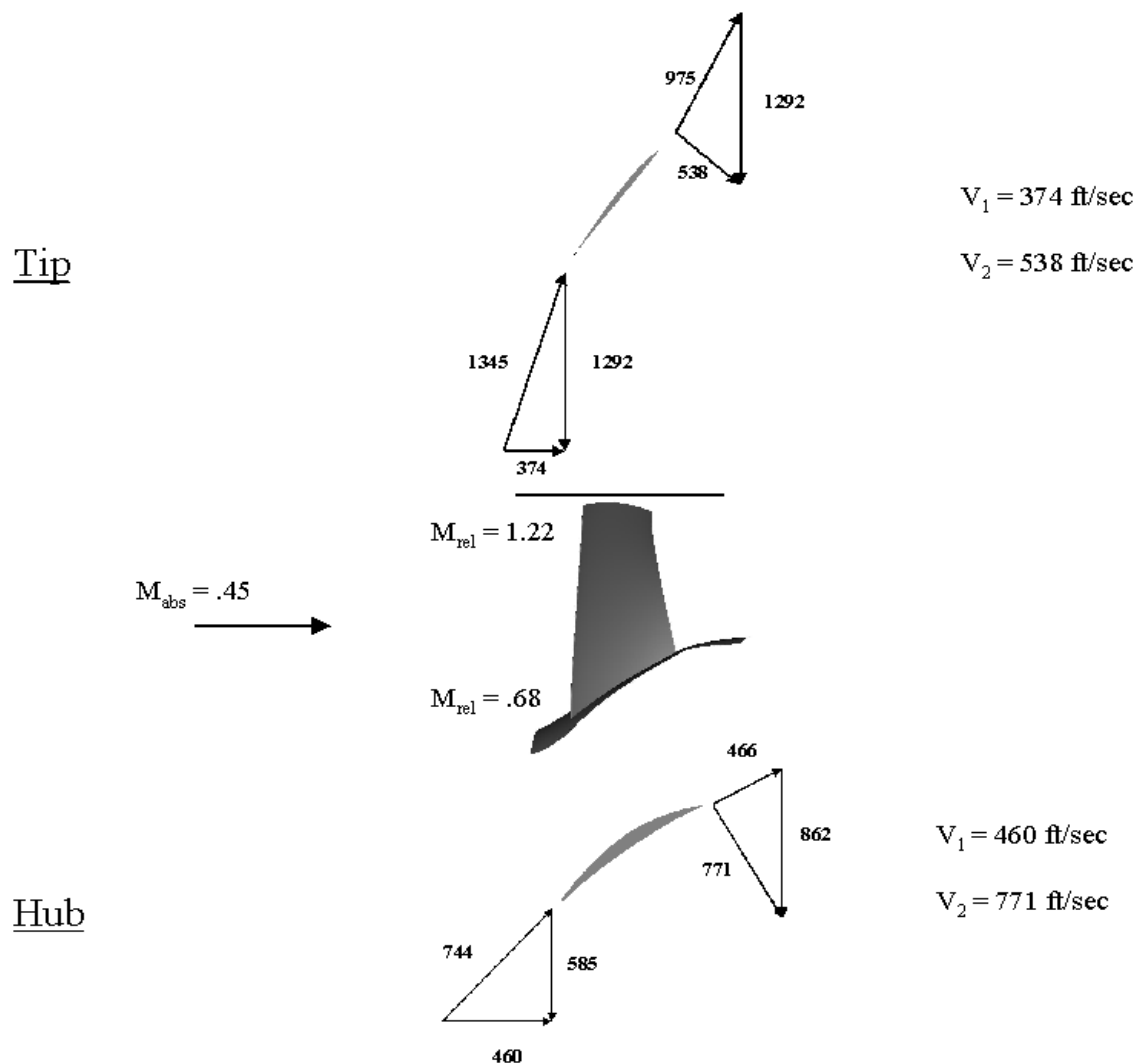


Figure 1. Velocity Changes Across a Transonic Rotor

The performance of a rotor design is characterized by several performance parameters. Primary among these are total pressure ratio, total temperature ratio, adiabatic and polytropic efficiencies, and mass flow rate. Methodology for calculating these and the other metrics used in this work may be found in Appendix B.

B. OVERVIEW OF CURRENT DESIGN PROCESS

The design of a modern axial flow compressor is achieved through a series of distinct steps. Although these steps have evolved in sophistication over the years, they remain essentially the same as those used to design the first generation of operational jet engines in the 1940's and 1950's. First, a set of overall performance parameters must be identified for the compressor. These parameters are usually determined by the work output capability of the turbine and must be matched closely to the other major components of the engine. Once the design objectives such as total pressure ratio, mass flow rate, number of stages, etc are determined, a preliminary design for each stage may be performed.

A meridional analysis of the flow through the compressor is conducted with the assumption that the flow is axisymmetric. Flow properties such as pressure, temperature and velocity are defined along streamlines at the entry and exit of each blade row and a determination is made as to the shape of the flow passage, as well as the convergence characteristics of the stream surfaces from radial equilibrium. Earlier applications of this throughflow analysis performed calculations between blade rows and accounted for blade losses with empirical data alone. Later versions added complex analytic loss models. More current methods use numerical techniques to accurately calculate the flow through the blade rows using body force terms in the equations of motion to satisfy radial equilibrium at every point in the flow field. Wennerstrom provided a good general description of current methodology [Ref. 4].

After entry and exit characteristics are determined for each row, calculations are performed to determine the variation in pressure and velocity along each stream surface and produce velocity triangles which are used to define blade section profiles. Two-dimensional blade sections are assigned by determining a mean camber line and thickness

distribution that achieves the desired turning characteristics of the flow. The profiles, usually airfoils, are quite often chosen from existing databases and come with well-understood loss characteristics. Two-dimensional CFD tools may be utilized at this point to verify or perhaps improve performance of the individual airfoil sections. These 2-D blade sections are then stacked radially to achieve an initial 3-D shape for the blade. The through-flow and blade-to-blade calculations are usually performed iteratively to achieve an acceptable preliminary design.

The next phase comprises finalizing the design. A preliminary structural analysis is performed on the 3-D blade to verify that anticipated stresses and deflections are not excessive. Additionally, 3-D CFD analysis may be conducted to determine whether or not the blade meets its overall design criteria. If not, changes are made to section profiles along selected stream surfaces in hopes of improving overall performance. Once adequate aerodynamic performance is achieved, a final structural analysis is performed to ensure that all structural requirements are met. These include dynamic response characteristics, aeroelastic effects, and fatigue. In addition, a shape correction procedure is normally implemented to account for deflections in the blade due to the rotational, thermal and gas loads encountered in use. Once the de-rotated shape of the final blade is determined, it can be manufactured and tested. The final compressor design is the culmination of this process for all blade rows and stages within the compressor.

As previously stated, the design process has evolved over time and uses ever more sophisticated tools and procedures to achieve the high performance required of today's turbomachinery applications. A brief review of this evolutionary history follows.

C. HISTORICAL PERSPECTIVE

In the early years of jet engine design, i.e., the late 1930's and throughout the 1940's, no generalized theory existed for the detailed calculation of flows through turbomachines. The first compressors were primarily of the centrifugal type and were designed essentially by cut and try. Configurations were conceived, built and tested and empirical databases for different designs were created. Axial and mixed flow machines

came later and again, many were designed by cut and try, using blade shapes determined primarily through cascade wind tunnel tests.

In 1952, Wu introduced a revolutionary theory for the exact calculation of turbomachinery flows [Ref 5]. It achieves solutions by calculating along two intersecting families of stream surfaces – a family of blade-to-blade (S_1) surfaces and a family of throughflow (S_2) surfaces as shown in Figure 2.

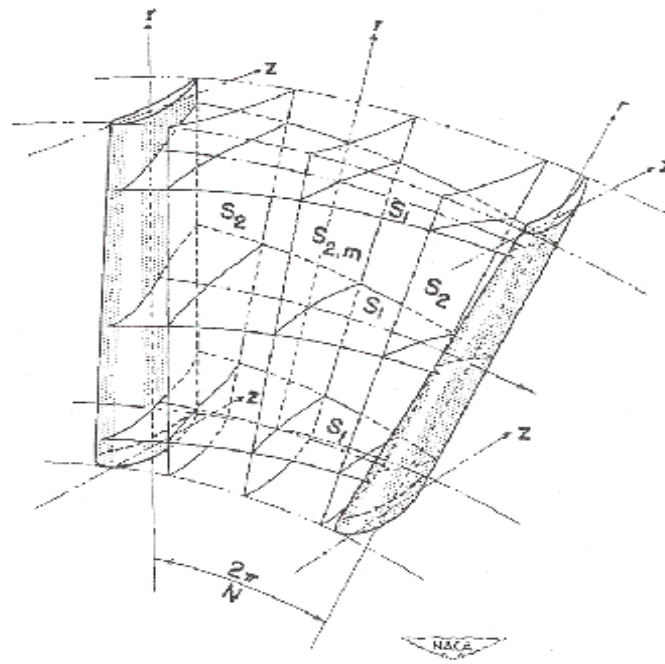


Figure 2. Stream Surfaces in a Turbomachine (From Ref. 5)

Analysis is performed on first one set of stream surfaces and then the other in an iterative manner until a satisfactory flow solution is obtained. The method is quite flexible in that the numbers of stream surfaces in either direction can be tailored to fit the specific problem at hand. Although it yields a fully three-dimensional result, it was complex and cumbersome when first introduced and for that reason, much effort has been expended toward simplifying the process.

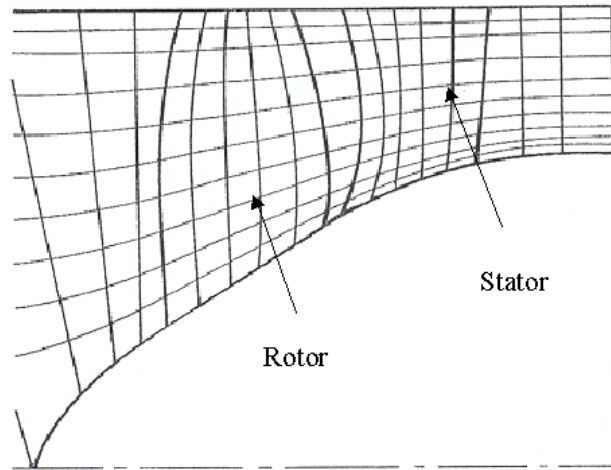


Figure 3. Throughflow Analysis Framework (After Ref. 4)

The most common simplification of Wu's method uses one S2 surface and multiple S1 surfaces in a procedure that has become known as the Quasi-3D (Q-3D) approach to turbomachinery design. A diagram of the throughflow calculation path is shown in Figure 3. In Q-3D, the flow is assumed to be axisymmetric with S1 surfaces taken as surfaces of revolution at various radial locations. As previously mentioned, earlier versions of this approach used between-blade calculating stations along the S2 surface with blade effects accounted for with loss predictions derived from empirical data. Designs produced with this method deviated only slightly from the previous ones upon which they were based and this led to a somewhat conservative mindset in the approach to blade design that persists even today.

Evolution of the Q-3D process brought the development of analytical tools with which to predict losses inside blade rows and thereby decrease the heavy reliance on empiricism. Mathematical loss models were developed which coupled fluid dynamic elements with observed empirical results and thereby made more generalized viscous flow predictions possible. Koch and Smith presented such modeling in 1976 [Ref. 6]. Shock loss prediction models for transonic blading were introduced as well. Miller et al. produced a 2-D model in 1961 which became the standard tool for predicting these losses in axial compressors [Ref. 7]. Wennerstrom et al. updated the model in 1983 to account for three-dimensional effects such as shock obliquity and for weak losses from flow at

high subsonic Mach numbers [Ref. 8]. This updated model proved to be more accurate than Miller in predicting shock losses.

As computer resources became more available in the 1960's and 1970's, numerical techniques for solving the throughflow problem were developed that used in-blade computing stations in addition to those between the blade rows [Ref 9]. The calculations were performed using a variety of techniques the most common of which became known as the streamline curvature method. Others included matrix solutions, finite element modeling and various time-marching schemes. The streamline curvature method was developed by Smith, Silvester, and Hetherington in 1966, has been refined over the years and according to Wennerstrom, remains the method of choice for throughflow analysis today [Ref. 4,10,11]. In 1974, he outlined a through-blade version of the method, which represented the blades using distributed body forces in the momentum equations inside each blade row. Derivatives in the circumferential direction were eliminated by formulating the equations axisymmetrically [Ref. 12]. A less simple but more accurate approach was published by Jennions and Stow in 1985 [Ref 13]. It formulated the equations of motion in three dimensions and then used a circumferential passage averaging technique to simplify the analysis to 2-D form. Their version of the throughflow analysis was packaged in a computerized system which included blade-to-blade analysis and a stacking line procedure, and was one of the first efforts to produce an overarching computer process for the aerodynamic design of turbomachinery.

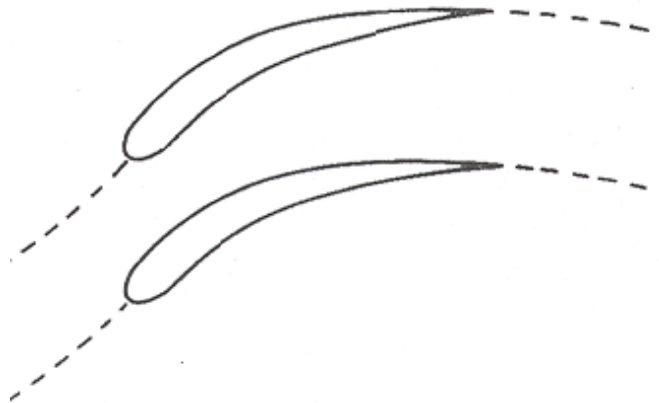


Figure 4. Blade-to-Blade Stream Surface

The development of blade-to-blade analysis for the determination of blade profiles along stream surfaces has followed a similar path. A blade-to-blade stream surface is depicted in Figure 4. Early work on the subject, such as that presented by NASA in 1965, relied on information contained in extensive empirical databases to choose pretested airfoil shapes to achieve desired turning of the flow [Ref. 14]. In 1969, Crouse et al. introduced a computer program which developed blade shapes mathematically by producing double circular arc elements along conical surfaces that approximate the meridional stream surfaces [Ref. 15]. This system was updated in 1981 to include an upfront throughflow analysis code, and a more complex shape generation capability utilizing high-degree polynomials to define the section camber line, as well as the pressure and suction surfaces [Ref. 16]. A blade stacking procedure was also addressed. The ‘Crouse Code’ remains the basis today for the generation of initial 3-D blade geometries.

Computational fluid dynamics (CFD) has evolved over the years as a valuable tool for analyzing the flow through turbomachines. As computing power has grown, CFD codes have progressed from 2-D potential solvers to Euler solvers with differential boundary layer to 2-D Navier-Stokes solvers and finally, to full 3-D Navier-Stokes codes that can be used to analyze an entire blade, a stage, or even a whole compressor. These codes have not yet been used extensively in the initial stages of design but have mainly been used to analyze the flow around mature designs (achieved with the lower order methods previously discussed) and to help verify performance prior to build and test. There has been quite a bit of effort to integrate CFD more fully into the design process however. Until recently, this has been limited to utilizing 2-D codes to aid in the blade-to-blade portion of the Q-3D process, and to using 3-D analysis at the end to verify the design. Denton stressed the importance of fuller utilization of 3-D CFD to enhance accuracy of blade designs, and put forward his own 3-D design procedure [Ref. 17]. Sanger used Denton’s 3-D CFD code to design one of the two rotors used in the present research.

Wennerstrom states, “Since we use 2-D codes to design the hardware and will be using a 3-D code to analyze the flow through that hardware, the question is what do we

change to achieve the result we want from 3-D analysis?”[Ref. 4]. He claims that the designer must visualize such changes and that an optimization strategy based upon 3-D CFD is largely one of trial and error. That premise provides the catalyst for the present research.

D. NEWER DEVELOPMENTS

Over the last decade, many new concepts have been introduced to improve the blade design process. They have been aimed at both improving the performance of resulting designs and at streamlining the process itself, so that designs may be achieved more quickly and economically. A few of those concepts will now be discussed.

1. Sweep

The idea of sweep to improve the aerodynamic performance of transonic and supersonic wings has been known since the earliest days of jet-powered flight. Sweeping the wings aft decreases the speed of the chordwise component of the flow, thereby reducing the drag caused by supersonic shock wave effects. The flows inside turbomachines are much more complicated however, and the positive effects from sweep observed in external aerodynamics are not easily applied to compressor flows, due to rotation and the complex interactions with case walls at the hub and tip. There have been numerous investigations into the effects of sweep on the performance of transonic fan blades, and swept designs have actually been designed, built, and tested; although they are not yet in widespread commercial use. References 18-20 describe earlier efforts to incorporate sweep into transonic rotor designs. In 1997, Wadia et al. reported the results of an extensive swept-rotor test program, and offered analyses of various sweep schemes and their relative impact on blade performance [Ref. 21]. Abdelhamid developed a new 3-D blade geometry package which he utilized to investigate sweep effects on a test rotor designed for the Naval Postgraduate School [Ref. 1]. The present work is based largely upon the success of his efforts.

2. CFD and Design Optimization

As mentioned, 3-D computational fluid dynamics has not, until very recently, played much of a role in turbomachinery design. It has been a valuable analysis tool but has generally been considered too unproven, as well as bulky and expensive, to use in routine blade design. Q-3D methods, as a rule, use simpler formulations of the flow equations (Euler vs. Navier-Stokes) that can be solved more quickly and require less computer time, thus making them more attractive for everyday design tasks. Some work has been done to try and find even quicker solutions to these equations, thereby making the Q-3D methodology that much more attractive despite its limitations [Ref. 22]. Q-3D methods have been used, along with optimization techniques similar to those utilized in this research, to find optimized 2-D section profiles which are then stacked to form an ‘optimized’ compressor blade [Ref. 23]. The problem is that there has been little or no success in improving real blade performance measures using this method. Much effort has been focused on aligning computerized Q-3D solutions with those obtained using full 3-D analysis, such that the former may be used as a quicker and easier substitute for the latter. Attempts to better approximate 3-D CFD solutions by manipulating variables in simpler codes has shown some promise, but the results still lack the fidelity and flexibility of true 3-D flow codes [Ref. 24].

3. 3-D Inverse Methods

Another technique that seeks to take advantage of the power of 3-D CFD analysis in blade design, without truly designing in three dimensions, is the 3-D inverse method [Ref. 24,25,26]. 2-D inverse methods create blade section profiles by finding a thickness distribution and camber which produce a given distribution of some chosen flow parameter, usually pressure, on either side of the blade. This is different from the conventional direct method in which blade section shapes are selected from an existing catalog or assigned based on the geometry package in Crouse’s code. The 3-D inverse method starts with a ‘guessed’ blade geometry and then modifies that geometry utilizing flow field information obtained from 3-D CFD analysis. Corrections to the initial geometry are applied at multiple spanwise sections using the 3-D CFD pressure

distribution information which includes the effects of spanwise flow, case wall interaction, etc. The biggest problem with this technique, as it stands, is that a blade must already exist to produce the 3-D CFD solution in the first place; so the exercise, it seems, becomes one of showing that the 3-D inverse method can be used to replicate an existing design. Further work is required to develop practical inverse methods which incorporate the use of 3-D CFD in blade design.

4. Multidisciplinary Design Optimization (MDO)

The concept of Multidisciplinary Design Optimization (MDO) is one which is being applied more and more often to the machine design field. In its most rigorous form, it consists of algorithms and computerized methods for determining the relative contributions and importance of various disciplines (such as aerodynamics, structures, manufacturing, overall cost, etc.) to the design process and then ensuring that the process is properly aligned with those relationships [Ref. 27]. In its simplest form, it refers to the idea that a final design should not be prescribed in one area before the other areas have at least been looked at to ensure there will be no problems down the road. Most current applications involve an iterative process in which aerodynamic designs are modified based on structural considerations, structural designs are changed because of manufacturing capabilities, and overarching changes are made due to cost. Reference 27 states,

In final turbomachinery design steps, 3-D blade design optimizations need quickly converging algorithms treating one single aerodynamic objective. The other involved disciplines lead to further constraints.

Such was the attempted implementation of MDO in the present research effort.

III. RESOURCES

A. BLADE-3D – THE ABDELHAMID BEZIER GEOMETRY PACKAGE

In 1997, Major Abdelhamid of the Egyptian Air Force, while a PhD student at NPS, created a new and greatly simplified geometry scheme with which to represent the shapes of turbomachinery blades [Ref. 1]. The package, which this author has adapted and chosen to call BLADE-3D, defines the blade geometry as a set of Bezier surfaces, which are a special class of what are known as non-uniform rational B-spline surfaces, or NURBS surfaces for short. While using NURBS to represent complex geometric shapes in design processes is not new, there are several features of BLADE-3D which make it unique when applied to turbomachinery design. This section will provide a brief overview of those features.

The Bezier surfaces, or surface patches as they are known, are derived from basic Bezier curve methodology, which parametrically represents complex curved shapes analytically with a minimum number of free parameters. The formulation was developed in the late 50's by an engineer at Renault, the French automaker, as an easier way to represent the curves used in auto body design [Ref 28]. Bezier curves may be expressed mathematically in several forms. One common method is to use a polynomial formulation, known as the Bernstein polynomial, to represent the curve as a function of a chosen parameter t . A cubic Bernstein polynomial is written as:

$$Q(t) = (1-t)^3 * P_1 + 3t(1-t)^2 * P_2 + 3t^2(1-t) * P_3 + t^3 * P_4$$

where $P_n = P_n(x,y,z)$ are the four control points that define the Bezier convex hull. A cubic Bezier curve and its convex hull are shown in Figure 5.

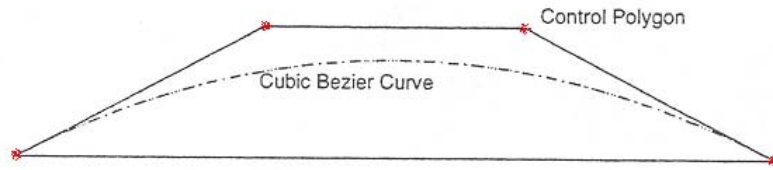


Figure 5. Bezier Curve with Convex Hull (After Ref. 1)

It can be seen from the figure that the Bezier curve lies completely within the polygon of control points. The two endpoints of the curve also form the bottom corners of the polygon and lines from those points to the inner control points are tangent to the curve at the endpoints. Movement of any of the four control points will change the shape of the entire curve and the shape change at any point is proportional to its distance from the control point that was moved. These are interesting properties of Bezier curves.

There are several other properties which make Bezier curves and surfaces well-suited for the present application [Ref. 1]. First, they are invariant under translation, rotation and scaling, which means that transformations may be applied to the control points to achieve the same result for the overall curve (important with regard to the sweep function). Continuity of slope of adjoining Bezier curves may be ensured by requiring that the common endpoint and the next control point in each curve are colinear. Continuity of curvature may be maintained by ensuring a common ratio between the segment lengths of adjoining curves. These properties are important in the fitting of the leading and trailing edge surfaces to the major surfaces of the blade, as will be discussed shortly.

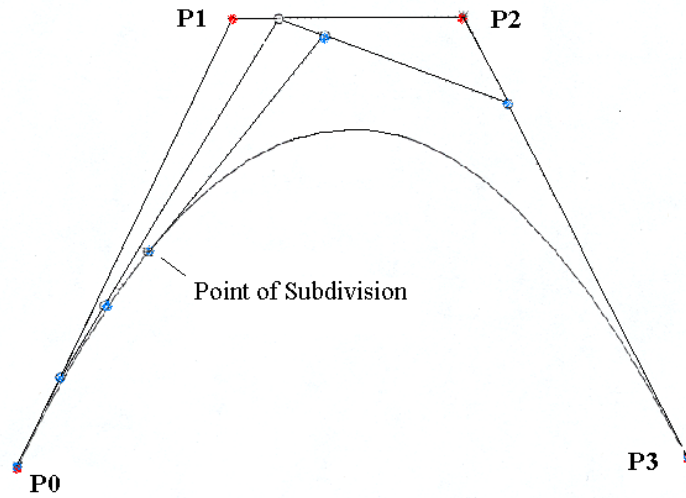


Figure 6. Subdivision of Bezier Curves (After Ref. 1)

Figure 6 shows one last property that is important, that of subdivision. Bezier curves may be divided into smaller segments, which may in turn be represented by their own sets of control points. These new control points may be determined mathematically from the original Bezier control points. Again, this proves useful in fitting leading and trailing edge surfaces to the blade.

BLADE-3D uses six cubic Bezier surface patches to represent the surfaces of the turbomachinery blade [Ref. 1]. Two of these surface patches form the entirety of the pressure and the suction surfaces. The other four surfaces comprise the leading and trailing edges, and form a very small portion of the overall blade. Each side of the blade then may be described analytically by only sixteen points in space, the Bezier control points, as opposed to the many points required by NASA's traditional MERIDL format [Ref. 16]. This feature, more than any other, is what gives BLADE-3D so much potential as a blade design optimization tool. A Bezier surface and its net of sixteen control points is presented in Figure 7.

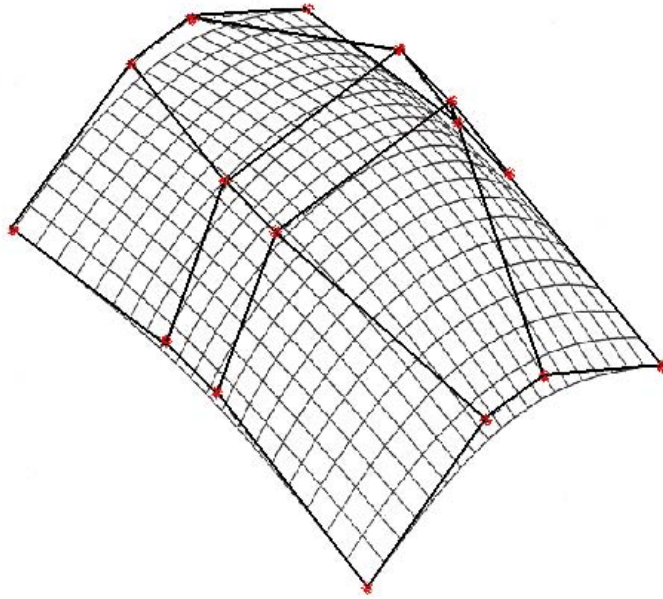


Figure 7. Bezier Surface with Control Point Net (After Ref. 1)

To obtain the control points for the Bezier surface that approximates the pressure or suction surface of a given blade, the blade is first represented by a set of data points. A parameter is chosen based on the geometry (arc length for example) and a set of control points calculated to approximate the surface. A nonlinear least squares procedure is then performed to determine the error between the calculated surface and the original surface. This error is then used to modify the original parameterization and the process is repeated. This iterative procedure is performed until a suitable parameterization is found and the most accurate control points are determined.

Leading and trailing edge surfaces are fitted to the pressure and suction surfaces by choosing scaling parameters which take advantage of the continuity of slope and curvature properties of Bezier curves. These parameters are used to generate curves which maintain the slope and curvature of the pressure and suction surfaces at front and back. These surfaces are joined and terminated at a midpoint, for which only continuity

of slope is achieved. A blade profile showing all six Bezier surfaces is shown in Figure 8.

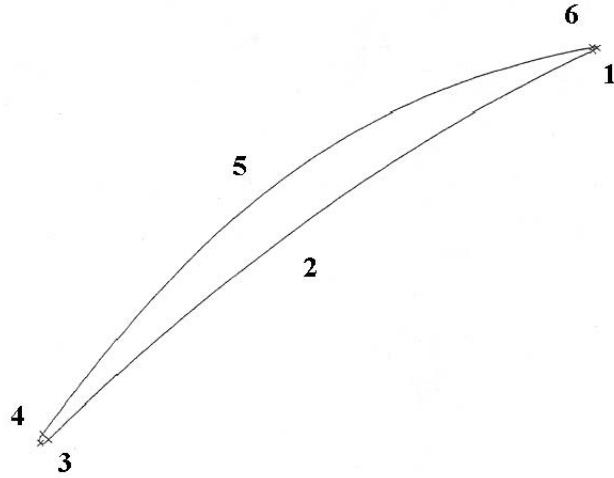


Figure 8. Bezier Representation of Compressor Blade (After Ref. 1)

Subdivision, as previously described, may be used to change the point on the pressure or suction surface where the leading or trailing edge is fitted. This, as will be seen later, is important in maintaining the chord length and overall footprint of the blade.

BLADE-3D was written in C++, an object-oriented program language in which code may be formulated in chunks and then simply dropped into higher order routines to carry out complex mathematical manipulations. It is organized into six subpackages, which build in turn on the preceding one. Abdelhamid felt that such an architecture for the package would be useful in constructing interfaces with other software tools such as grid generators, flow analysis codes, structural analysis tools and ultimately, software designed to control manufacturing processes. He envisioned the development of a graphical user interface in the future to make interface with the package easier. A few modifications to the code were made by the author which helped adapt it to the research problem at hand. Those changes are fully described later.

A complete discussion of the theory and formulation underlying BLADE-3D along with an extensive list of references pertaining to NURBS in general and Bezier curves and surfaces specifically is contained in Reference 1.

B. THE SANGER ROTOR

A transonic compressor stage was designed by Sanger at the NASA Glenn Research Center for use in the Turbopropulsion Laboratory at the Naval Postgraduate School as a research and teaching tool. In many ways, the rotor is well-suited as the test article for the present study since the design philosophy relied heavily upon CFD techniques and sought to minimize the use of conventional empirical design methods. Sanger used Denton's TIP3D three-dimensional flow code, an Euler solver with viscous forces accounted for by distributed body forces, to complete the design. The process yielded an aggressive, highly-loaded rotor which promised very good performance. Performance enhancements achieved through the optimization process pursued in the present study would certainly bode well for application to less mature designs.

The Sanger design was built and then tested in the compressor test rig at NPS. Unfortunately, before the testing could be completed at the highest speeds, the test rig suffered a hardware failure and the rebuilt stage has not yet been tested at 100% speed. The design parameters for the Sanger rotor are shown in Table 1 and a picture of the rotor is provided in Figure 9.

Total Pressure Ratio	1.61
Tip Speed	1300 ft/sec
Design Mass Flow Rate	17.09 lbm/sec
Tip Inlet Relative Mach Number	1.28
Aspect Ratio	1.2
Hub/Tip Radius Ratio	0.51
Number of Blades	22
Tip Solidity	1.3
Tip Diameter	11.0 inches

Table 1. Sanger Rotor Design Summary

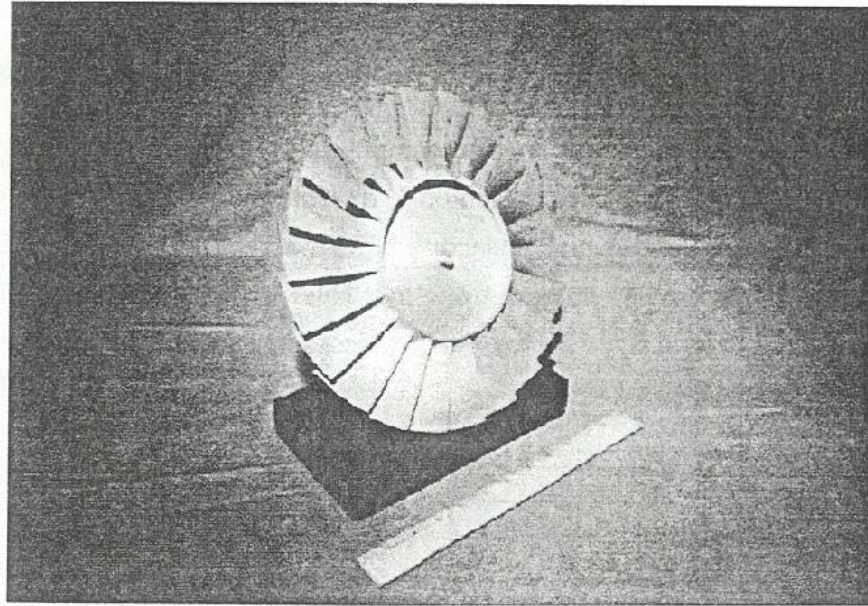


Figure 9. The Sanger Rotor (From Ref. 3)

A complete description of the Sanger rotor, the design process and the CFD performance results may be found in References 2 and 3. Previous work at the NPS Turbopropulsion Laboratory involving the Sanger stage are contained in References 29 through 32.

C. NASA ROTOR 67

NASA Rotor 67, also known as the ‘NASA Fan’, was designed in the late 1980’s at the NASA Lewis Research Center (now Glenn) and has been used extensively as a test case in the design, test and validation of many CFD software codes, tools and procedures. Its design parameters and performance characteristics have been widely reported in the open literature and may be readily obtained from the Internet. A brief synopsis of the design parameters for Rotor 67 is presented in Table 2 and a flow visualization image is shown in Figure 10.

Total Pressure Ratio	1.63
Tip Speed	1400 ft/sec
Design Mass Flow Rate	73.15 lbm/sec
Tip Inlet Relative Mach Number	1.38
Aspect Ratio	1.7
Hub/Tip Radius Ratio	0.37
Number of Blades	22
Tip Solidity	1.26
Tip Diameter	20.0 inches

Table 2. Rotor 67 Design Summary

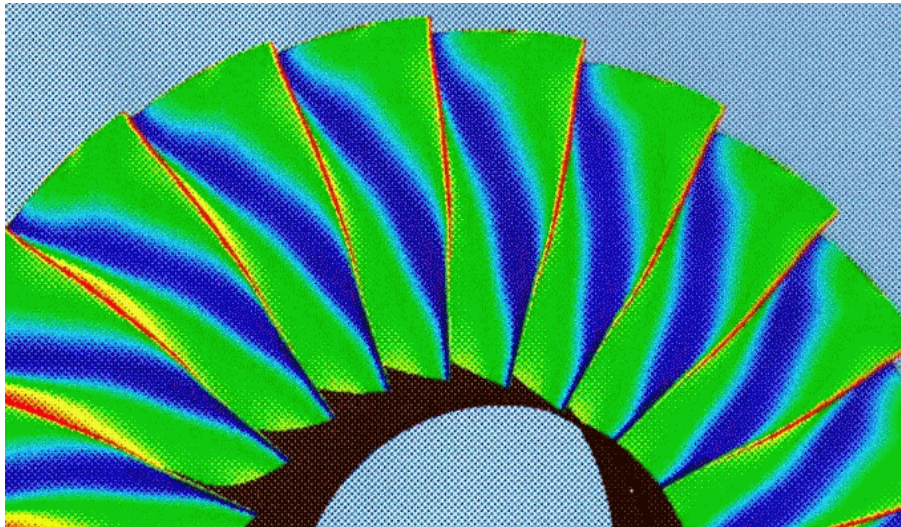


Figure 10. NASA Rotor 67

D. RESEARCH TOOLS

1. Grid Generator – TCGRID

TCGRID (Turbomachinery C-GRID) is a FORTRAN program designed to generate three-dimensional grids for turbomachinery blades [Ref. 33]. It was developed by Chima at NASA Glenn and is based upon an old, two-dimensional version of the Steger/Sorenson GRAPE code, which generates blade-to-blade grids on surfaces of revolution at given spanwise locations [Ref. 34]. TCGRID stacks and reclusters the grids spanwise to form the 3-D grid. All geometry manipulation in TCGRID is done with parametric cubic splines and

the code can handle axial, centrifugal and mixed flow machines. The code accepts input in several formats and can generate either H-type or C-type grids, which are compatible with both the RVC3D and SWIFT flow analysis codes. An example of a TCGRID-generated C-grid is shown in Figure 11.

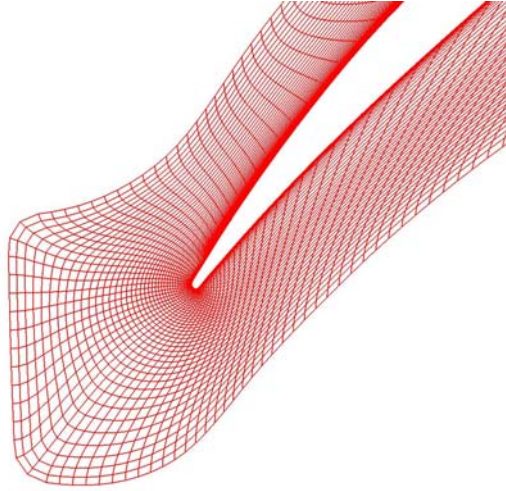


Figure 11. Leading Edge Detail of a Computational C-Grid from TCGRID

2. Flow Analysis Code – RVC3D

RVC3D (Rotor Viscous Code 3-D) is a computer code for analysis of three-dimensional viscous flows in turbomachines [Ref. 35,36,37]. It too was developed by Chima at NASA Glenn and solves the thin-layer Navier-Stokes equations utilizing a multistage Runge-Kutta explicit finite-difference technique. The equations are mapped to a general body-fitted coordinate system, with streamwise viscous terms neglected in accordance with the thin-layer assumption. Turbulence effects are modeled with a 3-D adaptation of the Baldwin-Lomax turbulence model, or an alternate model based upon Cebeci-Smith [Ref. 37]. The program is capable of analyzing either annular blade rows or linear cascades. A simple tip clearance model based upon a pinched blade tip is available. Variable inputs to the program include inlet total temperature and pressure, exit static-to-inlet total pressure ratio, and rotational speed. The output is in standard q-file format and is compatible with PLOT-3D and FAST flow visualization codes.

3. Flow Visualization Software – FAST

FAST (Flow Analysis Software Tool) is a menu-driven software program designed to aid in the analysis of CFD code outputs. It accepts grid generator and flow code output files, matches them and produces visual images of the details of the flow. It can perform calculations of a variety of flow field properties, including pressure and Mach number, and can produce useful images of the aerodynamic body being studied. The grid, blade, and flow images contained in this report were produced using FAST.

4. Structural Analysis Tools

a. Initial Graphics Exchange Specification – IGES 5.3

The Initial Graphics Exchange Specification is the standard for defining geometric objects for import into computer-aided design/modeling (CAD/CAM) software programs, and allows rapid interchange of data among a variety of engineering software applications [Ref. 38]. It has an 80-column ASCII format, and a standard IGES file is composed of five parts – Start, Global, Directory, Parameter, and Terminate. An example of an IGES input file for the Sanger rotor is provided in Appendix E.

b. I-DEAS Master Series Six

I-DEAS (Integrated Design Engineering Analysis Software) is an integrated package of mechanical engineering software tools [Ref. 39]. It is made up of a number of software modules called “Applications” which are further subdivided into “Tasks”. The two application modules used in the present work were the “Design” module, under which the blade geometry was imported and manipulated to create a solid, and “Simulation”, which contains the tasks involved with finite element analysis such as meshing, application of loads and boundary conditions, and solving for stresses and deflections. I-DEAS is a menu-driven program which can accept input information in a variety of ways, including IGES, NASTRAN and ANSYS file formats. Results are visually displayed and a universal file containing numerical values of finite element analysis data is also provided. Outputs may be formatted for use in other CAD/CAM software tools.

IV. METHODOLOGY

A. OVERVIEW

The purpose of this section is to describe how the resources listed in the previous section were used to achieve the results reported in the sections that follow. It proceeds in near chronological order and seeks to provide some of the major details involved in the research. An attempt is made to stay on course and avoid straying into tangential discussions but in a few cases, additional detail is provided for completeness.

B. ADAPTATION OF BLADE-3D

The first steps taken were to access and become familiar with Major Abdelhamid's geometry package, BLADE-3D. As previously discussed, the overall package consists of six C++ member class subpackages which are called by a main program to fit or change a geometry [Ref. 1] These codes resided in a number of computer files archived on the NPS aeronautical department's UNIX computer system, and had not been accessed for about two years. The files contained very little annotation and there was no written documentation to describe how they were to be used. To someone unfamiliar with C++, these files represented, in effect, an archeological cipher project which seemed very daunting at the time.

After a self-taught crash course in C++ [Ref. 40], the author set about trying to learn and exercise BLADE-3D. The most logical course of initial action was to try to reproduce Abdelhamid's results in fitting and manipulating the Sanger rotor geometry thereby learning in the process how to run and make modifications to the code, as required. A suitable MERIDL3 input file for the Sanger geometry (Appendix D) was available, so the problem became a matter of constructing a C++ main program to read the input file, call the appropriate member programs to perform the Bezier fit and then to produce a recognizable output. This proved to be no small task.

Understanding the structure of C++ programming is a small first step in the process of learning to actually compile C++ code and create executable routines.

Abdelhamid chose C++ because it was an object-oriented programming code within which packages may be written and then picked and chosen to put together short, concise executables. He structured his geometry package such that each member class of routines was based upon other, simpler ones. This makes sense until it comes time to work with the UNIX C++ compiler. For the present work, all the member classes had to be studied and recompiled to ensure that none of the executable object files had been corrupted during storage and transfer. It was required that the compilations be performed in a particular order utilizing just the right groupings of previously compiled object files or else the compilation would fail. It took a month or so of dedicated effort to learn how Abdelhamid's classes of subroutines fit together and to compile them into usable files. (Consideration was given to translating everything into MATLAB but that idea was abandoned as too labor intensive). In the end, the compiler issue greatly aided in becoming familiar with all the subroutines and understanding which ones were most important for using the package. The experience was very helpful when code changes were made later.

Once the codes were compiled and ready, the task became, as stated, to select an input routine, whatever geometry manipulation routines were required, and an output. There were three different input schemes and two outputs, all of which resided in the class 'blade'. The inputs allowed data to be read either as surface points on the blade or as the Bezier control points used by the package. The surface points could be in Cartesian coordinates, or in MERIDL2 or MERIDL3 formats, which use cylindrical coordinates. The control point inputs could be selected for either those that define all six blade surfaces or for those that define the pressure and suction surfaces only. Outputs could be in either surface point or control point form.

The first effort at utilizing the code was to try and read the MERIDL3 Sanger rotor coordinates and output Bezier control points that matched those published in Reference 1. First attempts at this failed, apparently due to the fact that the input routine could not recognize the MERIDL3 input data, which it was obviously designed to do. A detailed review of the input code revealed an apparent flaw in the logic which converted the MERIDL3 data into Cartesian coordinates for use in the fitting routines. The origin

of this bug in the code is unknown. The problem was corrected and control points were finally produced for the pressure and suction surfaces of the Sanger geometry, which matched those in Reference 1 reasonably well.

BLADE-3D incorporates a routine that fits leading and trailing edge surfaces to the previously fitted pressure and suction surfaces, in accordance with a shape parameter provided in the input file. What the values of these shape parameters should be was again a question that required investigation. Abdelhamid's files did not contain the appropriate parameter values nor did his notes allude to them. Examination of the code revealed that the parameters were percentages of the overall blade chord, which determine the extent of the leading and trailing edges, and therefore were most likely on the order of .01, .05 or maybe even 0.1. Figure 12 shows the variation of the leading edge shape with changes in the leading edge parameter.

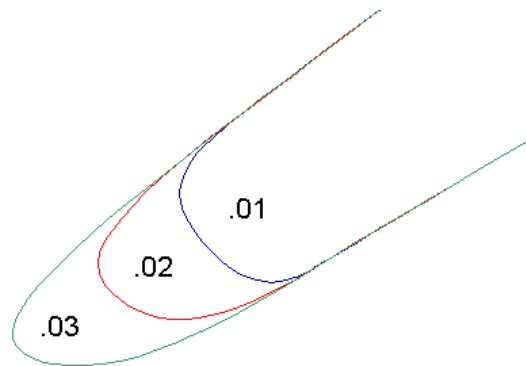


Figure 12. Effect of Leading Edge Parameter Change

After considerable effort, the shape parameters were chosen to be .02 and .01 for the leading and trailing edge respectively. These values produced the control points which most closely matched those reported by Abdelhamid, although there was still a problem. As discussed in Reference 1, application of the leading and trailing edge parameters directly to the pressure and suction side control points obtained from fitting the MERIDL code yielded a blade which was longer chordwise than the original. In addition, the shapes of the leading and trailing edges were asymmetric about the camber line. The obvious solution was the application of the subdivision routines contained

within BLADE-3D but again, there was no guidance on how they should be implemented. Through more trial and error, it was concluded that applying subdivision to both the pressure and suction surfaces in an amount equal to roughly half the leading edge shape parameter resulted in an appropriate correction to the chord length. It was also found that if these corrections were applied unevenly, that is, slightly more to the suction side and slightly less to the pressure side, then the problem of symmetry could be taken care of as well. The effects of varying the subdivision parameter on the pressure side only are shown in Figure 13.

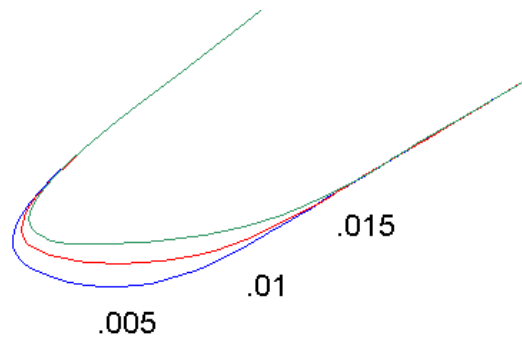


Figure 13. Effect of Subdivision Applied to the Pressure Surface

With a reasonably well-fitted representation of the Sanger geometry in hand, as well as a procedure to produce it, the next step was to compare its performance with that of the original using the RVC3D CFD code.

C. IMPLEMENTATION OF CFD TOOLS AND PROCEDURES

The first step in implementation of the CFD tools, after becoming familiar with their structure and operation, was the generation of a suitable computational grid. Since a method for generating a grid directly from the Bezier control points does not exist (although it was proposed as one area of extension to Abdelhamid's work), an alternative was employed. As discussed, TCGRID was utilized to generate the grids for this project but first, the blade geometry had to be translated back to MERIDL format for

incorporation into the TCGRID input file. As part of BLADE-3D, Major Abdelhamid created a routine which takes points from the fitted Bezier surfaces and creates 2-D blade profiles along conical sections similar to that required by the MERIDL format. The output from this routine can be expressed in either Cartesian or cylindrical coordinates. The cylindrical coordinate version can be easily put into MERIDL0 form and then appended to the standard TCGRID namelist input (pre-existing for the Sanger rotor), to create a complete input file (Appendix E). This was the technique used throughout the present study.

First attempts to generate the grid uncovered an interesting problem. While the BLADE-3D code was capable of outputting a MERIDL-like representation of the blade, it created anomalies at the trailing edge which frequently resulted in a negative Jacobian and subsequent rejection by the RVC3D flow code. Negative Jacobians are indicative of negative cell volumes, or places in the grid where grid lines cross unexpectedly and inappropriately. TCGRID generates a C-grid centerline which departs the trailing edge of the blade toward the grid exit, and from which the J grid lines project outward toward the grid boundary. The problem in this case was that the grid centerline did not always depart directly from the trailing edge but from a point two or three cells removed on the pressure surface of the blade (a result of BLADE-3D not dividing the mathematical listing of the blade profile precisely at the trailing edge). This caused some of the upward (suctionward) projecting J grid lines to have to ‘turn the corner’ around the real trailing edge and most of the time, this did not happen correctly. The grid lines passed through the trailing edge instead, hence the negative cell volumes, etc. While it was possible to finesse the input file to deal with this problem, a broader solution was sought and ultimately found. It was determined that by making small changes to the original BLADE-3D subdivision scheme used to define the fitted blade geometry, the problem with the BLADE-3D output could be almost alleviated, thereby precluding the subsequent issue with TCGRID. Resolution of this problem resulted in the creation of suitable grids and enabled the effort to proceed forward into working with the flow code.

Like TCGRID, initial attempts to apply RVC3D to compute the flow were not without problems. Major Abdelhamid used RVC3D to verify the accuracy of his Bezier

geometry fit and also to investigate the effects of forward and aft sweep on the Sanger geometry. Since he had relatively few runs to perform, he was able to carry each run out to 3000 iterations, a total certain to achieve convergence on all but the most complex flow cases; with convergence being defined as a three order-of-magnitude drop in the residual for the numerical method utilized. Such a run required about two days to complete on an SGI Octane workstation of the type used in the present work and given the far greater number of runs required, it was decided that 3000 iterations would be an unacceptable number. Initial runs of the baseline or fitted Sanger geometry were performed at 1500 iterations and did not achieve convergence. Subsequent 2000 iteration runs were performed which did not converge either. Various modifications to the computational parameters such as Courant number and levels of implicit residual smoothing in the pre-existing RVC3D input file for the Sanger rotor did little to change the convergence rate.

As discussed previously, the design intent for the Sanger rotor was for relatively high loading, i.e. operation close to stall. Due to the more complex flow patterns encountered in this regime, CFD computations of such flows require considerably longer to converge to the accepted level of accuracy. Calculation time can be cut drastically simply by choosing a less complex flow regime to study, one not so close to stall and therefore not subject to complicated flow separation issues. The decision was made to use a lower value for exit static-to-inlet total pressure ratio, 1.19 vs. the 1.22 value used in previous analyses of the Sanger rotor. This point was chosen as the design intent for this exercise, and all subsequent RVC3D runs were performed there. The necessary three order-of-magnitude convergence criterion was easily met within 1500 iterations, a computation that required slightly less than 24 hours on the Octane. That was considered acceptable and the work moved forward.

The first task in using the flow code was to verify the accuracy of the BLADE-3D fit to the original Sanger geometry by comparing performance at the design point. The results of that comparison are shown in Figures 32 and 33 in Section V.

D. AERODYNAMIC OPTIMIZATION PROCEDURE

1. Random Variation of Control Points

The first step in formulating the optimization procedure for the Sanger rotor was to choose an objective function and any constraints that would be placed upon the process (Appendix C). After some deliberation, it was decided that mass flow rate would be a good choice for the objective function since pressure ratio and efficiency are often targeted in an engine design, and improving mass flow would probably require the optimization of passage shape rather than changes in blade turning. Also, for the conditions of this exercise, changes in mass flow rate required changes in only one flow variable, inlet Mach number, a factor that would simplify and shorten the required sensitivity analyses. It was decided to require that there would be no loss in adiabatic efficiency during the process since decreases in efficiency are never a goal of good design. The only other design constraint, except for those imposed upon the movements of control points, was a requirement for positive blade thickness. As a matter of procedure, it was decided that the input values for the grid generation program and for the flow code would remain as consistent as possible so that any changes in the objective function would be solely due to changes in the blade geometry. For that reason, it was decided to terminate the optimization procedure if a converged solution could not be obtained without changes to the grid or the input boundary conditions.

Before the actual optimization process could begin, some ground rules for control point movement had to be set. First of all, it was decided that the locations of the bottom row of control points, those in the hub region, would not be changed at all during the exercise. This would provide a stable frame of reference for all modifications to the blade and would preclude any geometry changes that would require modifying the hub itself. Secondly, a similar decision was made regarding the control points along the leading and trailing edges of the pressure and suction surfaces except when moved by the sweep mechanisms contained in BLADE-3D. By limiting independent movement of these points, it was possible to maintain a fairly consistent chord length, thereby avoiding deviations in aspect ratio and solidity. An added benefit was that a reasonably constant thickness was maintained at the leading and trailing edges and changes in the leading and

trailing edge shape parameters were avoided. Movement of the off-blade control points at the tip were only allowed in the axial and tangential directions to prevent any significant changes in the radial dimensions of the blade at the tip, thereby avoiding redesign of the outer case wall.

So the options for control point movement during the optimization process were limited to the four center off-blade points on both the pressure and suction surfaces with these points being moveable in all directions – axially, tangentially, and radially. As mentioned, the center points at the tip on both surfaces could each be moved in only two directions. The result was an optimization problem with 32 variables and because of this high number, it was decided at first to investigate using a Monte Carlo or random variation technique. Figure 14 shows the possible variations in control points on the suction side.

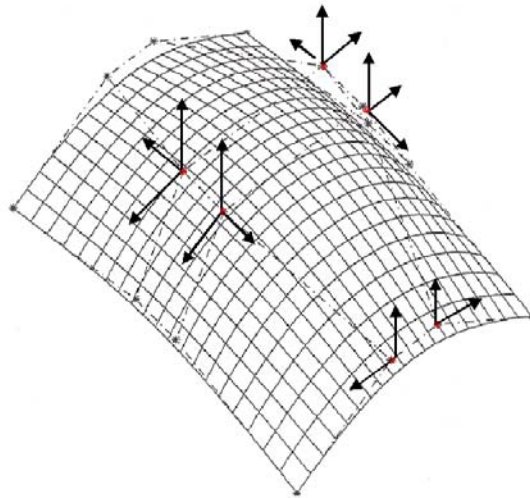


Figure 14. Moveable Control Points

To further limit the scope of the random variation effort initially, and to isolate the effects of the movements of suction side vs. pressure side points, it was decided to look at the center off-blade points by themselves, but only moving them in two directions. This served to lower the number of random variables to 8. The movements of these points was limited to approximately 10% of the chord length in the axial direction

and 5% of the thickness in the tangential direction and a FORTRAN routine, RANDCP, was written to produce random variations subject to these constraints (Appendix G). One hundred RVC3D runs were made during this portion of the exercise and a representative plot of the results is shown in Figure 15.

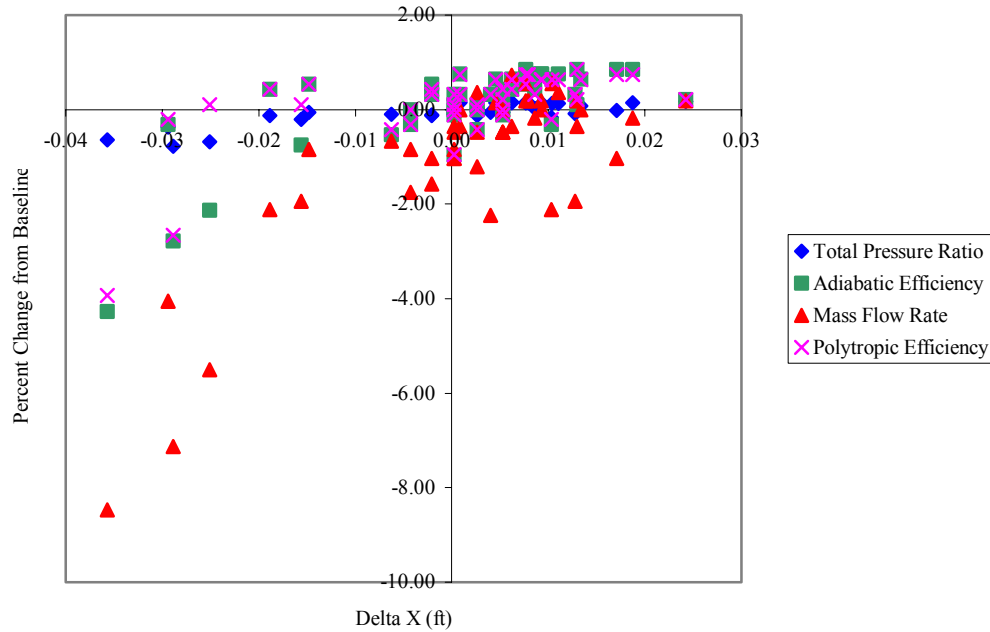


Figure 15. Example – Random Variation of Suction Surface Control Points

From the plot, it is seen that the random combination of new suction surface control points produced in this phase achieved very small if any positive changes in mass flow rate. On the contrary, many of the runs produced substantial decreases in flow rate or in many cases, no solution at all. In roughly one third of the 100 test cases tried, the flow code failed to converge to a solution. The observation that some of the runs produced improvement in blade performance, however, was a positive indicator that there was potential in the optimization effort.

A similar procedure was performed for the center off-blade control points on the pressure side. Again, 100 test runs were conducted using the same constraints as for

movement of the suction side points in the axial and tangential directions. The results of these runs are presented in Figure 16.

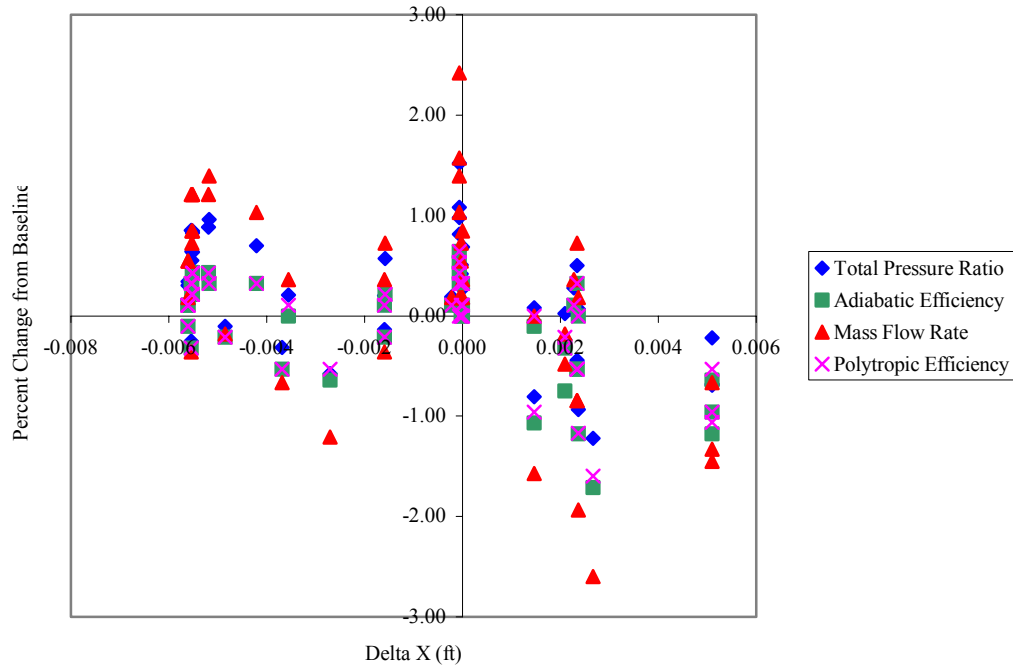


Figure 16. Example – Random Variation of Pressure Surface Control Points

The above figure shows that moving the pressure side control points seemed to have a more beneficial effect on mass flow rate than did that of the suction side points. For the pressure side, we see one combination that yielded a 2.5% improvement whereas the maximum for the suction side was about 1%. A generally more positive trend is noted as well; that is, there are fewer negative results with lesser magnitude than for the suction side. It should be mentioned also that out of the 100 cases run for the pressure surface, fewer of them failed to converge, an indication that the CFD code was more tolerant of perturbations in the pressure side flow field. This fact would be supported by the results of the later optimization approach.

Based on these results, it was decided to pursue a more structured and orderly approach to the optimization but first, an examination of forward and aft sweep was conducted.

2. Effect of Forward and Aft Sweep

A series of runs was performed to look at the variation in mass flow rate and the other blade performance parameters with application of BLADE-3D's built-in sweep functions. As previously mentioned, there are two – one that moves only the tipmost row of control points and one that moves the outer two rows to achieve a more gradual sweep effect from the midspan outward. These modes were identified as Sweep 1 and Sweep 2 respectively by Abdelhamid, and a comparison of both modes to the baseline shape utilizing 10% forward sweep is shown in Figure 17 (the magnitude of sweep is expressed as a percentage of the chord length).

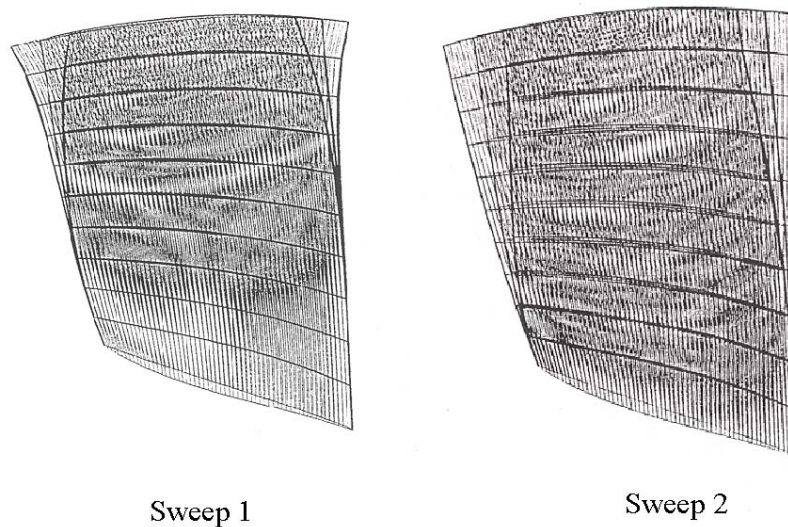


Figure 17. Sweep Manipulation in BLADE-3D

Examination of the two sweep modes was performed in 5% increments. The results are shown in Figures 18 and 19.

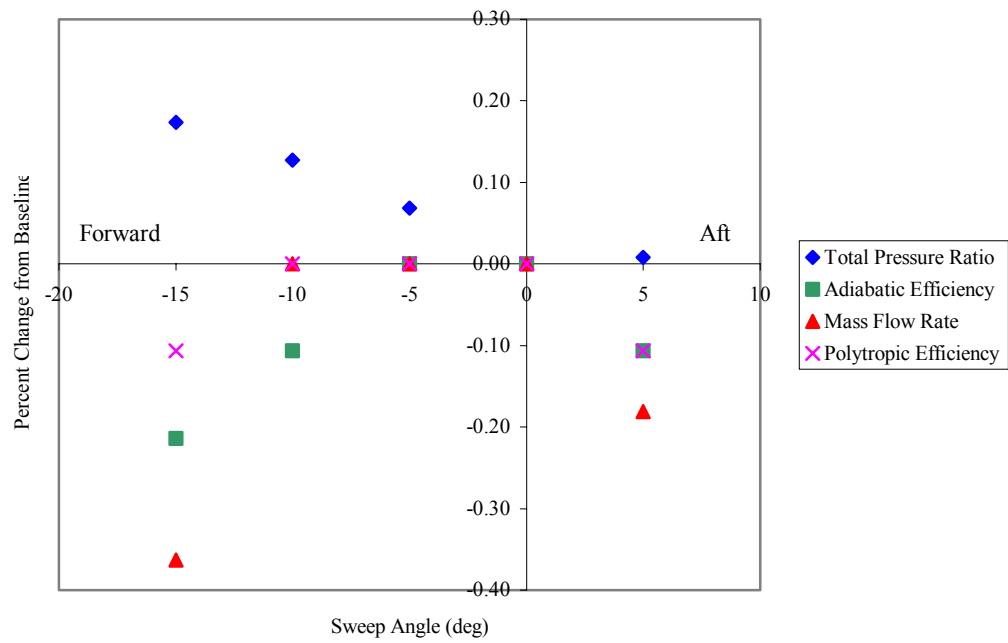


Figure 18. Effect of Sweep – Sweep 1

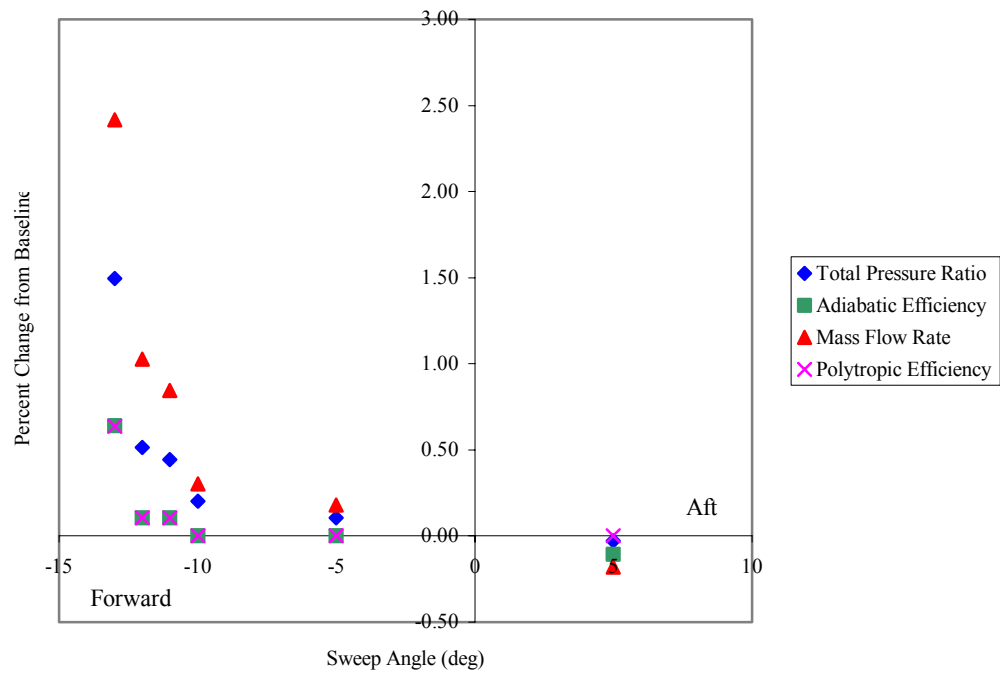


Figure 19. Effect of Sweep – Sweep 2

The figures show that Sweep 1 provided essentially no improvement in mass flow rate in either direction. All blade performance parameters decreased with sweep with the exception of total pressure ratio which improved slightly with aft sweep, and much more substantially with forward sweep up to a maximum of about 15% beyond which no solutions were obtained. Sweep 2 had a much more dramatic effect, and it can be seen that there was considerable improvement in all parameters with forward sweep, and a comparable decrease with aft sweep. The trend appears definitive. It was decided, based upon these results, that further efforts involving sweep would focus exclusively on forward sweep since aft sweep showed no improvement whatsoever in mass flow rate.

Since sweeping multiple rows of control points (Sweep 2) had a greater positive effect on the performance of the blade than did Sweep 1, the geometry package was modified to enable sweep of all three outer rows of points independently. The modification was made by implementing a Sweep 1-type routine at each row, which could then be applied in concert to achieve a variety of sweep effects. This change enabled a sweep optimization process to be performed, the results of which will be discussed later.

3. One-dimensional Search Technique

a. Pressure and Suction Side Control Points

Since the random variation of control points described previously yielded less-than-hoped-for results, an approach based upon the technique outlined in Section III was implemented. A one-dimensional search scheme was performed on the same center pressure side control points, this time using the radial direction since it had been excluded from the previous examination. The problem required a 4-dimensional direction vector to be determined by sensitivity analysis. This sensitivity analysis required that the radial component of each control point be incremented independently and positively by .001. An abbreviated RVC3D run of 200 iterations was then performed for each to determine the resulting direction of movement of the objective function (mass flow rate or more simply, inlet Mach number, which could be read directly from the RVC3D output). An

abbreviated run was also conducted for the baseline blade for comparison purposes. It was discovered that radial movement of the center points toward the edges; i.e., the hub for the inner points and the tip for the outer points, resulted in increases in inlet Mach number. This resulting vector was then added in increasing multiples to the original radial components of the control points to complete the optimization. This procedure was performed until a drop-off in efficiency was noted.

It should be mentioned that no attempt was made at this point to use the gradient of the objective function in the optimization process. It was decided to keep the components of the optimization vector equal in magnitude in order to keep a single control point from dominating the process at the expense of the others. Also, .0001 was used as the increment in the optimization vector itself rather than the .001 used in the sensitivity analysis. This enabled closer control of the changes in the locations of the control points and would prevent, it was felt, rapidly passing by the closest point of approach to the maximum. Once the vector was determined, the optimization procedure was performed by conducting concurrent RVC3D runs to full convergence, utilizing increasing multiples of the optimization vector. The results of these runs are presented in Figure 20.

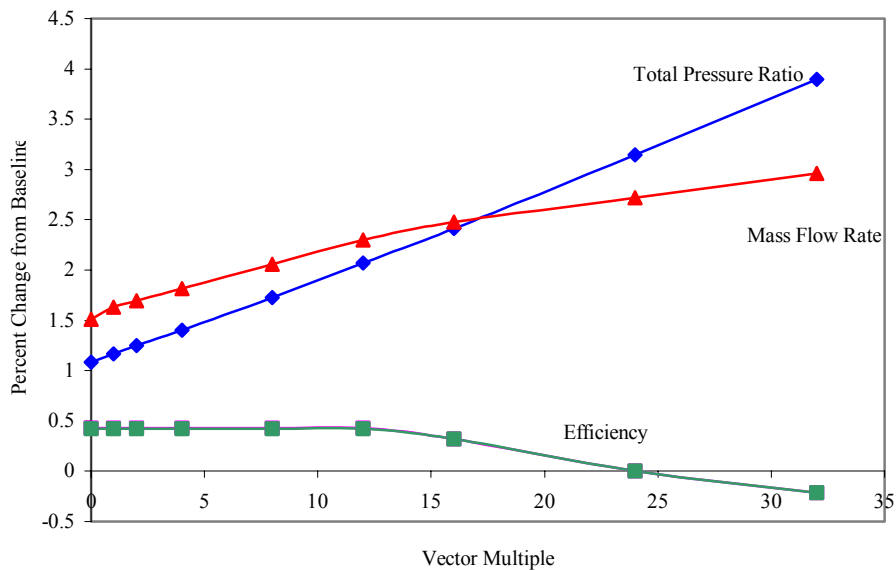


Figure 20. Pressure Side Radial Optimization

The figure shows that repeated application of the optimization vector resulted in ever increasing improvement in mass flow rate, as well as total pressure ratio. As mentioned, the procedure was carried out until the adiabatic efficiency dropped from its original value which occurred after about 24 multiples of the vector. There appears to be a knee in the curve at approximately the 16 multiple point after which the rate of increase in mass flow rate is reduced and the efficiency begins a more rapid drop off. The cause of this knee is unknown. It can be seen that the total pressure ratio continued to increase at a fairly constant rate throughout. The improvement in mass flow rate achieved during this portion of the exercise was greater than that achieved through the random variation procedure and was achieved more rapidly, predictably and repeatably. It validated the notion that an automated procedure consisting of a systematically applied optimization scheme indeed held promise for further investigation.

Given the initial success of the systematic approach outlined above, it was applied to the entire 32-variable optimization problem defined at the outset. The four center control points on both sides, as well as the middle tip points, were moved simultaneously in a manner determined by a similar sensitivity analysis procedure. The same incrementation scheme was used with a similar concurrent method of applying the resulting optimization vector. Again, the idea was to apply the vector until a drop in efficiency was noted, or until it was obvious that the maximum improvement had been attained. Figure 21 shows the results of the first run.

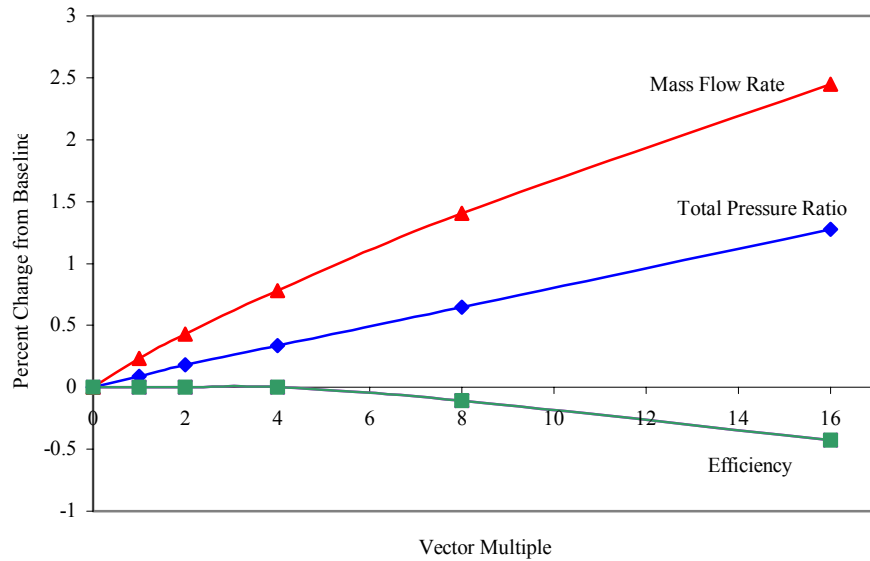


Figure 21. Sanger Rotor – Optimization Run 1

It can be seen in the above figure that the efficiency dropped off fairly early, around the 5th multiple, despite the fact that increases in mass flow rate and total pressure ratio occurred out through the 16 vector multiple point and apparently beyond. Given that result, it was believed that a second run in which adiabatic efficiency was used as the objective function might be useful since an increase in efficiency beyond the initial value would allow further effort toward improving mass flow rate. The second run was conducted in the same manner as the first (with the hope that mass flow rate would not decrease while attempting to improve efficiency). The results of the second run are presented in Figure 22.

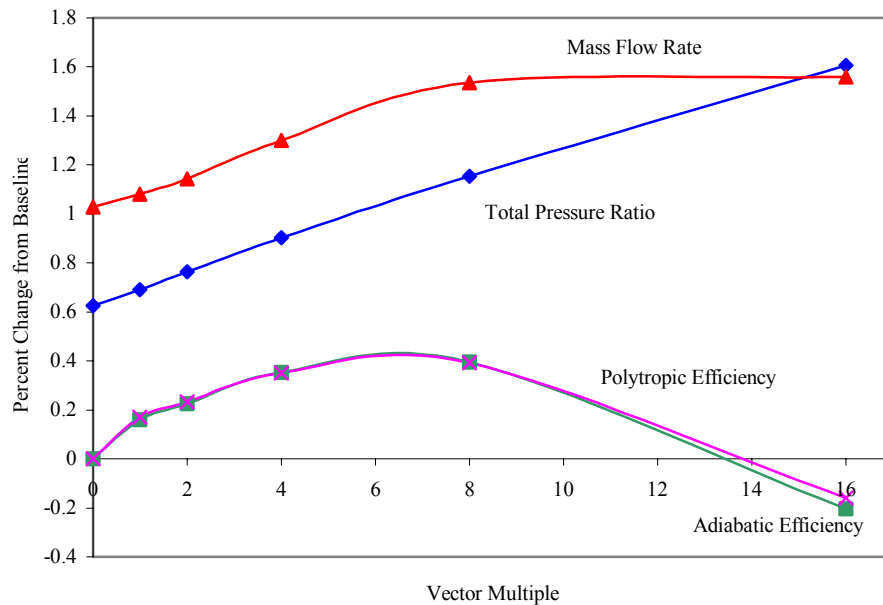


Figure 22. Sanger Rotor – Optimization Run 2

As shown above, the second run was in fact successful in achieving an improvement in adiabatic efficiency with the added welcome outcome that both mass flow rate and total pressure ratio were also improved. Polytropic efficiency was also tracked since it is a measure of merit that does not depend on the changing pressure ratio. The starting points for this run were the values of the parameters at the 5th multiple in run one. The peak of the efficiency curve occurred at just over six in this run, at which point an additional .5% improvement in mass flow rate was realized. The third optimization run was begun using the parameter values at that point, having again established mass flow rate as the objective function. The results of Run 3 are shown in Figure 23.

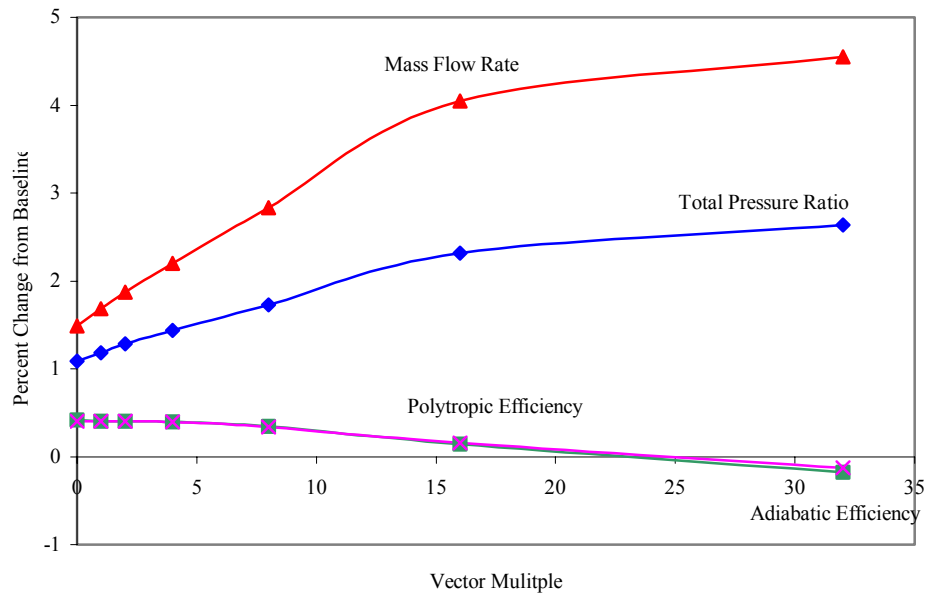


Figure 23. Sanger Rotor – Optimization Run 3

The results shown above were highly encouraging at first given that the apparent outcome after the first three optimization runs was an improvement of better than 4% in mass flow rate along with an increase in total pressure ratio of 2%+. However, all was not as it seemed. As before, the RVC3D runs for the increasing vector multiples were run concurrently to minimize wall clock time for the optimization process. The grids generated were not examined in detail in advance and it was not until afterward that it was discovered that blade thickness had become an issue. It was readily apparent in looking at the grid for the 32nd multiple that the thickness had in fact become negative, which was obviously unacceptable. It was initially surprising that RVC3D actually achieved a converged solution with non-physical boundaries. It served to show that the computer program cannot recognize whether the input geometry is physically possible or not. Figure 24 depicts the thickness problem observed for multiple 32 as depicted by I-DEAS.

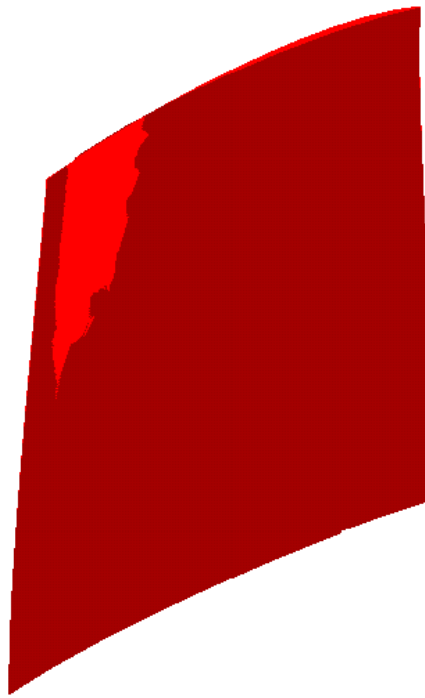


Figure 24. Sanger Rotor – Lack of Thickness during Run 3

This development made it clear that a check of blade thickness would be required in the optimization process. The thickness calculation scheme and FORTRAN code previously discussed were formulated at this juncture and applied to the blade attained after vector multiple 32 in Run 3. As observed, the thickness calculation produced a substantially negative result in the forward region between midspan and the tip. Going back through the results from Run 3 to find the multiple where the blade still maintained a reasonable amount of positive thickness throughout, a new optimization run was begun at point eight.

For the fourth optimization run, the procedure was modified such that before the flow code was used, the thickness was checked by both the FORTRAN routine and a visual inspection in I-DEAS. If thickness was found to be negative anywhere in the blade, then the closest control points on both surfaces were moved away from each other tangentially enough to achieve positive thickness. This movement was accomplished manually by simply changing the y-coordinate of the specified control point in

increments of .002 until blade integrity was restored. These changes were then incorporated into the geometry for the run through RVC3D. For Run 4, the process became a multidisciplinary one in which structural analysis tools were used in conjunction with the flow code to produce an acceptable result. The results for the fourth optimization run are shown in Figure 25.

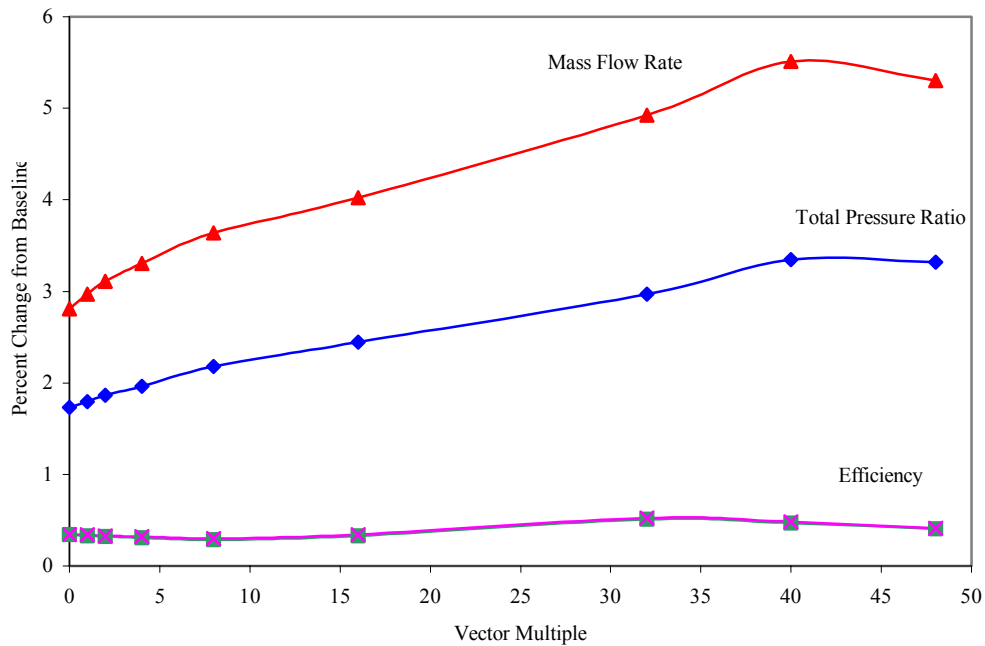


Figure 25. Sanger Rotor – Optimization Run 4

The figure shows that continued progress was made in the improvement of mass flow rate; ultimately achieving an approximate 5.5% gain with an accompanying increase in total pressure ratio. The efficiency maintained a slight improvement as well. The fact that the process continued as long as it did was somewhat surprising given that there were thickness issues from the very beginning and the geometry was ‘brute-forced’ into remaining positive. Finally, at the 40th multiple, there was a drop off in mass flow rate, which signaled closest passage to the maximum and an end to this phase of the optimization process. Because of the thickness issue, it was decided that there probably wasn’t much to be gained by performing another sensitivity analysis and perhaps

proceeding in a different direction with the same process. The decision was made to proceed to sweep as a method for further improving the performance of the blade.

The thickness issue necessitated the need to incorporate a structural analysis procedure into the process. I-DEAS was selected, and considerable effort was expended learning to use it; especially in the process associated with creating IGES files to import the geometry. Several weeks of work were required to ‘break the code’ on this and several other issues associated with using these tools. Those issues will be discussed more fully later in this section.

b. Forward Sweep

As a way to get a feel for how forward sweep should affect the performance of the so-far partially optimized blade, it was decided to perform an optimization procedure on the sweep function itself, utilizing the baseline blade, and then to apply those changes to the results of Run 4. A sensitivity analysis similar to those already described was performed for the sweep function at each row of sweepable control points. A gradient of the objective function with sweep was calculated for each row and then normalized by dividing through by the largest. Sweep was incremented in each row in three different ways as shown in Table 3.

	Smaller <u>Increments*</u>	Equal <u>Increments</u>	Larger <u>Increments</u>
Inner Row	0.9375	1	1.067
Middle Row	1	1	1
Outer Row	0.7292	1	1.37

*Smaller increments represent normalized gradient

Table 3. Sanger Rotor Sweep Optimization Scheme

All three methods involve using the row with the largest gradient as unity. The smaller increment applied the relative gradients directly while the larger increment applied the reciprocal such that the row with the smallest gradient changed the most per vector multiple. The results of the methods are shown in Figure 26.

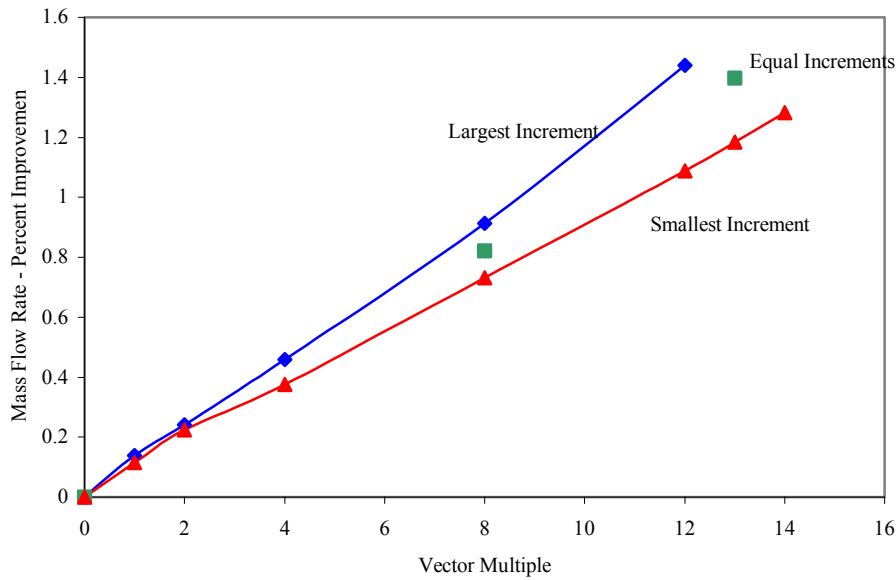


Figure 26. Sanger Rotor – Optimization of Sweep

As expected, the larger increment method showed the most rapid improvement in mass flow rate and achieved an overall improvement of about 1.5%. There was a possibility that one of the other two methods, while slower, might converge to a higher end point, which would make it the method of choice. As is seen in the figure, that did not happen and the larger increment values were chosen for incorporation.

The results of the forward sweep optimization investigation were added to those for the four optimization runs accomplished previously to produce what was thought would be the final configuration of the optimized blade. This geometry was then passed over to the structural analysis program and to determine whether or not it would meet structural requirements.

F. STRUCTURAL ANALYSIS

1. Finite Element Analysis

Blade geometry information was imported into I-DEAS via the IGES file format (Appendix E). Since IGES supports the B-spline surface entity as an accepted data input, the control points for the Bezier surfaces defining the blade could be written directly into the input file. While learning how to create and translate IGES files took some time – it was essentially like learning a new computer language – the payoff was tremendous in that it ultimately allowed for very efficient transfer of information back and forth between the aerodynamic and structural analysis phases of the research. At first, all six Bezier surfaces were input into I-DEAS which resulted in a ‘part’ (as I-DEAS refers to it) composed of six separate components from which a solid is created. As input, the six surfaces formed a hollow tube object, for which end surfaces had to be generated, and then all eight surfaces stitched together to produce the solid blade. I-DEAS has various methods for accomplishing this, none of which worked very well for this geometry. After much trial and error and very little success, it was decided to reduce the input file to the pressure and suction surfaces only. After doing this, it was found that the corresponding corners of the two surfaces could be connected with lines and that four additional surfaces could then be produced using the ‘Surface by Boundary’ function of the Master Modeler. From there, the six surfaces could be stitched together to form a slightly modified solid blade. The resulting part was essentially the original blade geometry without the leading and trailing edges and it was felt that this would be acceptable for the structural analysis since those portions were a very small percentage (less than 1%) of the overall blade mass. This decision helped to streamline the input and modeling process considerably. Figure 27 shows the solid blade as produced by this procedure in I-DEAS.

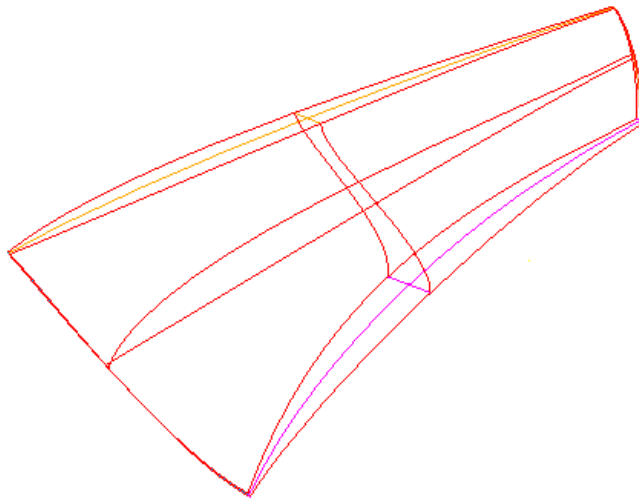


Figure 27. Solid Modeling of Sanger Blade with I-DEAS

Once a solid blade was generated, the meshing function of I-DEAS was used to complete the finite element model. The fidelity of the mesh was determined automatically by I-DEAS depending upon the dimensions and details of the part. It could also be selected by the user. Usually, the program generated as coarse a mesh as was feasible without violating the geometry requirements of the component tetrahedral elements, and this served to minimize solution times. As the blade became thinner during the optimization process, the mesh became finer and solution times increased substantially.

After meshing was complete, boundary conditions and loads were applied. The only boundary condition imposed for this blade was that it be clamped at the hub with no deflection allowed. Blade loading consisted of applying a rotation about the x-axis equivalent to the compressor speed and a distributed gas load on the pressure side of the blade. Both of these were easily performed in I-DEAS. The gas load utilized was calculated from the RVC3D output. Once boundary conditions and loads were applied, the finite element model solution could be performed.

Initial I-DEAS solutions for the baseline blade agreed very well with the results of the structural analysis for the Sanger rotor conducted by Hermann at NASA Glenn and also to the results obtained by Abdelhamid in his work [Ref. 1, 41].

2. Cold Shape Correction

As the blade became thinner and thinner during the optimization process, it became apparent through structural analysis that large deflections under load were creating a situation in which the blade no longer retained the shape for which the aerodynamic analysis had been performed. While this was true also for the baseline blade, the effects were far more pronounced in the modified blades. It was obvious that some sort of shape correction procedure had to be developed that would result in the blade assuming the proper aerodynamic shape after the loading was applied. This effort became the focus of the work for several weeks.

In Reference 4, Wennerstrom devotes a couple of pages to this issue and discusses the idea that the blade must be manufactured in one shape, with the knowledge that it will deform into a different shape when loaded, and that this different shape must conform to the aerodynamic design intent. He describes an iterative procedure in which structural analysis is performed to determine blade deflections, those deflections are subtracted from the design shape to create a new blade geometry and then this new blade is loaded to determine the new deflections, and so on. This procedure is performed until the deflected shape of the revised blade geometry matches the original aerodynamic design.

A technique to accomplish this was developed, but required some time to perfect since I-DEAS does not provide a direct output of deflected geometry, not to mention one in BLADE-3D control point format. A way had to be found to calculate new control points for a deflected blade geometry before a correction procedure could be established. It was determined that the BLADE-3D surface point output was quite useful in this regard. For a given set of control points, BLADE-3D can produce a set of Cartesian coordinate surface points for the pressure and suction surfaces of the blade. In the I-DEAS universal data file, original locations and deflections of the nodes in the finite

element model are provided in tabular format. With these pieces of information, the closest node to each surface point could be calculated, and then the deflection of that node applied to the point to produce a surface model of the deflected blade. Those points could then be used by BLADE-3D to calculate a new set of control points for the deformed model. In addition, the nodal deflections could be subtracted from the original surface points to produce a 'predeflected' blade i.e., a corrected blade shape for further structural analysis. FORTRAN routines to calculate the closest nodes and to produce deformed and 'predeflected' surface geometries (CNODE and DGEOM) are given in Appendix G.

Once these techniques were developed, an iterative correction was attempted for the baseline blade as a test of the procedure, since the smaller deflections encountered there held better promise of success and validation of the method. After several iterations, it was discovered that the process was diverging rather than converging on a new blade shape. Repeated attempts produced the same result and reexamination of the process achieved nothing toward finding the problem. However, by switching from using linear statics to non-linear statics on the advice of NASA Glenn, convergence was obtained [Ref. 42].

Linear static analysis, while suitable for very small deflections, was not working here because the deflections were large relative to the size of the blade. Nonlinear statics applies the loading incrementally, which is in fact appropriate since a spinning rotor takes time to come up to speed. The solution is calculated using a varying stiffness matrix as the load is applied, and this results in smaller stresses and deflections for a given load case. The cold shape correction procedure, with nonlinear analysis, converged successfully to a suitable 'predeflected' geometry for the baseline blade. [The results for the cold shape correction of the Rotor 67 Final design contained in Section V were very similar to those attained for the baseline blade in terms of number of iterations and accuracy in matching the deflected blade to the intended geometry.] The viability of the method was well-demonstrated. Figure 28 provides a visualization of the geometry change produced by the cold shape correction procedure.



Figure 28. Blade Iterations during Cold Shape Correction

Unfortunately, the attempted cold shape correction of the optimized Sanger rotor did not work out as well. Because of the blade's thinness, the deflections encountered under load were considerably higher than for the baseline blade, as is shown in Section V. The correction procedure did not converge on a suitable cold shape nor did the deflections diverge. After a few iterations, the excess deflections became almost stable. Therefore, a different approach was taken. The structural analysis was run for the optimized blade, and the deflections were obtained and subtracted to get the first cold shape. This cold shape was then loaded to achieve a new deformed blade, which was then run through RVC3D to determine its performance. The idea was that if the original optimized blade shape could not be achieved, then the best performance by a loaded blade would have to be accepted as the design. It was expected that this performance would be worse than before. Surprisingly, the new hot shape actually performed better than the design achieved through the previous optimization, so this new shape became the accepted design and it is this geometry that is described in detail in Section V.

A comparison of the performance of the optimized blade and the new shape achieved through the cold shape correction procedure is shown on the speedline graphs in the Sanger Rotor Performance portion of Section V (A-2).

G. ROTOR 67

The methods outlined above were applied in turn to NASA Rotor 67. The first task in the process was to achieve a BLADE-3D fit to Rotor 67, which was performed much in the same manner as previously described for the Sanger rotor. The only issue here was that the existing MERIDL file for Rotor 67 contained 14 section profiles to define the geometry, as opposed to the 11 which had been used for the Sanger rotor. Since BLADE-3D had been formulated using the Sanger design, the fitting logic involved dividing the Bezier surfaces into ten spanwise pieces based upon the 11 section profiles obtained from MERIDL. Therefore, the MERIDL geometry for Rotor 67 was redefined using 11 spanwise sections, and this was done by interpolating selected portions of the data. The BLADE-3D fit was then easily accomplished, and a Rotor 67 baseline geometry achieved.

The purpose of investigating a second rotor was to demonstrate the general applicability of the optimization method. To further that end, a different objective function as well as different search techniques were used. First, the objective function was chosen to be polytropic efficiency, and rather than shoot for an open-ended optimization result, at least in the initial control point variation, it was decided to see if a one percent improvement in efficiency could be achieved simply by varying the off-blade suction side control points in two dimensions. This decision was partly driven by time and by the fact that it was desired to avoid the extreme thickness changes observed in the Sanger rotor optimization. As mentioned, computing time is greatly increased as the number of design variables increases. The scheme chosen for this part of the investigation resulted in an eight-variable problem, much smaller than the 32-variable case looked at for the Sanger rotor. The reason for this reduction is that the objective function depends upon two parameters, total temperature and total pressure, which change in relative magnitude as the calculations inside RVC3D proceed toward convergence. Because of this, the runs performed for the sensitivity analysis had to be carried all the way to convergence to determine the true nature of changes in polytropic efficiency. A way had to be found to reduce the overall computation time, and this was done by reducing the number of variables.

The results for the Rotor 67 suction side control point optimization procedure are presented in Figure 29.

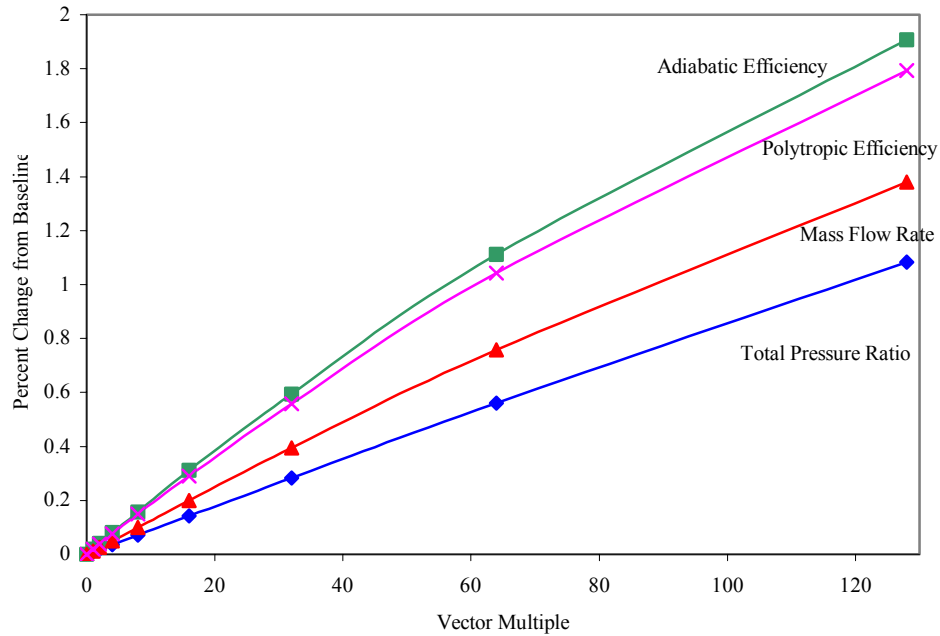


Figure 29. Rotor 67 – Suction Side Control Point Optimization

It can be seen that the desired one percent improvement in polytropic efficiency for Rotor 67 was easily achieved by the optimization scheme used. Also, it should be noted that the efficiencies improved to a higher degree than either mass flow rate or total pressure ratio, a result quite different from that observed for the Sanger rotor. This suggests that the optimization process can in fact be tailored to target improvements in selected performance parameters.

Forward sweep was applied to Rotor 67 as well in order to see if the efficiency could be further improved. It was decided to go ahead and use the larger increment method as described for the Sanger investigations and those increments are shown in Table 4.

	<u>Increments</u>
Inner Row	4.55
Middle Row	1
Outer Row	2.14

Table 4. Rotor 67 Sweep Optimization Scheme

The results of the sweep optimization process for Rotor 67 is shown in Figure 30.

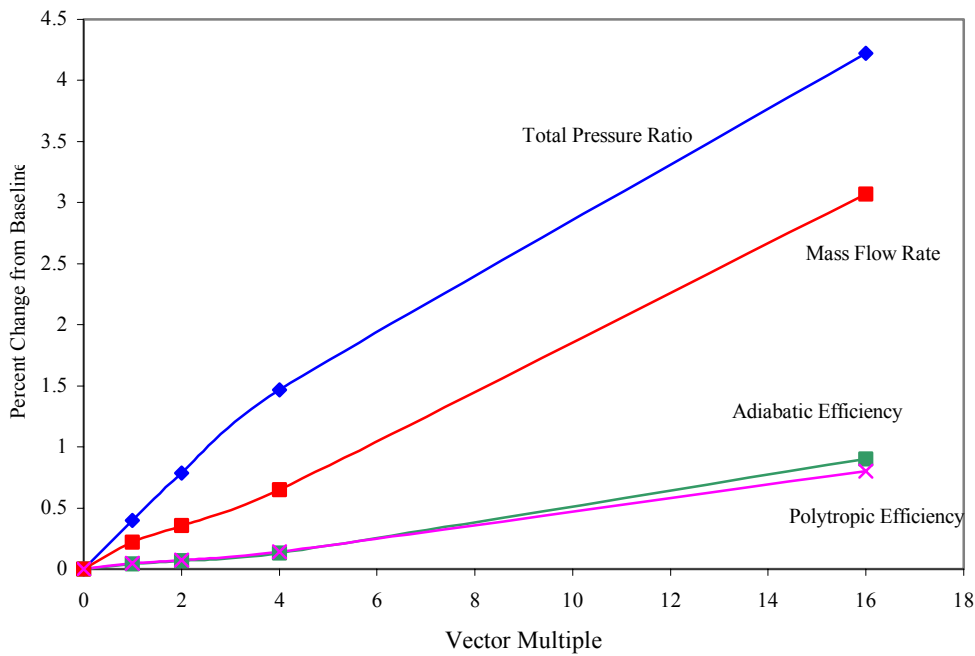


Figure 30. Rotor 67 – Optimization of Sweep

It can be seen first of all that the forward sweep process resulted in a much more dramatic shape change for Rotor 67 than it did for the Sanger rotor. Not only were the sweep increments larger at the one-third span point as well as the tip, the process was able to attain a higher number of vector multiples. The result was a blade which departs radically from the accepted paradigm in overall shape if not in thickness as observed

before. The performance of this blade is reported as ‘New’ under the Rotor 67 portion of Section V. As will be seen, it was not the end result of the process.

When the structural analysis was conducted on the Rotor 67 new design, it was found that the steady stress levels far exceeded the maximum for the chosen material, a high-strength titanium alloy typical of those used in bypass fans. The stresses in the new blade were on the order of 210,000 psi where the material could tolerate only about 120,000 psi. The observed maximum stress occurred at the leading edge where it joined the hub and was essentially a stress concentration which could have most likely been relieved by filleting; but that was outside the scope of this effort. It was decided to remove some (approximately 75%) of the sweep that had been applied in the earlier optimization process, and doing so achieved a design which met acceptable stress levels. This blade is what is referred to as the Rotor 67 final design and its details are reported in Section V.

The cold shape correction procedure was successfully applied to the final design to achieve the appropriate ‘predeflected’ geometry.

H. OPTIMIZATION ALGORITHM

A major intent of this study was to develop a methodology or algorithm for the automated design optimization of compressor blades. The processes and procedures developed through the investigations outlined in this section have been put together in flow chart format to visualize how such an automated procedure would look. That flow chart is presented in Figure 31.

For this procedure, one enters the upper left side of the chart with the baseline configuration expressed in BLADE-3D format. A search direction is defined through sensitivity analysis, and then the determination of the search distance is performed by the loop on the lower left. It can be seen that this loop contains features which check the thickness against some predefined minimum and then compares the value of the objective function with that from the previous run. It also checks to make sure that the constraint functions are not violated (here there is one, there could be several). Departure to the

right from this loop leads to the structural analysis and cold shape correction portions of the procedure. The diamond on the far right is that point at which the decision is made whether to accept the current design iteration, or to proceed in a different search direction to try to get closer to the maximum or minimum of the objective function.

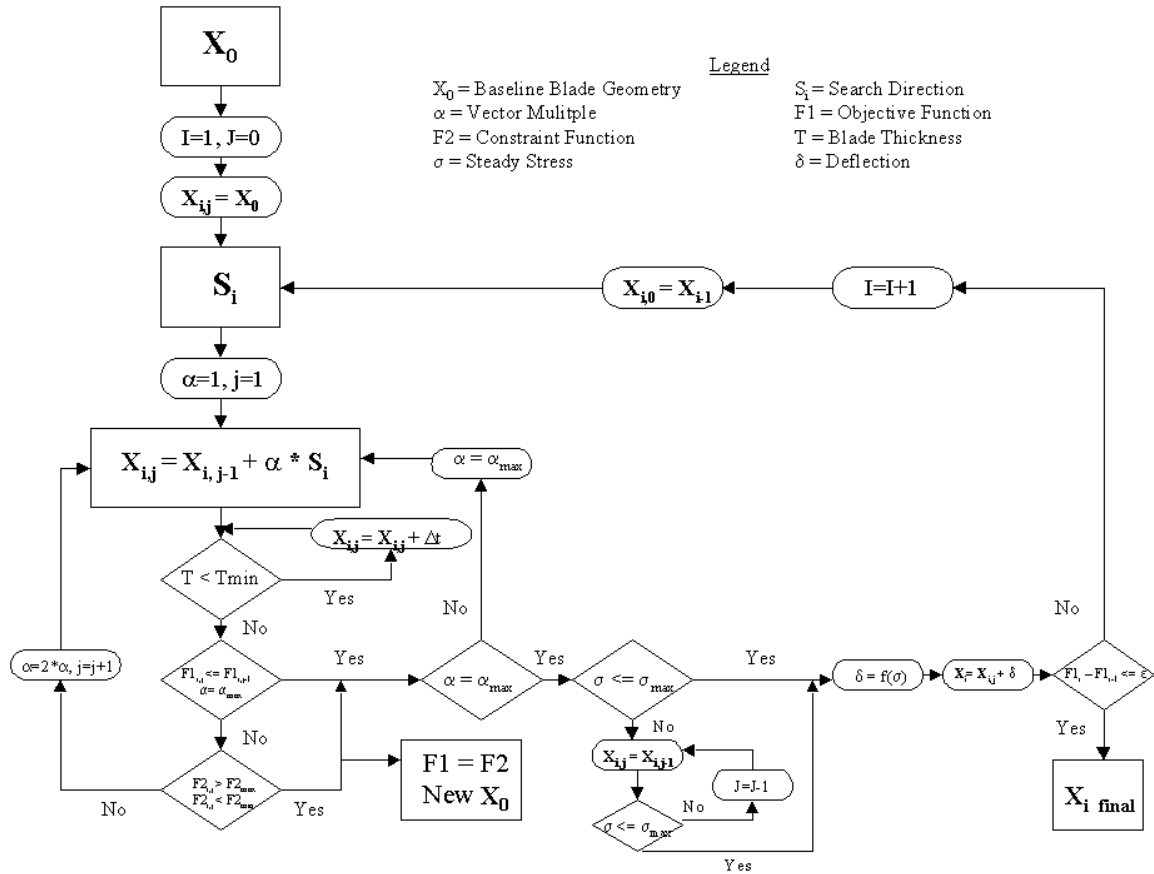


Figure 31. The Optimization Algorithm

This algorithm provides the foundation for a fully automated design optimization method although actual implementation in the course of the present study required hands-on manipulation. Data had to be organized and formatted in order to move it from one program to another. The procedure was performed however, with very little interference in terms of human decision-making in the design process itself, once objectives and constraints were determined. From that perspective, the goal of the research was

achieved. Considerably more programming work will be required to generate a real and wholly computerized capability.

The design improvements to the Sanger Rotor and Rotor 67 that resulted from the application of the algorithm are detailed in the next section.

V. RESULTS AND DISCUSSION

A. THE SANGER ROTOR

1. Overview

The Sanger rotor design was optimized using the procedure described in Section IV. An overall comparison of the baseline and optimized configurations is presented in Table 5.

	<u>Baseline</u>	<u>New Design</u>
Mass Flow Rate	16.55 lbm/sec	17.88 lbm/sec
Total Pressure Ratio	1.6	1.68
Adiabatic Efficiency	0.936	0.945
Polytropic Efficiency	0.94	0.949
Design Speed	27,000 RPM	27,000 RPM
Tip Inlet Relative Mach Number	1.19	1.21
Tip Forward Sweep	0%	12%
Weight Factor	1	0.4
Maximum Steady Stress*	31,100 psi	22,500 psi

* 110% design speed

Table 5. Sanger Rotor Optimization Summary

As the above data indicate, dramatic improvements in the overall performance of the Sanger rotor were achieved through the optimization process. Mass flow rate, which was the objective function for the exercise, increased by 8.1%. This improvement was most likely due to the two most prominent changes realized in the shape of the Sanger blade - substantial loss of thickness and the addition of forward sweep. The combined effect of these changes is a rotor with increased pumping capacity due to changes in passage shape with accompanying changes in the turning of the flow.

In addition to the improved mass flow rate, more modest gains were achieved in total pressure ratio and efficiency. The total pressure ratio across the rotor increased by 5% while the adiabatic and polytropic efficiencies increased by 0.9% each. The original goal for the optimization was to improve mass flow rate with no loss in rotor efficiency. The fact that efficiency as well as total pressure ratio improved along with the flow rate is a pleasant side benefit of the 3-D optimization process. Further discussion of the likely mechanisms behind these improvements will come in a following section which deals with the flow field.

As discussed above, the optimization process resulted in substantial decreases in metal thickness, particularly in the outermost regions of the blade span. The loss of thickness led directly to a large reduction in the mass of the blade. As can be seen above, the overall weight of the blade decreased by approximately 60%, a quite dramatic reduction and one that may in fact be impractical from an overall structural and manufacturing perspective. The non-linear static structural analysis performed on the optimized blade showed that it could withstand the steady static stresses and deflections induced by the operating conditions of the exercise; but a more in-depth structural analysis, to include dynamic response, unsteady effects and fatigue, would undoubtedly uncover issues [See Appendix A]. Even so, the severe thinning of the blade and the accompanying reduction in weight is an interesting and beneficial trend. The weight reduction led to a sizeable decrease in the centrifugal loading on the rotor at 110% design speed and, as shown in Table 2, there was a 28% decrease in the maximum steady stress; again, an interesting and highly desirable result.

2. Performance

A set of constant speedlines was constructed for the baseline and optimized Sanger rotors by performing CFD runs at various values of exit-static to inlet-total pressure ratio. The design value of this parameter for the exercise was 1.19 and for the speedlines, the values were varied between 1.16 and 1.22. The values for all other boundary and initial conditions remained constant (except for the Base 90% line where speed was changed). From the results, plots of total pressure ratio vs. mass flow rate and

efficiency vs. mass flow rate were constructed, which aptly demonstrate the performance improvement attained through the optimization process. These plots are presented in Figures 32 and 33.

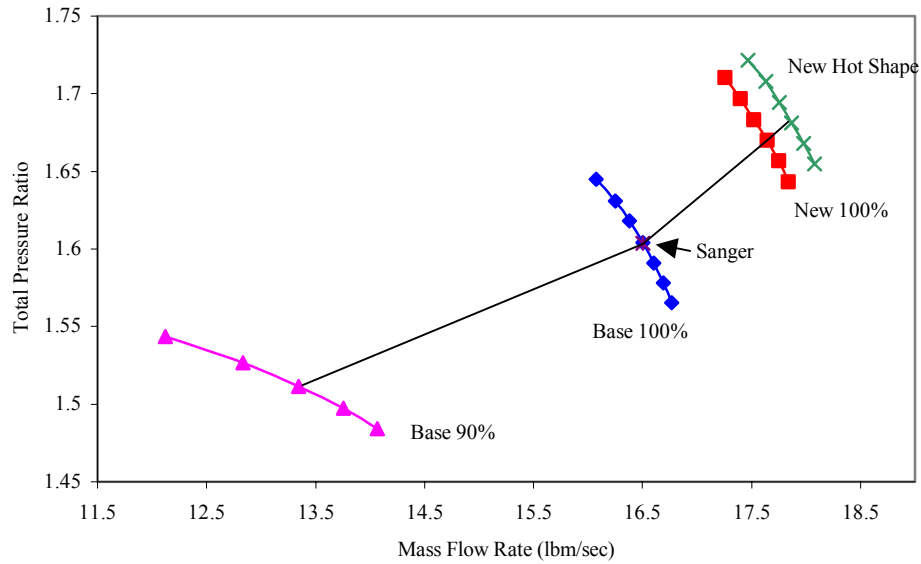


Figure 32. Sanger Rotor Performance

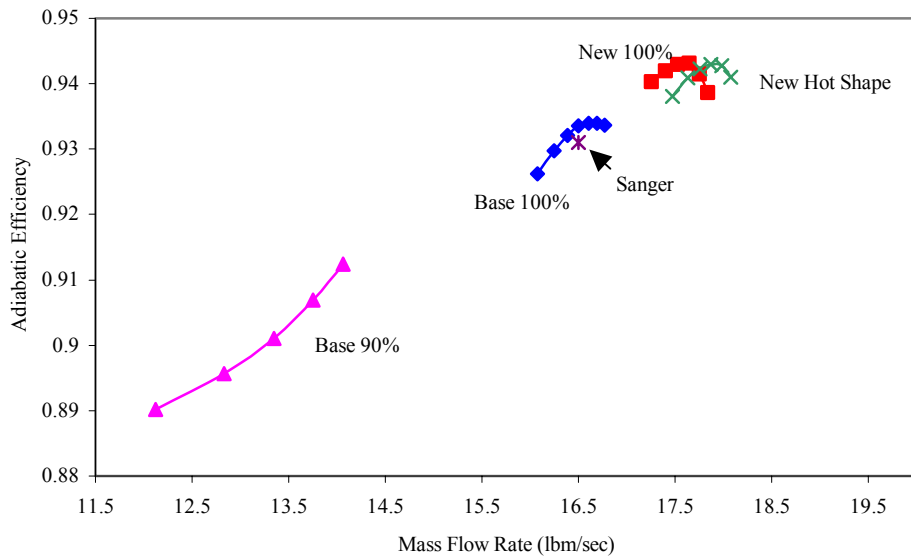


Figure 33. Sanger Rotor Efficiency

The results in the two figures provide a yardstick by which to measure the effects of the Bezier fit and optimization methodology on all areas of the rotor's performance. The data point representing the performance of the original Sanger rotor at the (exercise) design point is labeled 'Sanger' on both plots. This can be compared with the performance of the baseline or BLADE-3D fitted geometry by noting the location of the corresponding point on the 'Base 100%' speedline. It is seen that there is very good correlation between the performance of the original and fitted geometries, and that the fitted baseline was a good starting point for the subsequent optimization effort.

The 'Base 90%' speedline is plotted as a reference for the improvement achieved. It can be seen that at 100% speed, the mass flow rate is increased by an amount comparable to that which would be attained by operating the rotor at about 105% design speed. The implication is that the redesigned rotor would be able to produce the intended design mass flow rate at a lower speed; thereby decreasing the work input required from the turbine. For a given engine cycle requirement, an alternative benefit of the rotor redesign would be that it could provide the basis for a rotor design which would produce the same mass flow rate at the same drive-turbine speed but with a reduced annulus area. This would lead to a further reduction in blade mass, a decreased frontal area for the engine, and an overall decrease in weight and drag for the aircraft.

A similar observation can be made for the total pressure ratio. The design intent total pressure ratio could be achieved at a lower speed with the redesigned rotor or alternatively, a higher pressure ratio could be attained at the same speed, which, if this were the first stage in a multi-stage machine, could potentially lead to the requirement for fewer subsequent stages and an overall decrease in the weight, size and complexity of the compressor. The combined benefits of the improvements in mass flow rate and total pressure ratio are substantial. In a fan, this translates into an increase in available thrust as long as the low pressure turbine is capable of providing the required drive power.

As stated before, the improvement in rotor efficiency, while not specifically an objective of the optimization exercise, is beneficial. Improved compressor efficiency would reduce the required work input from the turbine and would result in some combination of decreased weight, potentially lower turbine inlet temperatures, less complexity, and lower fuel consumption and therefore, an overall enhancement in engine

economy. The nearly 1% improvement in adiabatic efficiency between the baseline and optimized or new configurations is clearly shown in the plot. Another interesting observation is that the application of BLADE-3D to approximate the original Sanger geometry in and of itself resulted in a small but definite improvement in rotor efficiency. This could be an illustration of the benefit of the Bezier geometry scheme in representing the 3-D blade as opposed to the MERIDL stack of relatively independent 2-D blade profiles. A smoother, less wavy shape might result in slightly fewer losses over the blade span and an overall slight improvement in efficiency. Abdelhamid found a similar result in his work on the Sanger rotor [Ref. 1].

3. Geometry

The overall impact of the geometry changes made during the optimization process have been presented and discussed. Figures 34 through 37 provide a graphical display of those changes and a basis for further discussion of their effects.

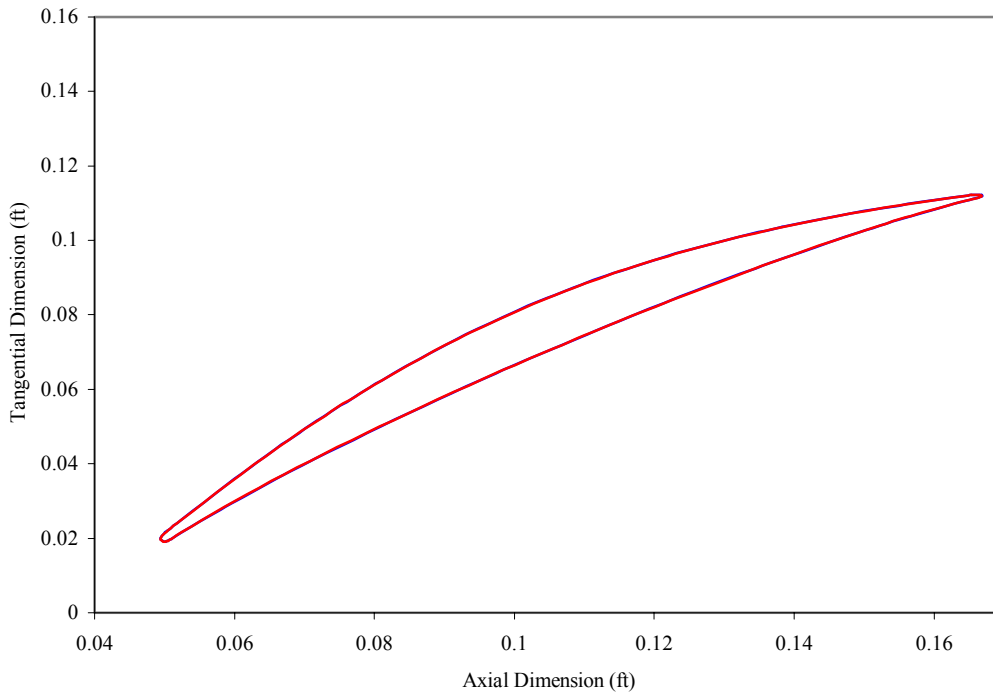


Figure 34. Sanger Rotor Geometry – Hub

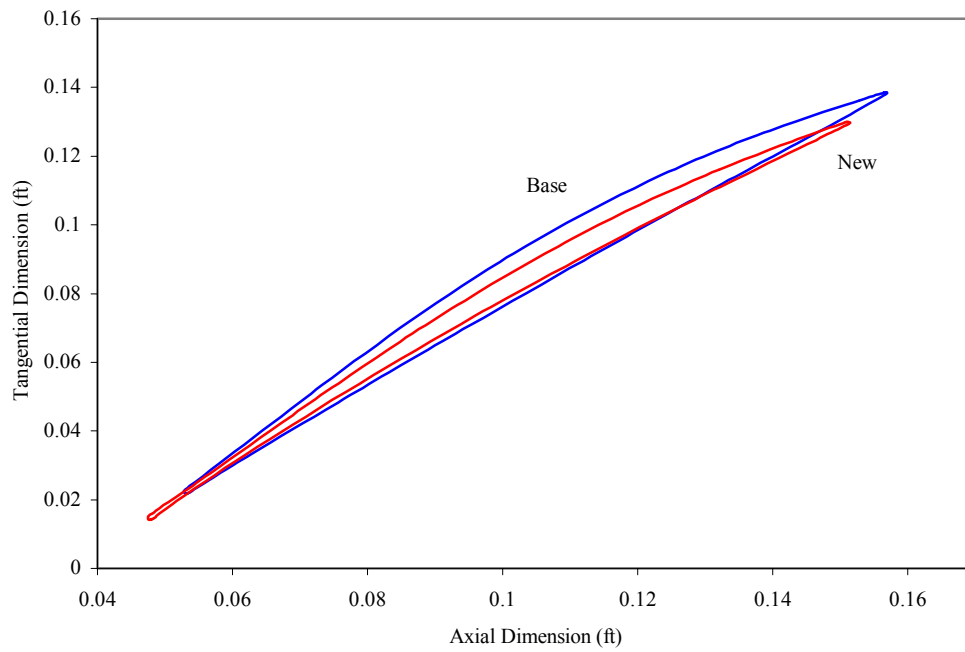


Figure 35. Sanger Rotor Geometry – 30% Span

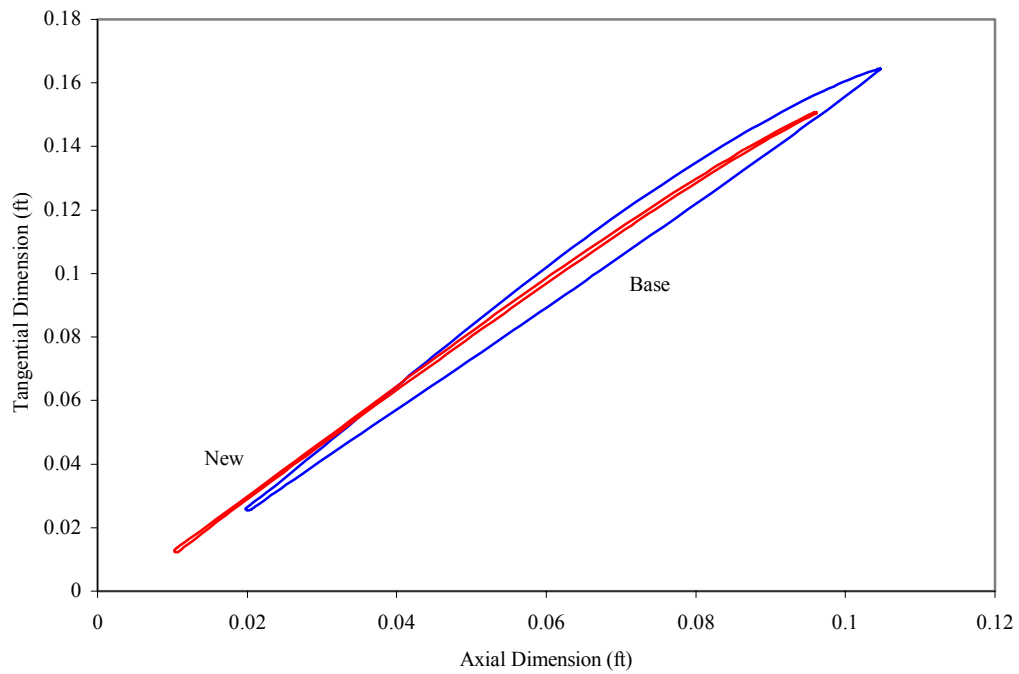


Figure 36. Sanger Rotor Geometry – 70% Span

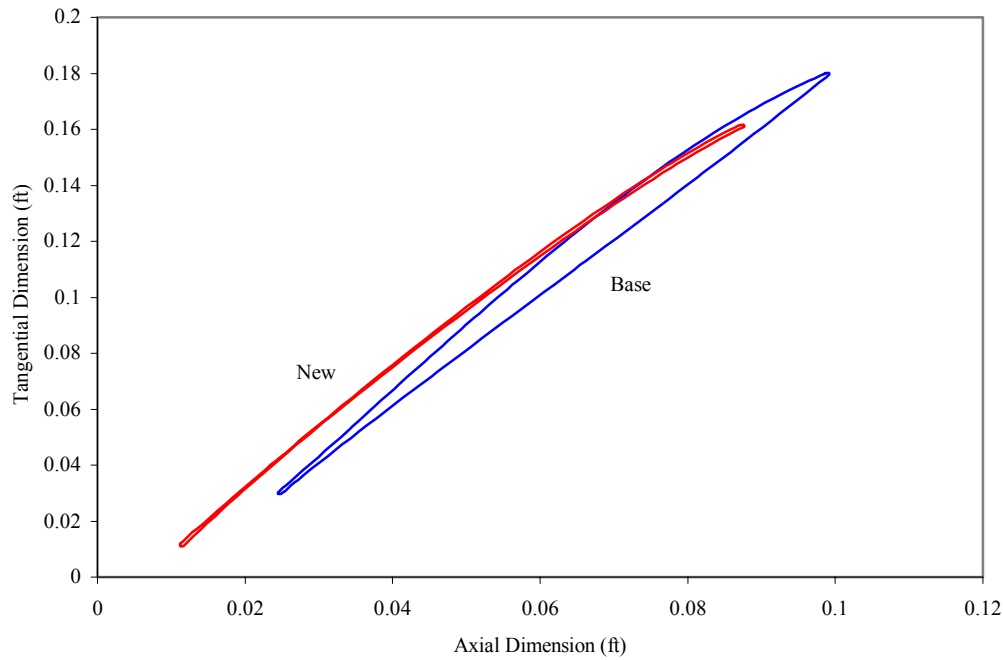


Figure 37. Sanger Rotor Geometry – Tip

The first figure compares the two geometries at the hub and it can be seen that they are identical. The bottom row of Bezier control points, which define the blade geometry, lie in the hub wall and were not moved in the optimization process. This was therefore the expected result.

At 30 percent span, a definite thinning of the blade is apparent as well as the forward sweep applied by moving the second row of control points. A small displacement of the blade in the direction of the pressure side can be observed in addition to the forward sweep toward the leading edge. This is due to the fact that the sweep programmed for this row of control points was an adapted version of the code used to sweep the tip in the original BLADE-3D, where the chord or stagger angle of the blade is much greater. The tangential component of the sweep function resulted in some translation rather than pure sweep. The effect here is minor but in future efforts, this feature of BLADE-3D should probably be modified.

The blade grows even thinner at 70% span, with the thinnest region (outside the leading and trailing edges) being just aft of where the leading edge Bezier surfaces join

with the pressure and suction surfaces. The blade is also displaced somewhat toward the suction side as a result of the cold shape correction procedure, which resulted in some tangential deflection from the original shape. It is interesting to note that the new geometry begins to resemble a forward-swept version of the suction surface of the baseline blade. This is probably due to the fact that the changes in the flow rate were much more sensitive to changes in the pressure side control points, and that movement of the suction side points were more likely to result in non-solutions. The optimization scheme ended up making the most dramatic changes to the pressure side, while leaving suction side relatively unchanged in comparison.

The geometry at the tip is a continuation of what is observed at 70%. The blade is forward swept, very thin and more highly cambered than the original blade. While the new geometry results in some very positive effects on the flow field, the extreme thinness must obviously be viewed with some skepticism, even though the blade passes muster when subjected to a steady static stress analysis. A more detailed discussion of the stress analysis results will be presented later.

Figures 38 through 43 are plots of chord angle, camber angle, and several thickness parameters as a function of spanwise location. They supplement the blade profile illustrations in understanding the changes to the geometry that occurred during the optimization process.

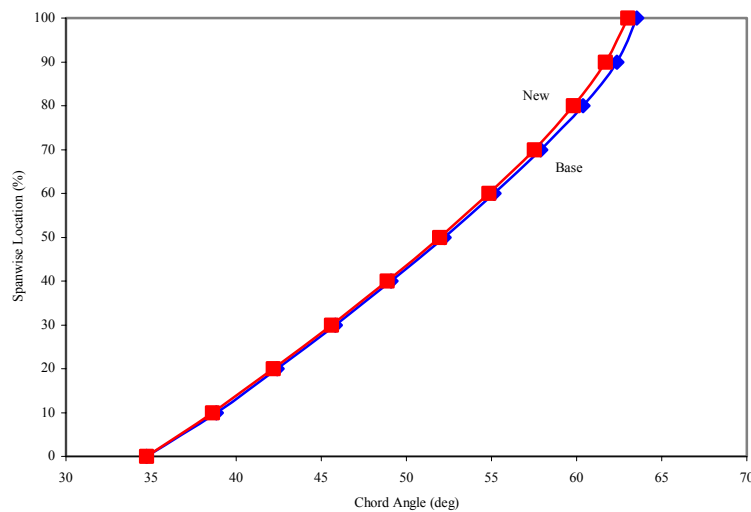


Figure 38. Sanger Rotor – Chord Angle

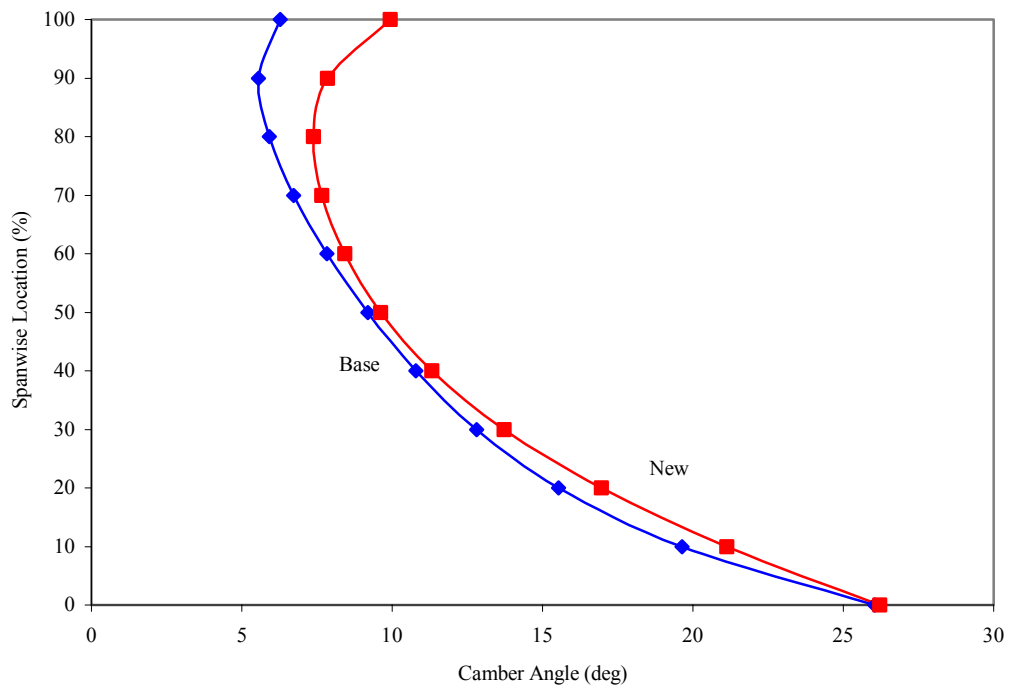


Figure 39. Sanger Rotor – Camber Angle

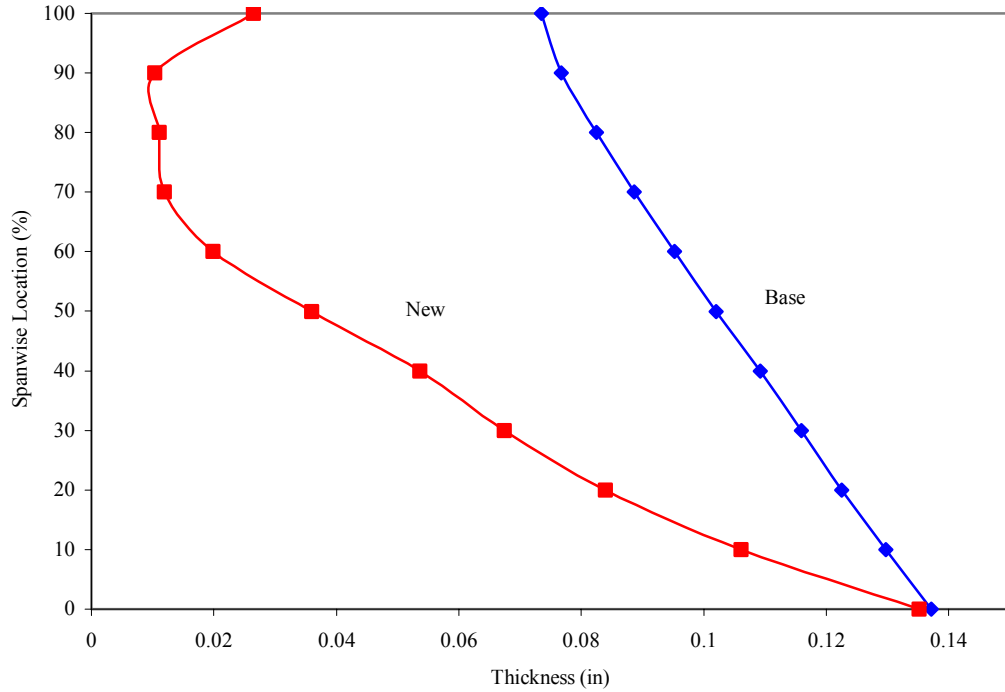


Figure 40. Sanger Rotor – Maximum Thickness Distribution

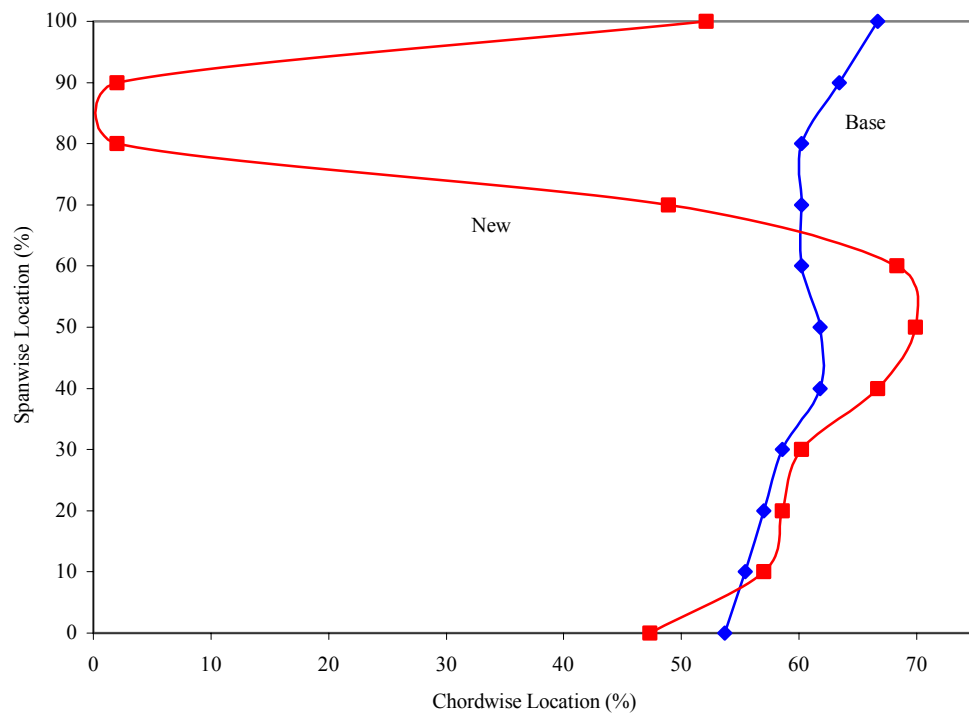


Figure 41. Sanger Rotor – Maximum Thickness Location

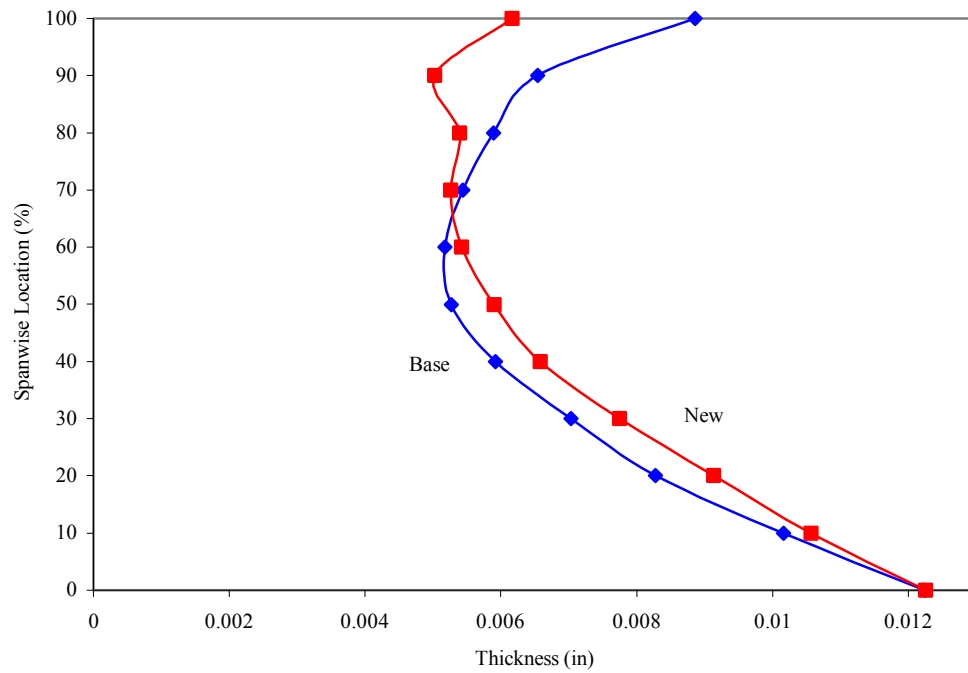


Figure 42. Sanger Rotor – Minimum Thickness Distribution

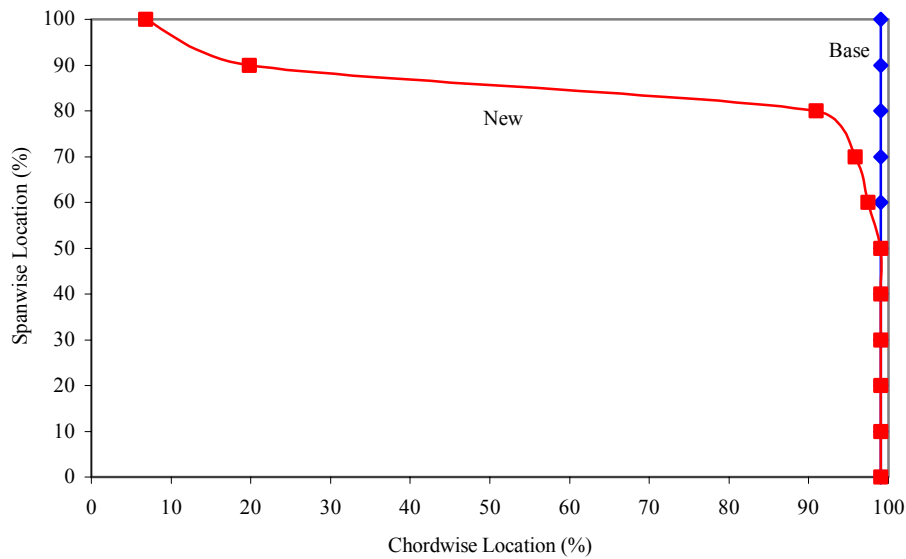


Figure 43. Sanger Rotor – Minimum Thickness Location

The chord angle of the rotor remained essentially unchanged during the optimization except for a slight decrease near the tip. This is most likely due to the fact that the tip leading edge deflects the most under load and the optimized blade is actually a load-deflected shape determined through the cold shape correction process. The camber angle curves are similar although the new blade shows more camber near the tip. This is reflected in the profile illustrations, and is due to the pressure side of the blade moving toward the suction side as previously mentioned. The tip region of the new blade conforms more closely to the suction side of the baseline blade and therefore is more highly cambered.

The thickness plots display the region between where the leading and trailing edge surfaces join the remainder of the blade. The maximum thickness distribution plot demonstrates the dramatic reduction in thickness produced by the optimization procedure. It clearly shows the region in the outer third of blade where thickness was manipulated directly to prevent it from becoming negative. The slight increase in thickness at the tip of the new blade is a function of tip control point movement having been eliminated from the optimization procedure at some point prior to completion of the process. The location of maximum thickness in the new blade behaves similarly with

span to that of the baseline until the very thin outer region. Maximum thickness in the thinnest portion of the blade occurs right where the leading edge surfaces join the remainder of the blade. Since the shapes of these leading edge surfaces were not changed during the optimization, the region just aft of the leading edge actually gets thinner with chord and this creates a concave area in the forward portion of the blade. Again, this may seem impractical from a structural perspective and certainly lies outside the accepted paradigm for the shape of turbomachinery blading, but the effects of this shape on the flow field are positive and interesting to consider. These effects will be presented in the section dealing with the flow field.

Minimum thickness behaves similarly in both the baseline and the new blades. The location of minimum thickness generally occurs where the trailing edge joins the large surfaces of the blade but in the outer region of the new blade, the location of minimum thickness changes. In fact, maximum and minimum thickness in this region appear to occur concurrently and this is just another indicator as to the extreme thinness of the optimized blade.

4. The Flow Field

A number of flow field parameters were extracted directly or calculated from RVC3D output data. These parameters were plotted vs. span for both the Sanger baseline and optimized or new blade designs and those plots are provided in Figures 44 through 52.

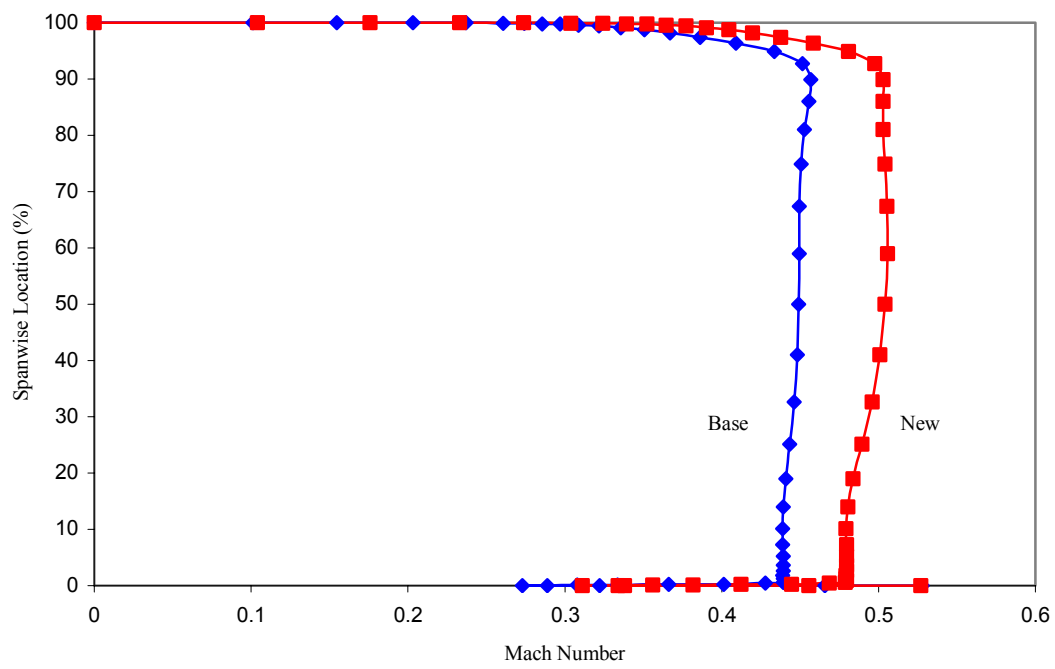


Figure 44. Sanger Rotor – Absolute Inlet Mach Number

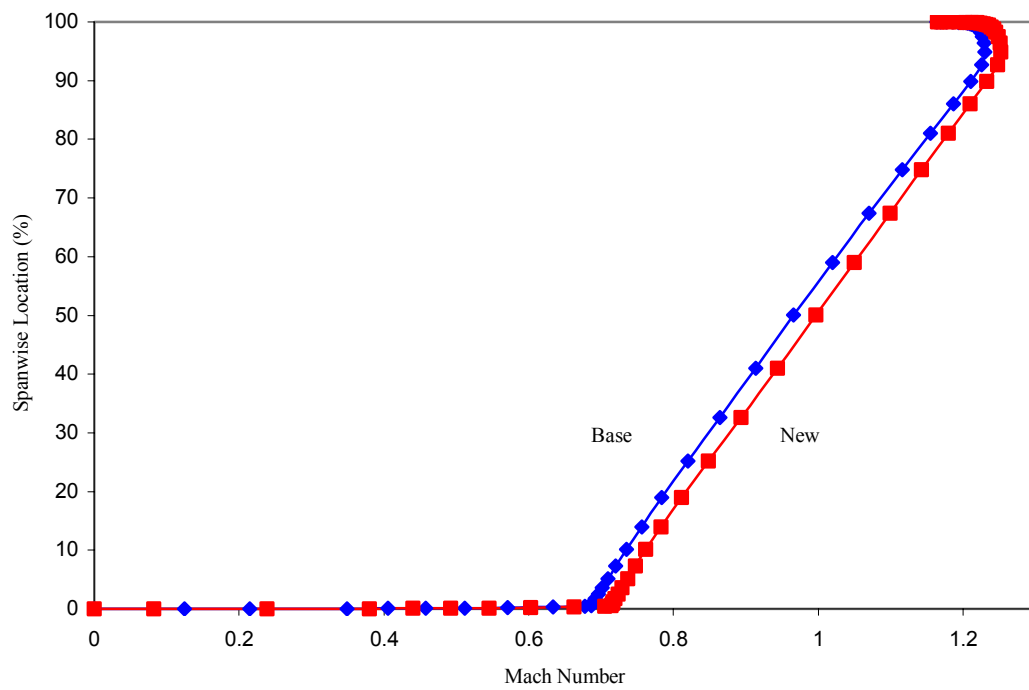


Figure 45. Sanger Rotor – Relative Inlet Mach Number

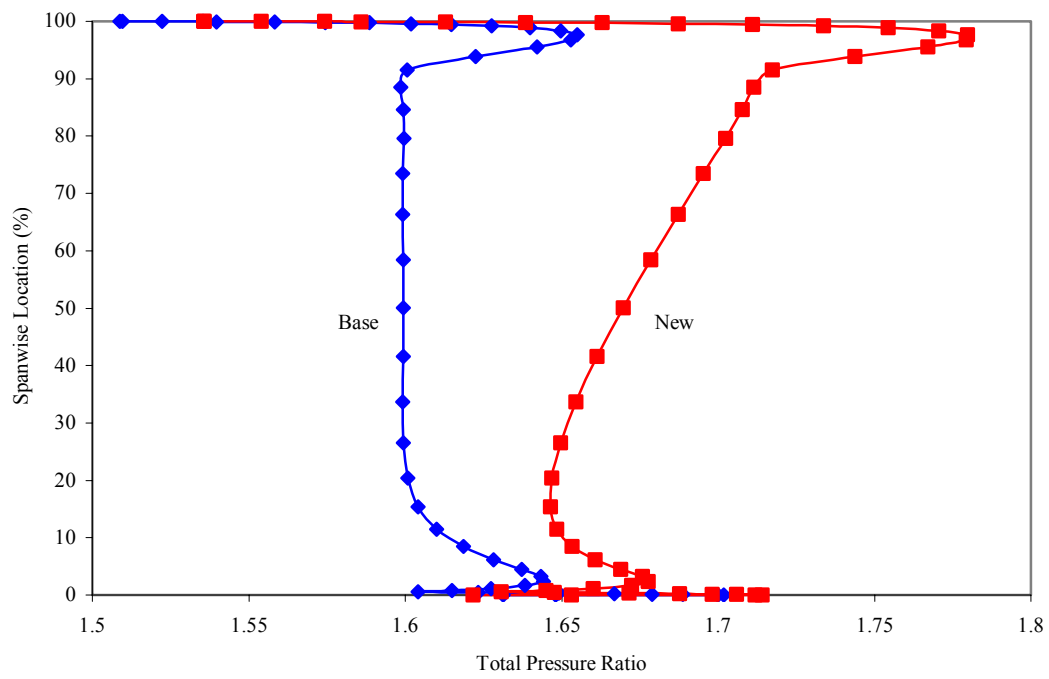


Figure 46. Sanger Rotor – Total Pressure Ratio

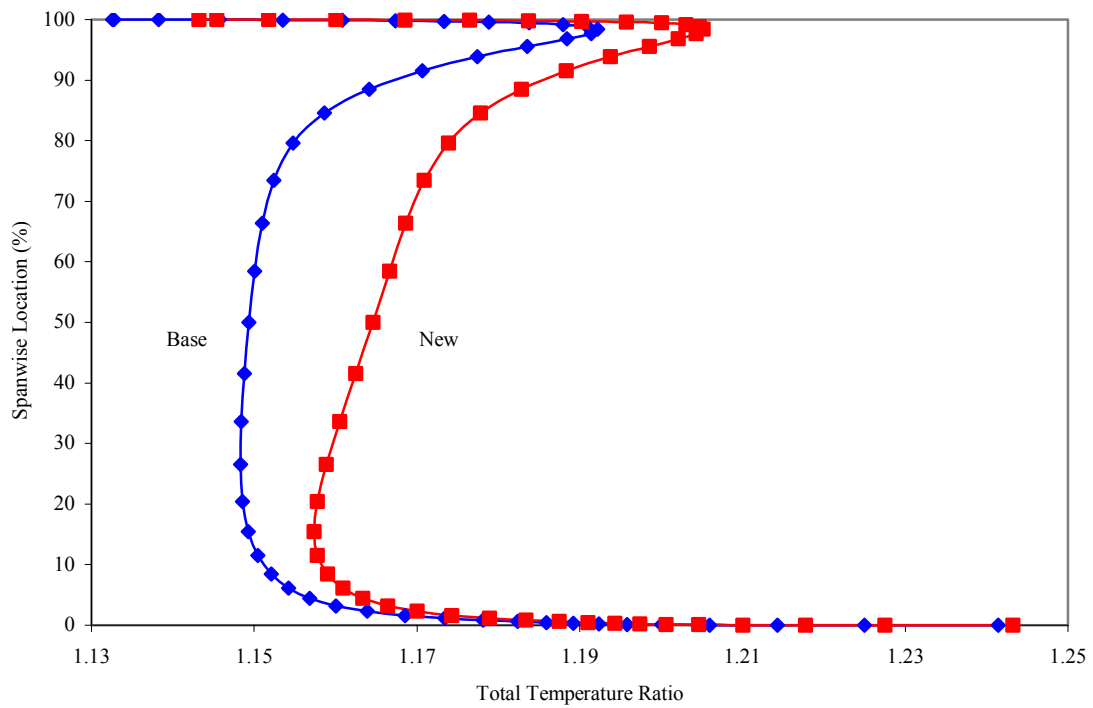


Figure 47. Sanger Rotor – Total Temperature Ratio

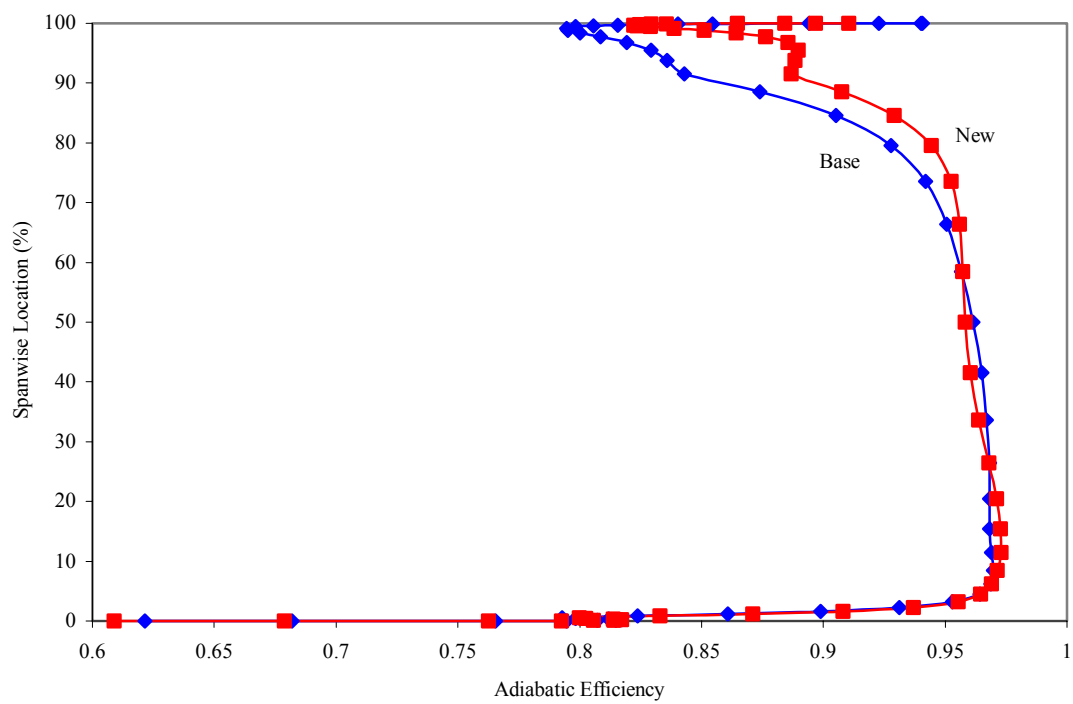


Figure 48. Sanger Rotor – Adiabatic Efficiency

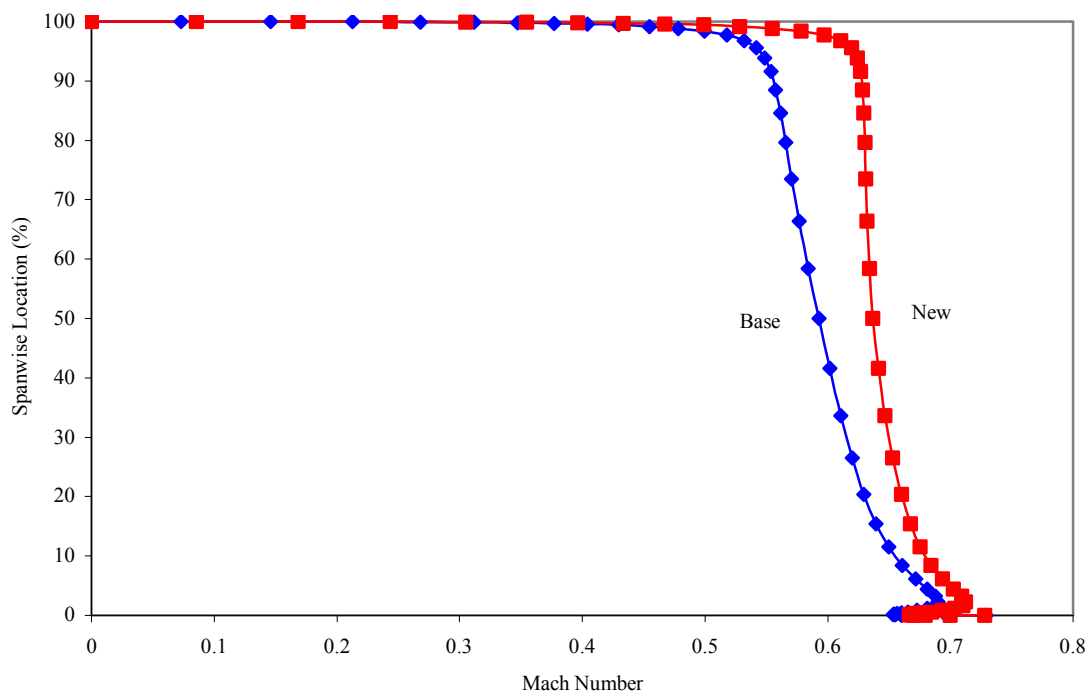


Figure 49. Sanger Rotor – Absolute Exit Mach Number

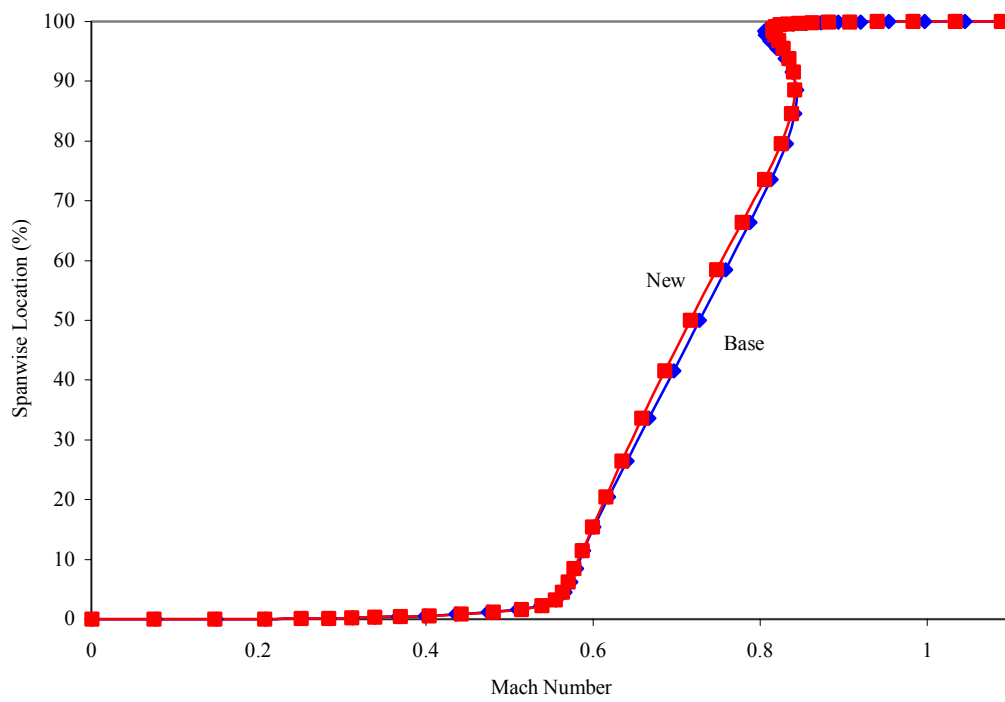


Figure 50. Sanger Rotor – Exit Relative Mach Number

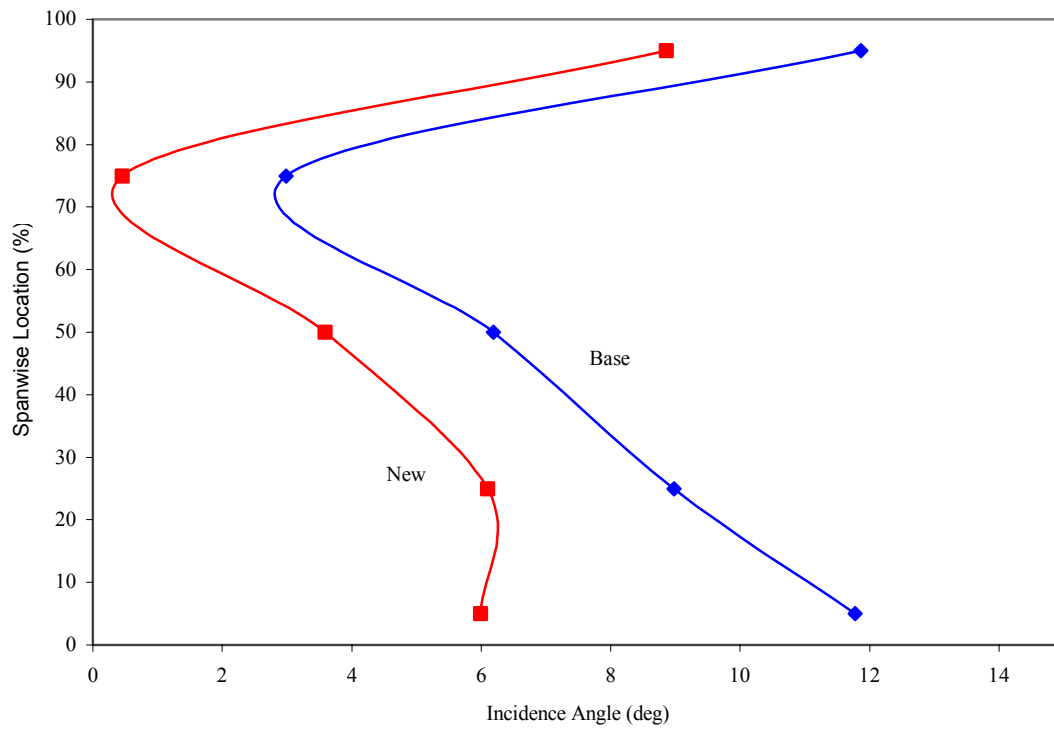


Figure 51. Sanger Rotor – Incidence Angle

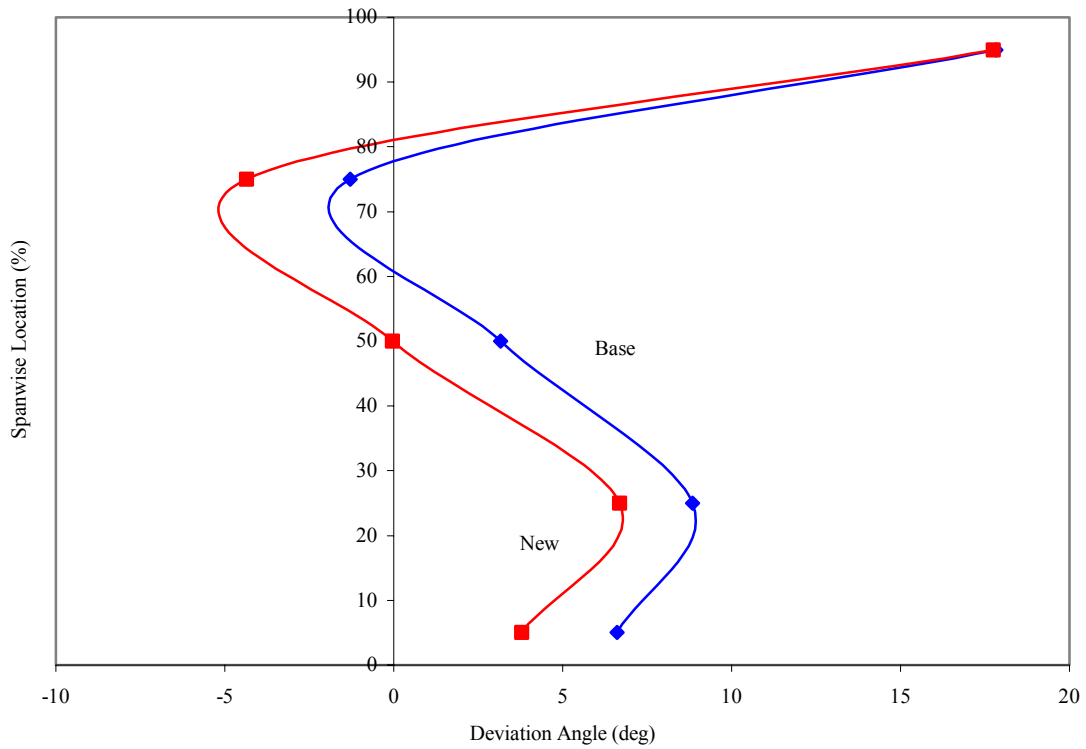


Figure 52. Sanger Rotor – Deviation Angle

It can be seen that inlet Mach number, both absolute and relative, are higher in the optimized blade than in the baseline and that the increases are fairly uniform with span. The Mach number plots for the optimized blade decrease more slowly in the outer case wall region perhaps due to more energized flow near the blade tip as a result of the forward sweep. The increase in mass flow rate realized in the optimization is a result of, and correlates directly with, the increased Mach number at the inlet.

Total pressure ratio is also increased in the optimized blade, and the increase becomes greater moving outward from the hub. The original Sanger design sought to achieve a constant total pressure ratio across the span, and the plot of total pressure ratio vs. span would indicate that such is true for the baseline blade as well. The spanwise increase in the new blade seems to correlate with the presence of forward sweep and is especially pronounced in the outer case wall boundary layer region. An explanation for this phenomenon would be that not only is the flow more energized in this region, there

are also fewer losses due to shock and boundary layer separation effects. These phenomena may be observed in the flow field contours presented later. Total temperature increases in a similar manner but not nearly as dramatically. It indicates that more work is being performed on the flow by the optimized blade, which would be expected for a rotor with increased pumping capacity.

The total pressure and total temperature ratios described above combine to account for the increased adiabatic efficiency observed in the new blade design. As mentioned, both quantities are increased over those seen for the baseline and that increase becomes greater with span. The total pressure ratio increase is far greater near the tip and explains why almost all the increase shown on the efficiency plot occurs in that region.

Absolute Mach number is increased at the exit as was expected for the higher mass flow rate achieved in the optimization process. Exit relative Mach number is nearly unchanged, and is in fact lower in the middle of the blade than for the baseline. This correlates well with the finding that deviation angle is lower over the majority of the span, as illustrated in the deviation angle plot. Lower deviation angles translate to lower tangential velocity components which, depending upon local sonic velocity at the exit, could lead to lower relative Mach numbers.

The plot of incidence angle vs. span shows that it too is decreased in the new blade. This decreased incidence angle indicates that the blade design is better suited to the conditions of the flow, and leads to fewer losses, as will be seen in the following contour images of the flow field. Figure 53 is a depiction of Mach number contours just above the suction surface of the baseline blade on the left, and of the optimized blade on the right. It provides an overall comparison of the flow fields around each blade as well as a good perspective view of the blades themselves. The differences in shape between the two - most specifically, the differences created by the introduction of the forward sweep, show clearly. The contour lines shown are for the K surface five grid lines away from the surface of the blade; that is, just outside the boundary layer.

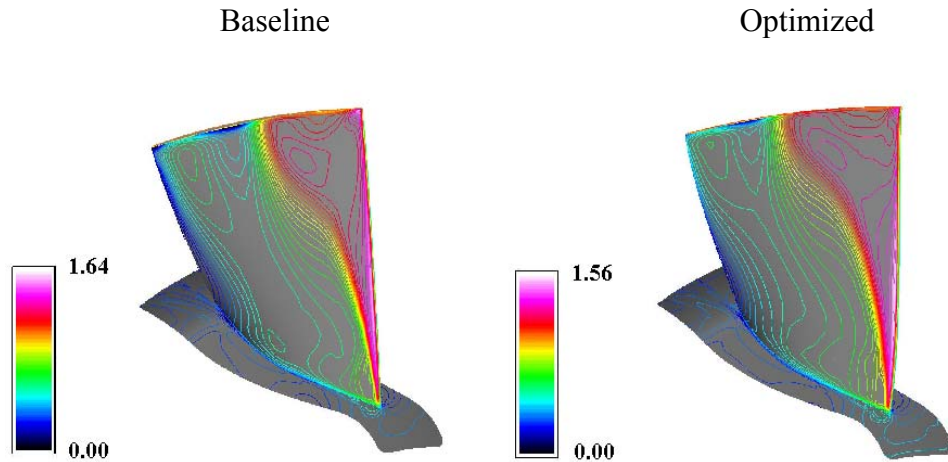


Figure 53. Sanger Rotor – Geometry and Mach Number Distribution

The contour lines are very similar at first glance, but there are subtle differences which help to explain the improved performance of the optimized blade. First, the peak Mach number for the optimized blade is lower than that for the baseline. Since the contour colors are almost identical between the two images, a lower peak Mach number would indicate the overall flow is slightly slower over the new blade, thereby creating weaker shocks and fewer shock losses in the supersonic region. Close examination of the shock area near the tip of the new blade shows that the contour lines around the shock are in fact spread over a larger distance, thus supporting the notion of a weaker shock structure. Also of note is the trailing edge region. The dark blue colors indicate areas of very low Mach number associated with flow separation in the boundary layer. These areas are considerably larger and more pronounced on the baseline blade. They extend over the entire span whereas there are places on the trailing edge of the new blade where they are not visible at all. There is also a region of such flow along the tip. Again, this area is larger for the baseline blade than for the new blade. Weaker shocks and fewer friction losses in the tip region are the primary reasons for the higher total pressure ratio and improved efficiency achieved in the optimization.

Figures 54 through 58 are blade-to-blade views of the flow contours at various spanwise locations for both blades with the baseline blade on the left.

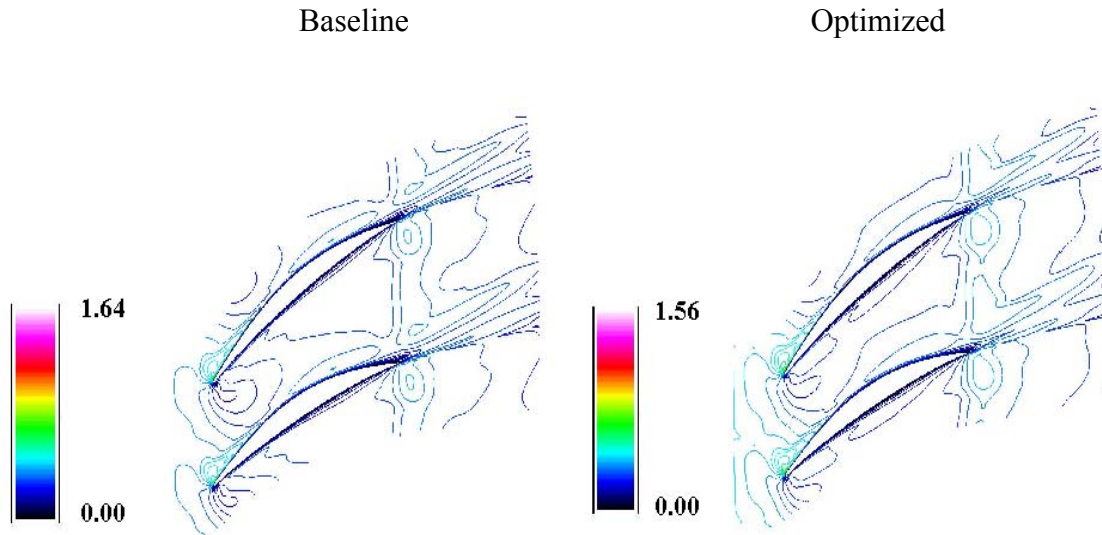


Figure 54. Sanger Rotor – Mach Contours near the Hub

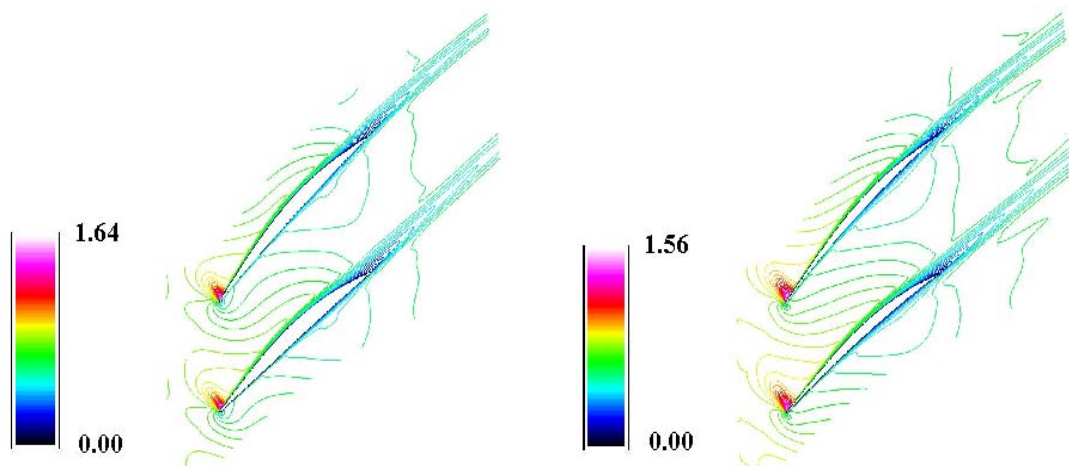


Figure 55. Sanger Rotor – Mach Contours at 30% Span

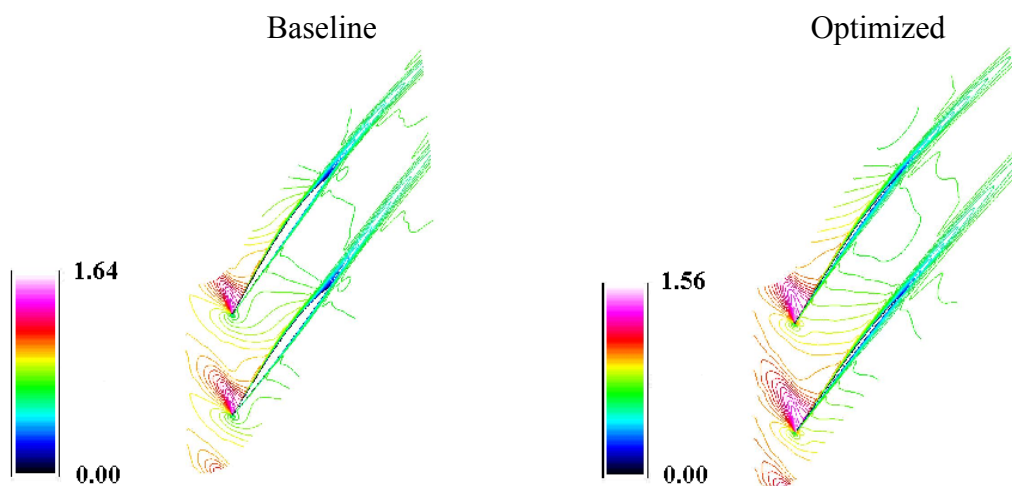


Figure 56. Sanger Rotor – Mach Contours at Midspan

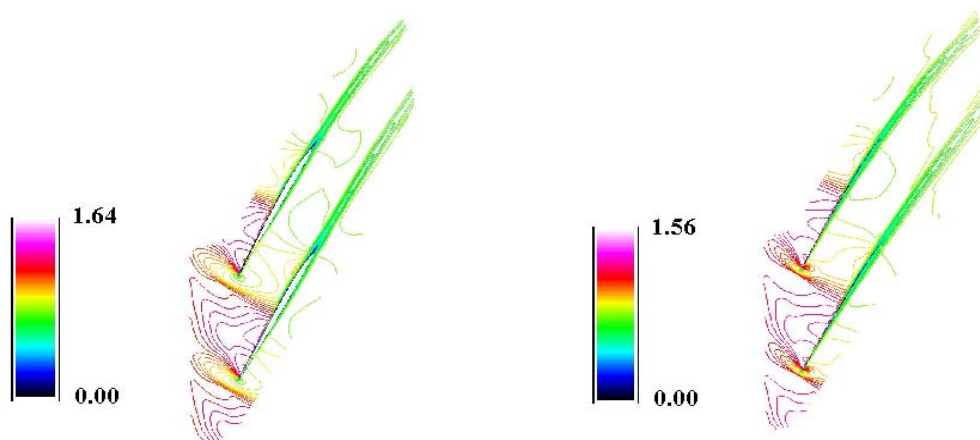


Figure 57. Sanger Rotor – Mach Contours at 70% Span

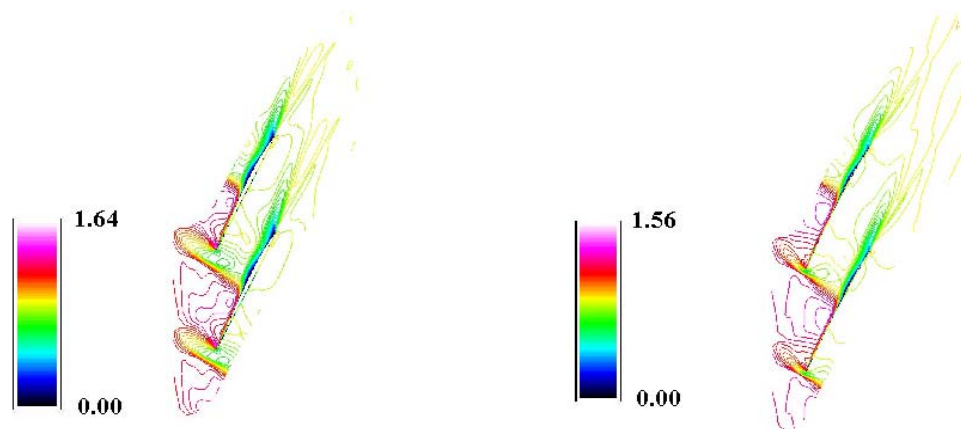


Figure 58. Sanger Rotor – Mach Contours near the Tip

Comparison of these contour images again reveals the extreme relative thinness of the optimized blade. These pictures support the ideas put forward in the previous discussion concerning weaker shocks and less flow separation near the trailing edge. In those showing the flow at 70% span and near the tip, it can be seen that the leading edge shock stands considerably closer to the optimized blade than to the baseline, an indication that it is a weaker shock. Also, in the area where the bow shock hits the preceding blade, the contour lines are farther apart on the optimized blade; the shock area is smeared out and this too demonstrates that it is weaker. The dark blue areas on the trailing edge suction surfaces where flow separation occurs are easily seen to be larger for the baseline blade except near the hub where the geometries are nearly identical.

In general, the images of the flow field along with the graphical data previously presented aptly demonstrate properties and details of the flow which account for the performance improvements observed for the optimized design.

5. Structural Comparison

Finite element structural analyses were performed on the both the baseline and optimized blades in accordance with the procedures outlined in Section IV. Figures 59 and 60 present the results of that analysis.

Maximum Steady Stress – 31,100 psi
Maximum Deflection - .0308 in.

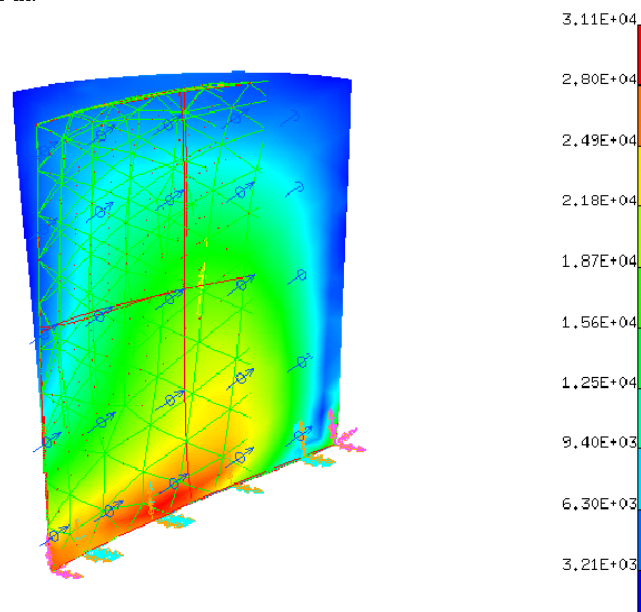


Figure 59. Sanger Rotor – Structural Analysis, Baseline Blade

Maximum Steady Stress – 22,500 psi
Maximum Deflection - .13 in.

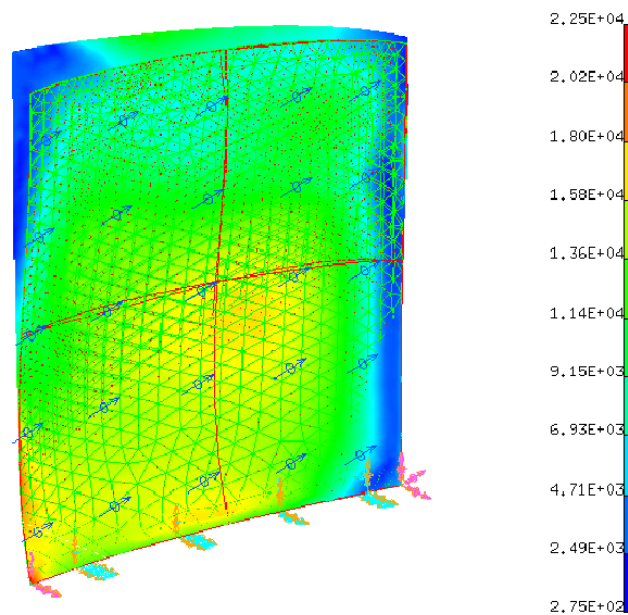


Figure 60. Structural Analysis, Optimized Blade

The finite element analysis for the optimized blade shows that stress levels are much lower and more evenly distributed through the blade structure. For the material utilized, a 7075-aluminum alloy, the maximum allowable stress was 55,000 psi and it is seen that both blades fall well below that value. The primary reason for the dramatic decrease in stress for the new blade is the lower centrifugal loads caused by the thinning of the blade and the resulting decreased weight. Gas loads for the optimized blade were slightly higher than for the baseline due to the increased mass flow rate. The difference was approximately 2 pounds - 13 pounds total vs. 11 - but the effect was small since the gas loads are an order of magnitude lower than the centrifugal loads. Generally, forward sweep causes the stresses at the leading edge of the hub to increase substantially, and it can be seen that the highest stress in the new blade does occur in that region; but the effect is offset by the overall effect of the lower centrifugal loads.

As would be expected with a much thinner blade, the maximum deflection for the optimized blade is on the order of four times that of the baseline. It occurs in the region of the leading edge at the tip. It was this large deflection that first made it apparent that a cold shape correction procedure would be required for the results of the aerodynamic optimization to remain valid. The cold shape correction was developed and applied to the blade as described in Section IV.

B. ROTOR 67

1. Overview

NASA Rotor 67 was optimized in accordance with the procedure described in Section IV. An overall comparison of the baseline and final design configurations are presented in Table 6.

	<u>Baseline</u>	<u>Final Design</u>
Mass Flow Rate	73.80 lbm/sec	75.58 lbm/sec
Total Pressure Ratio	1.56	1.6
Adiabatic Efficiency	0.895	0.914
Polytropic Efficiency	0.902	0.92
Design Speed	16,043 RPM	16.043 RPM
Tip Inlet Relative Mach Number	1.37	1.38
Tip Forward Sweep	0%	9%
Weight Factor	1	0.96
Maximum Steady Stress*	115,000 psi	132,000 psi

- 110% design speed

Table 6. Rotor 67 Optimization Summary

From Table 6, it can be seen that the goal of increasing the polytropic efficiency at the design point by at least one percent was easily achieved in that the efficiency of the final design is nearly two percent higher than the baseline. Adiabatic efficiency improved by a similar amount. In addition, mass flow rate and total pressure ratio increased by approximately 2.5%, less than the improvement observed for the Sanger rotor since neither of these were the objective function for this exercise. The amount of sweep at the tip for the Rotor 67 final design is only 9% as compared to that for the Sanger rotor but it should be noted that the sweep at one third span is much higher, about 19% as compared to 10%. This shape difference results again from the different objective function. The Rotor 67 geometry changes will be discussed in detail later.

There is much less of a weight change for the Rotor 67 effort and that results directly from the fact that blade thickness was not allowed to vary as dramatically and the blade retained something close to the baseline thickness. The maximum stress increased in the final design due to the effect of forward sweep on the hub leading edge. This will be shown in the section on structural analysis.

The results help illustrate several positive aspects of the geometry package as well as the optimization process which it facilitates. First, the fact that BLADE-3D produced a good fit to Rotor 67 proves that it has application across a range of blade designs. Rotor 67 is a much larger blade with a higher aspect ratio and considerably more camber in the hub region. It can be inferred that BLADE-3D would have little or no trouble fitting a generic preliminary design as part of an automated design procedure.

Secondly, targeted performance improvements were achieved through the optimization process and the relative increases in the various performance parameters were quite different than those observed for the Sanger rotor. This shows that the concept of changing the position of Bezier control points to achieve improvements in 3-D blade performance parameters is valid and viable.

2. Performance

Constant speedlines which illustrate the performance improvements obtained for Rotor 67, are shown in Figures 61 and 62.

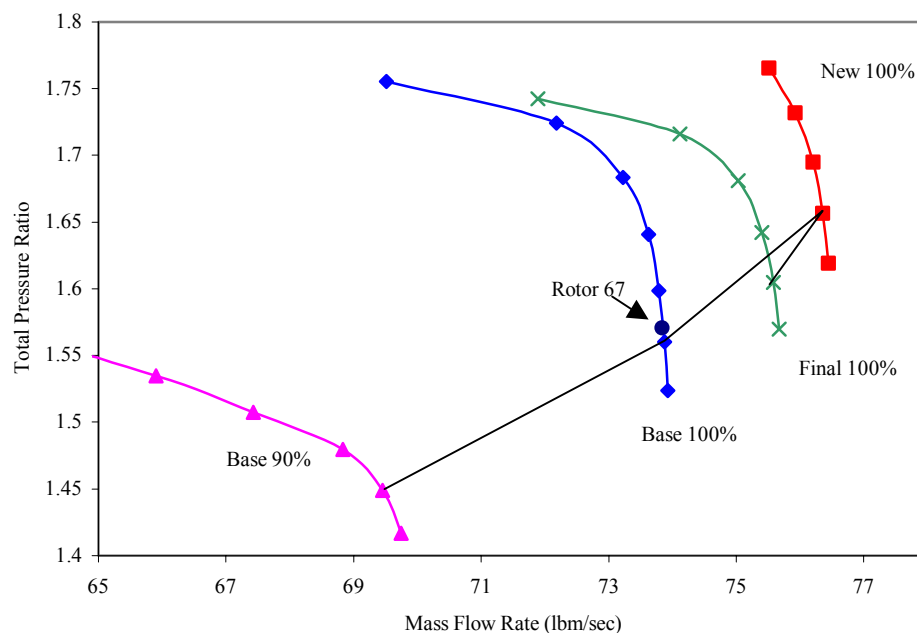


Figure 61. Rotor 67 Performance

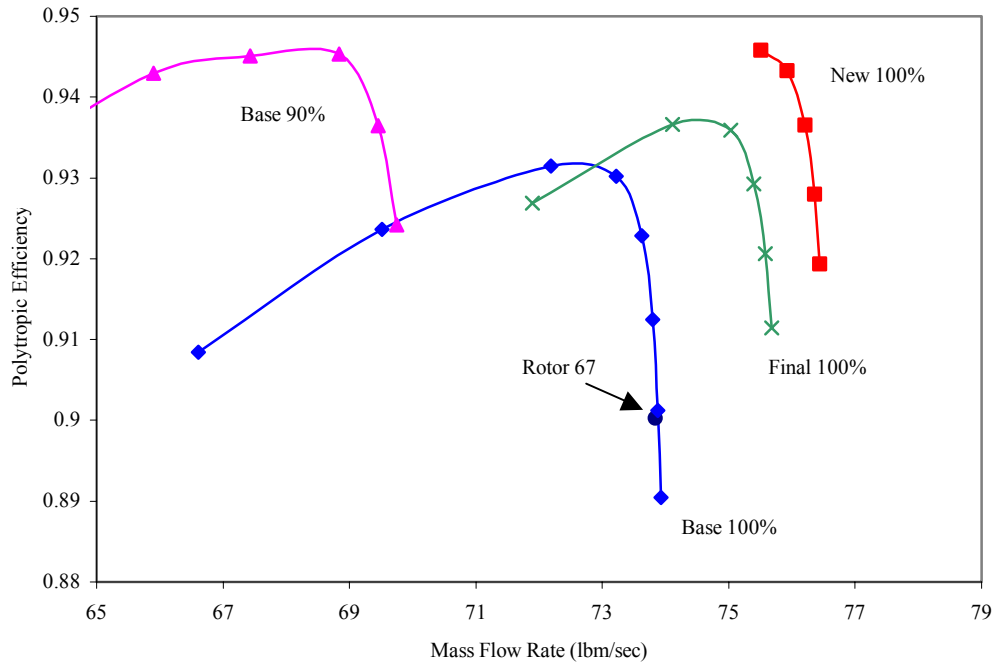


Figure 62. Rotor 67 Efficiency

From the plots, it is easy to see the major difference between the optimization process for Rotor 67 and that for the Sanger rotor. For the Sanger rotor, the structural analysis actually produced a better performing blade than that achieved during the basic procedure. Here, it was required to back off the design resulting from the aerodynamic optimization in order to meet structural constraints. That is shown on Figure 71 as a sort of backtrack of the design point line from the “new” to the “final” design.

Once again, the point at which the original geometry was fitted by BLADE-3D is shown and again, it can be seen that it lies on or very close to the lines for the baseline 100% performance on both plots. Like the Sanger rotor effort, it was decided to choose a point on the speedline away from stall in order to facilitate convergence of the flow code. In this case, it appears that the point chosen was perhaps a little too far away in that it lies a considerable distance from the peak of the efficiency curve shown in Figure 62. Since efficiency was the objective function, it would have made sense to conduct the optimization near peak efficiency, although efficiency improvements for the final design

were realized over the entire range of values plotted, and in particular at the chosen design point. This, however, qualifies as a lesson learned for future investigations.

The impact of the performance improvements seen here would be similar to those discussed for the Sanger rotor – smaller size, less complexity, better fuel efficiency, etc.

3. Geometry

The geometry changes for Rotor 67 resulting from the optimization process are presented in Figures 63 through 66. Geometries for the baseline, the blade achieved through the aerodynamic design process (new), and the final design are all shown for comparison.

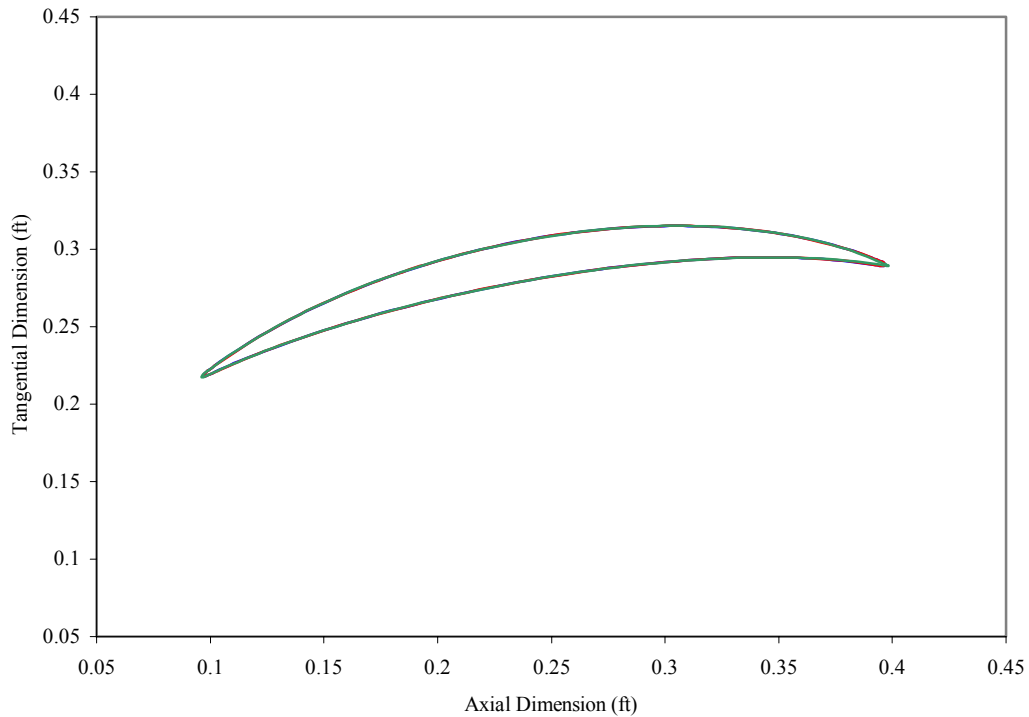


Figure 63. Rotor 67 Geometry – Hub

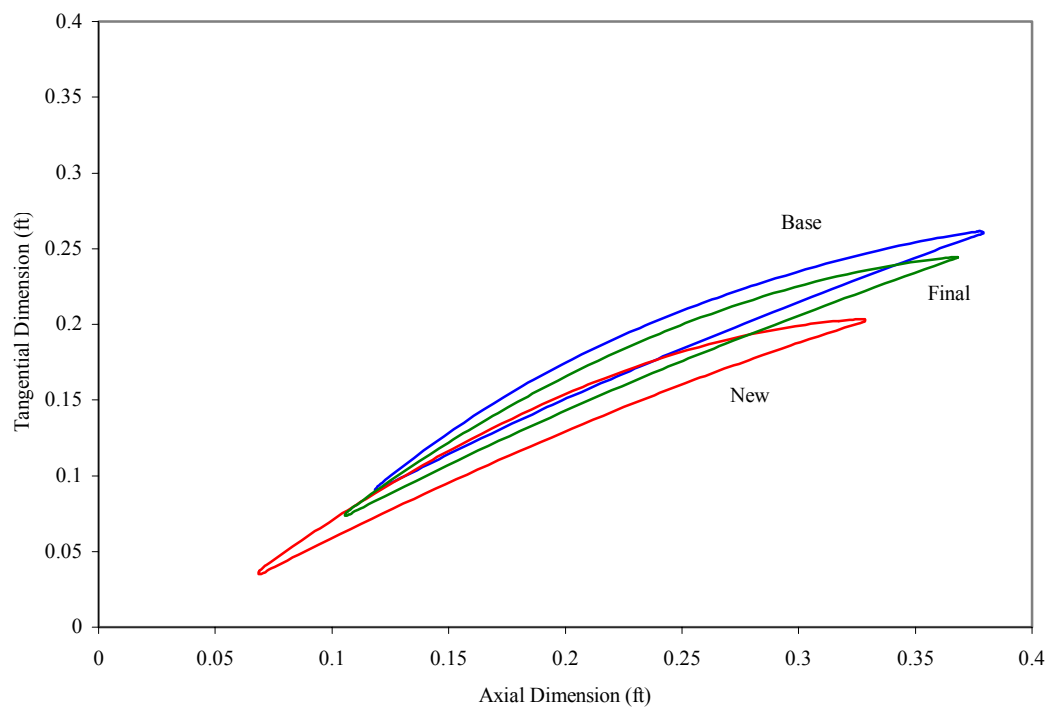


Figure 64. Rotor 67 Geometry – 30% Span

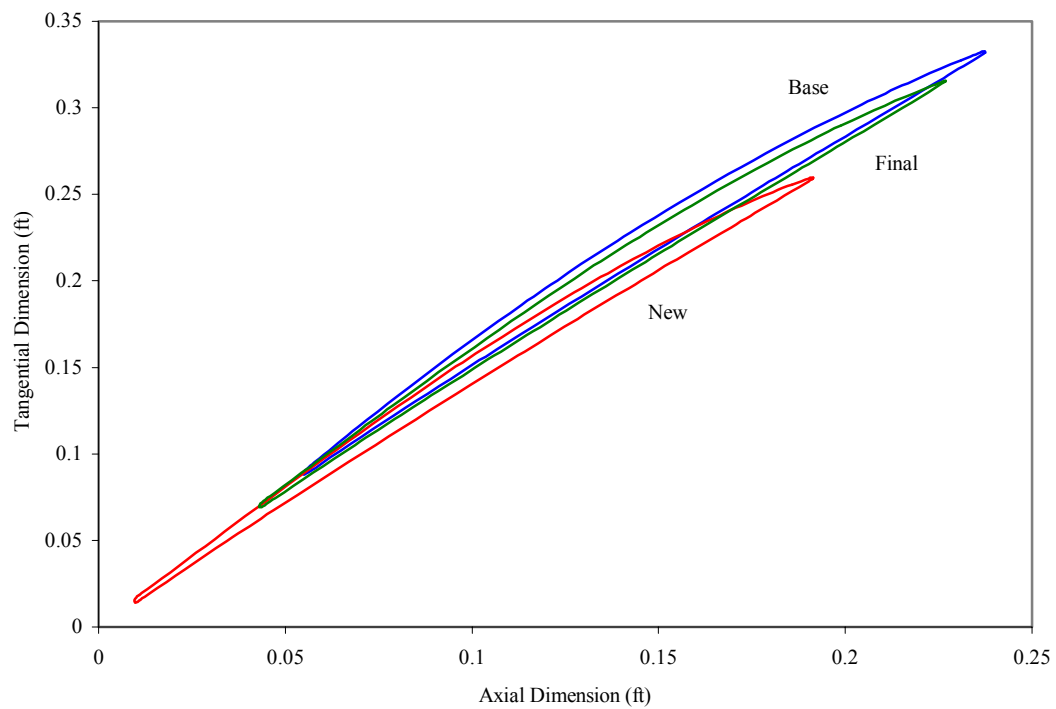


Figure 65. Rotor 67 Geometry – 70% Span

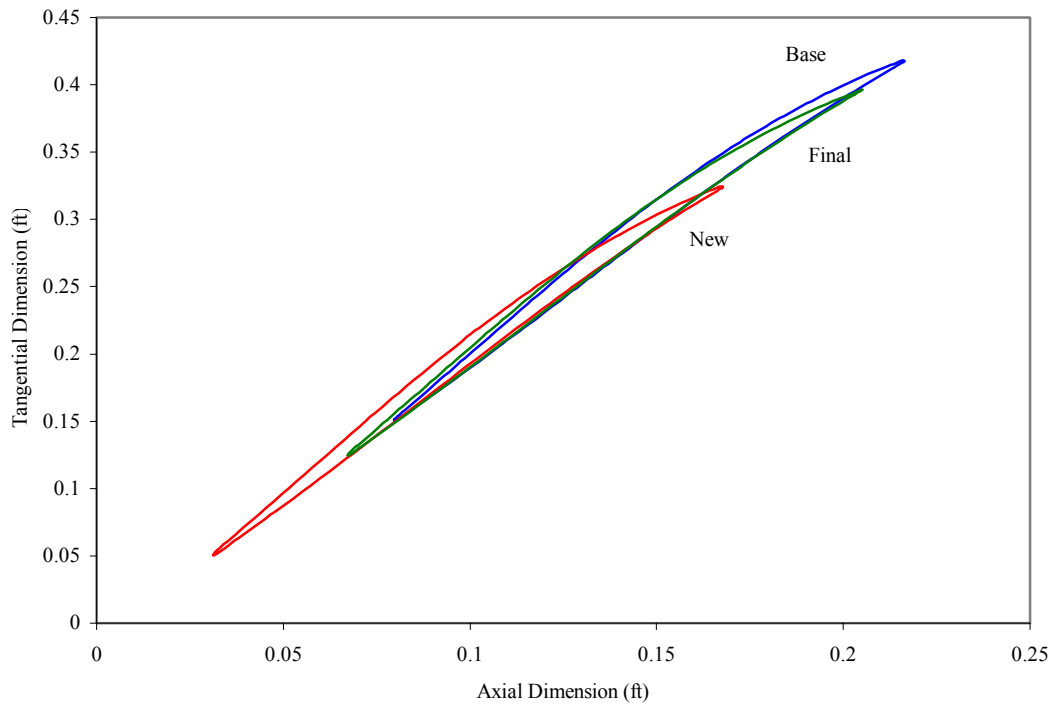


Figure 66. Rotor 67 Geometry – Tip

There are several aspects of the geometry changes that should be noted. The most obvious one as compared to the results for the Sanger rotor is that the thickness for all three geometries are very similar, thus showing that the design goal of avoiding thickness loss was achieved. Secondly, the phenomenon observed for the Sanger rotor where sweep for the innermost row of control points (not the hub) resulted in tangential translation as well as pure sweep, is repeated here but to an even higher degree particularly in the new blade. This is because the amount of sweep applied to the inner row was about twice as high as was explained in the overview. Finally, it can be seen that forward sweep evident in the final blade is much less than that for the new blade and shows the result of removing sweep for structural considerations.

Figures 67 through 71 are the accompanying plots of various geometric parameters.

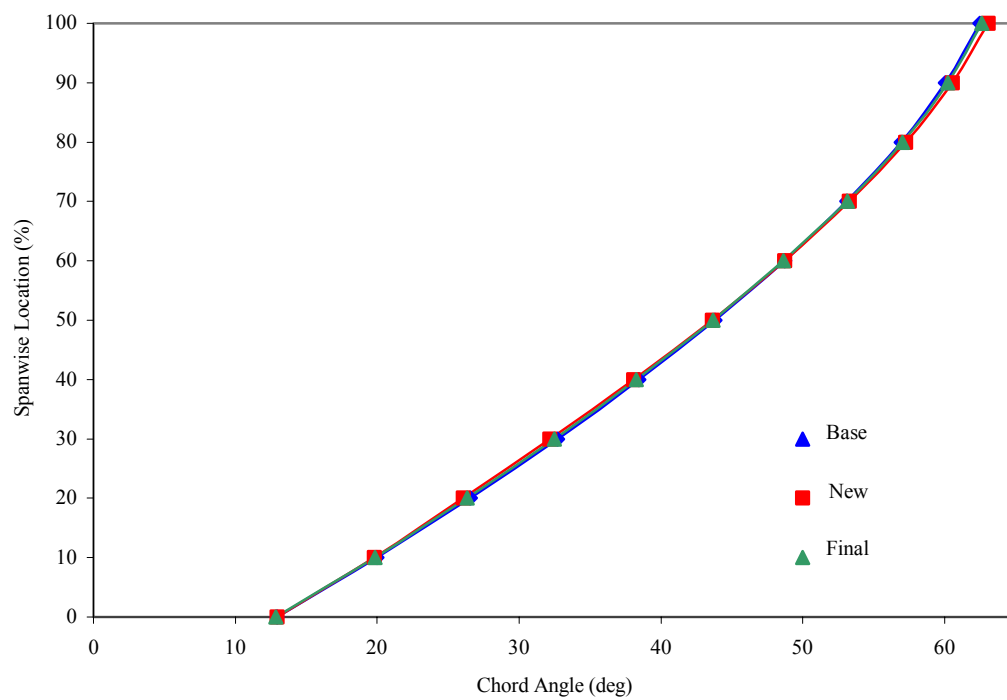


Figure 67. Rotor 67 – Chord Angle

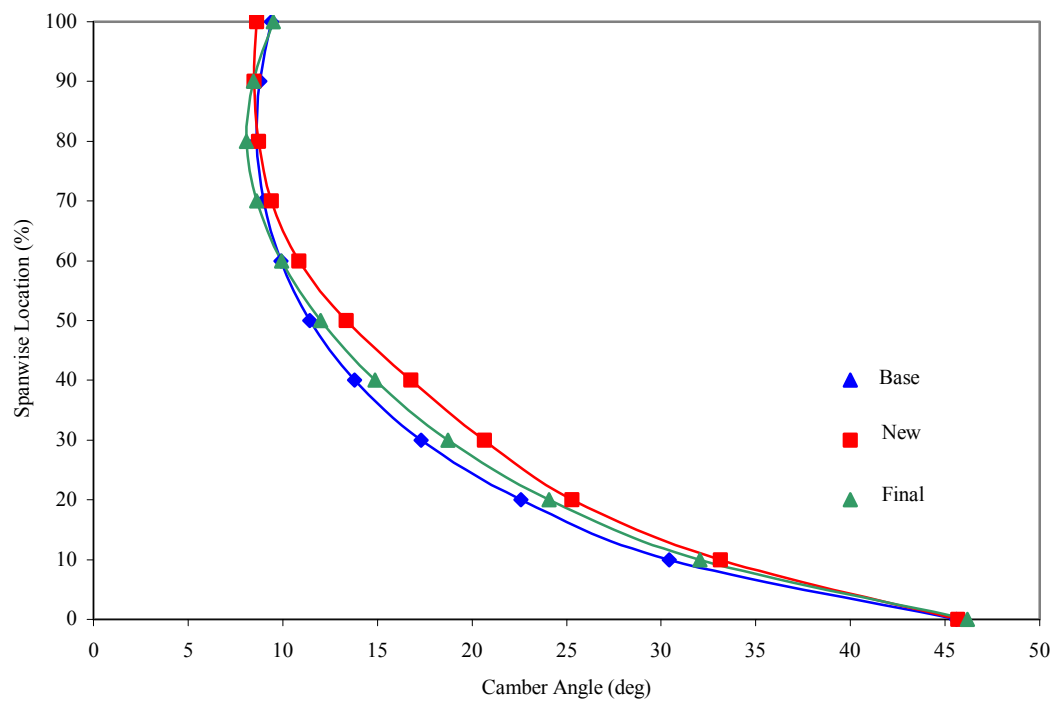


Figure 68. Rotor 67 – Camber Angle

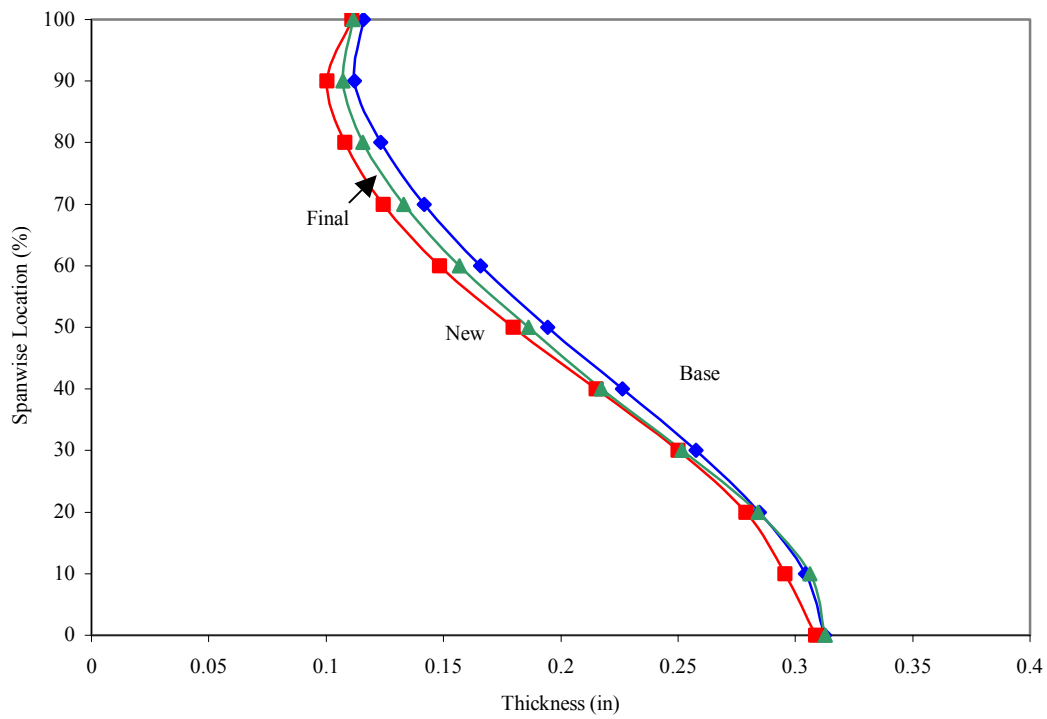


Figure 69. Rotor 67 – Maximum Thickness Distribution

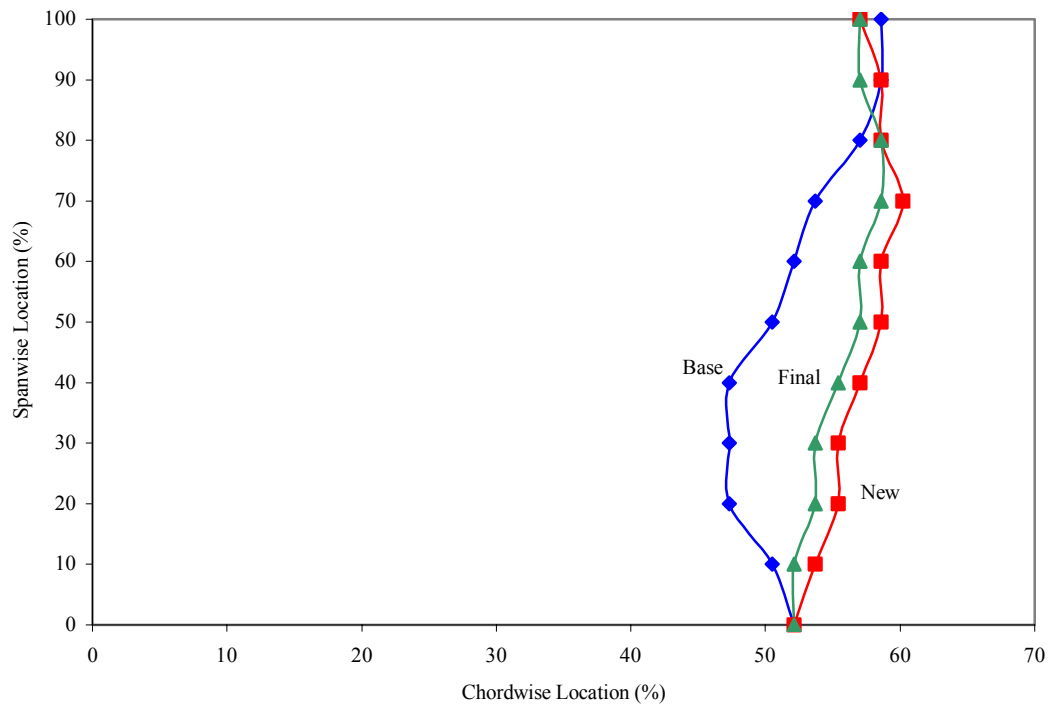


Figure 70. Rotor 67 – Maximum Thickness Location

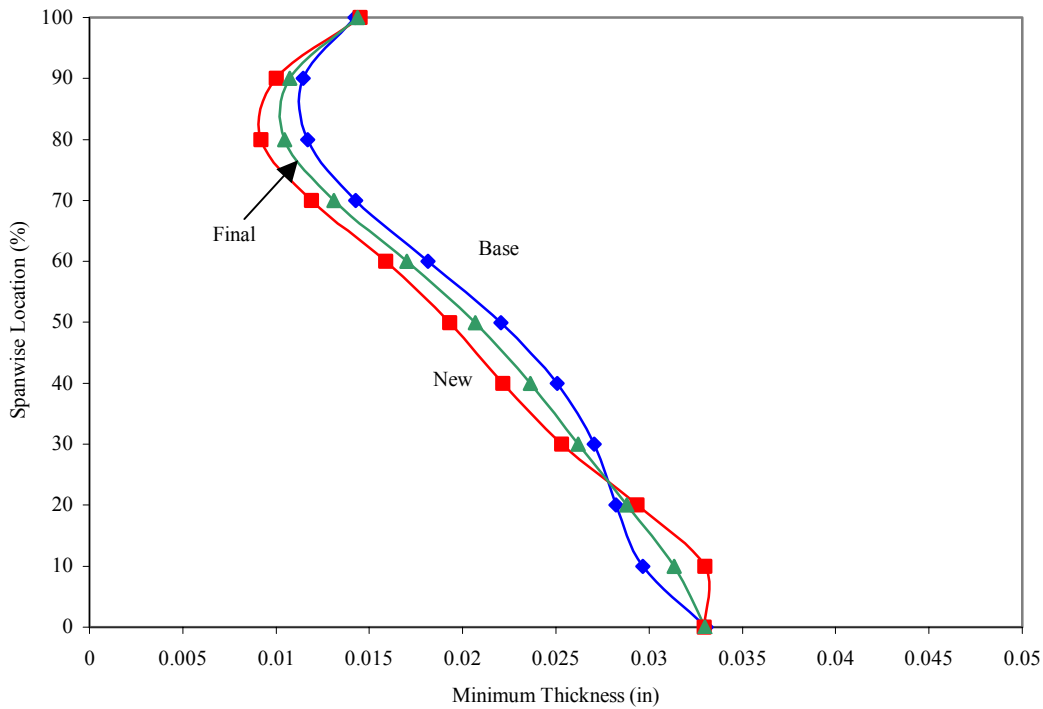


Figure 71. Rotor 67 – Minimum Thickness Distribution

In general, the plots show that none of the geometric parameters shown were changed substantially by the optimization process. Values and trends of each one remain consistent. There are a couple of points that should be made. First, camber angle changes less rapidly in the new blade (and slightly less so in the final blade) as a function of span than it does in the baseline. This creates an interesting result in the nature of the flow field, which will be discussed shortly. Also, the location of maximum thickness is generally farther aft in the new and final blades, a result of the relative movement of the suction side control points to achieve the desired one percent improvement in efficiency. A plot of minimum thickness location is not provided since it was consistent in all three blades at 99% chord.

4. The Flow Field

As for the Sanger rotor, flow field properties for Rotor 67 are presented in Figures 72 through 80. Again, baseline, new and final designs are shown for comparison.

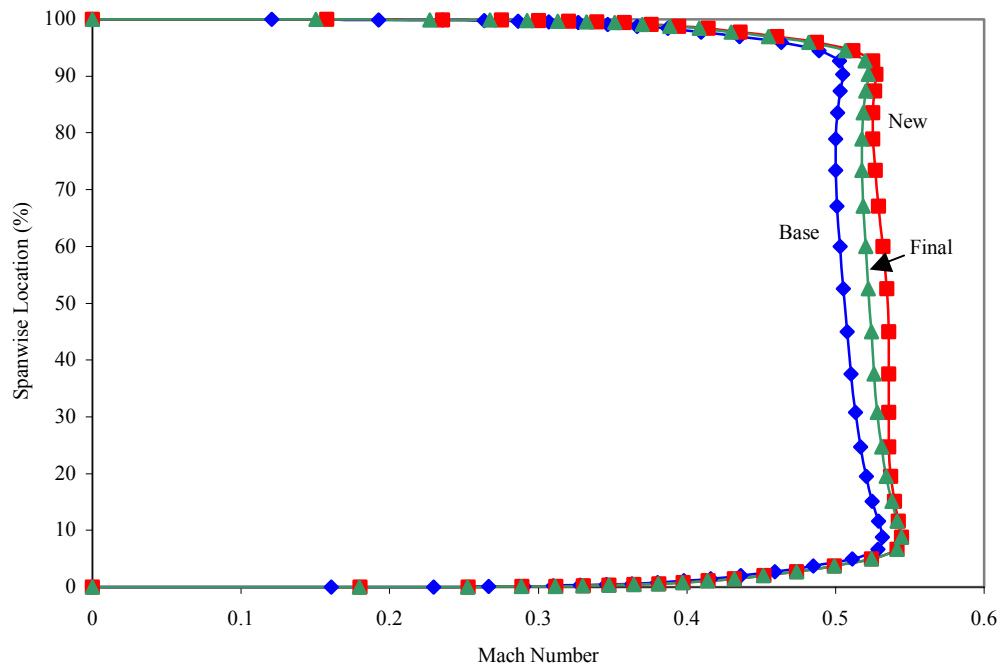


Figure 72. Rotor 67 – Absolute Inlet Mach Number

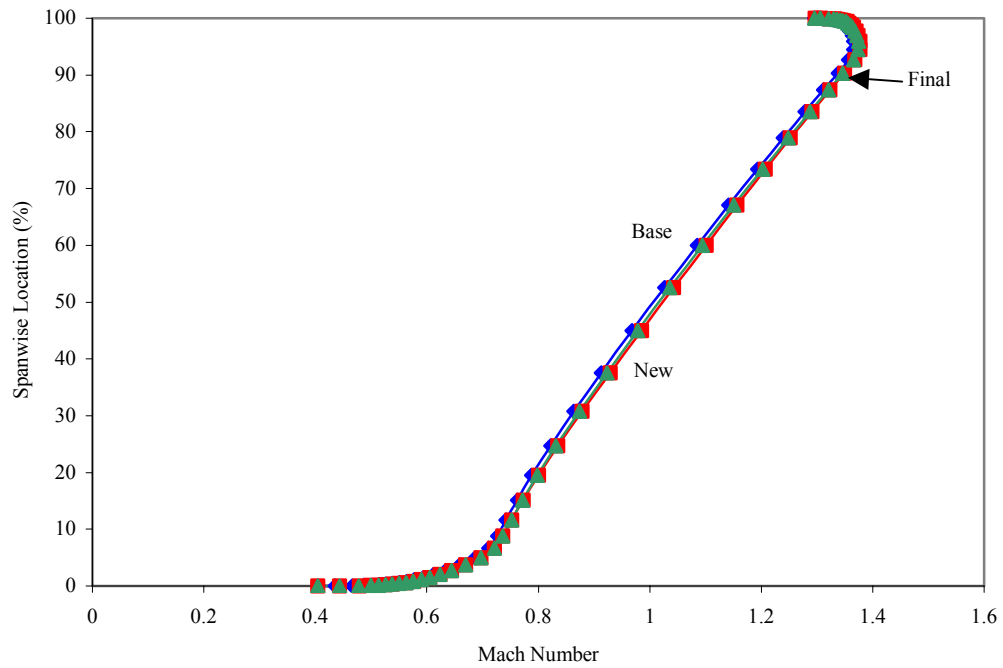


Figure 73. Rotor 67 – Relative Inlet Mach Number

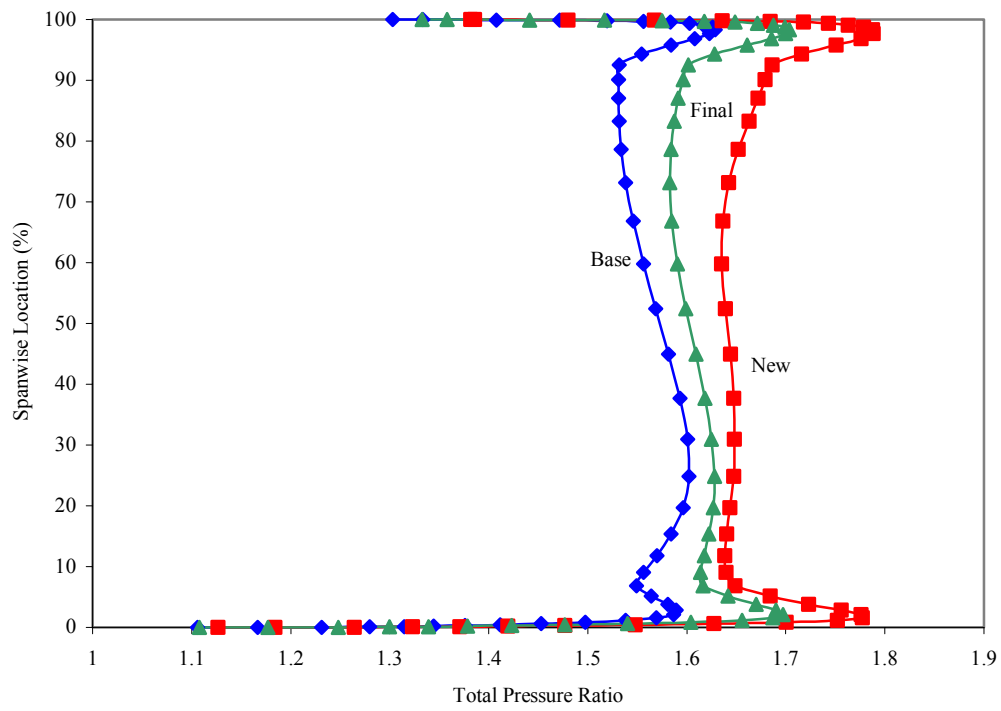


Figure 74. Rotor 67 – Total Pressure Ratio

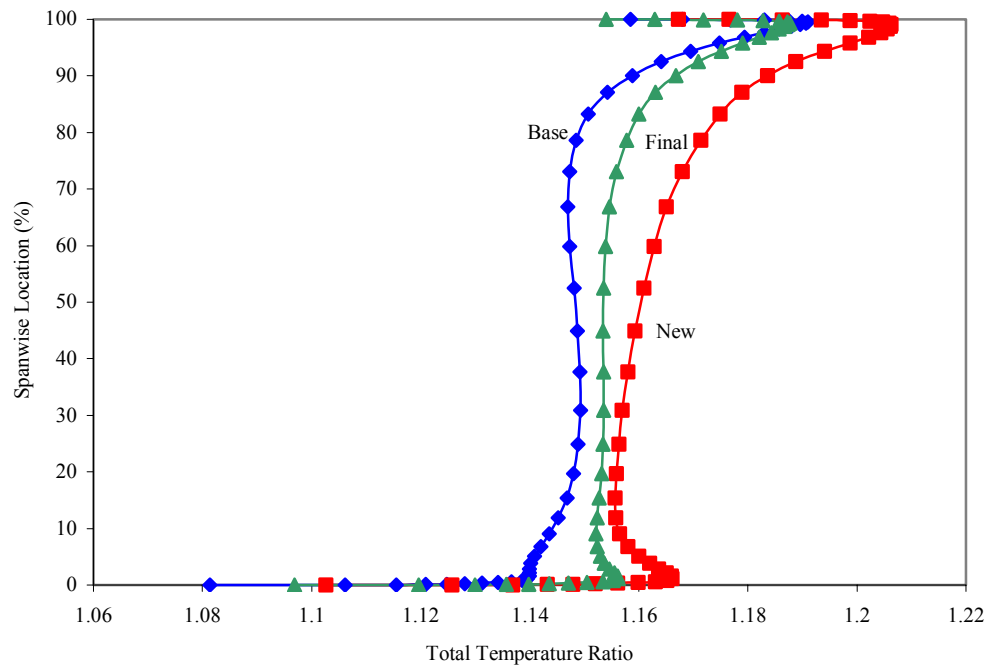


Figure 75. Rotor 67 – Total Temperature Ratio

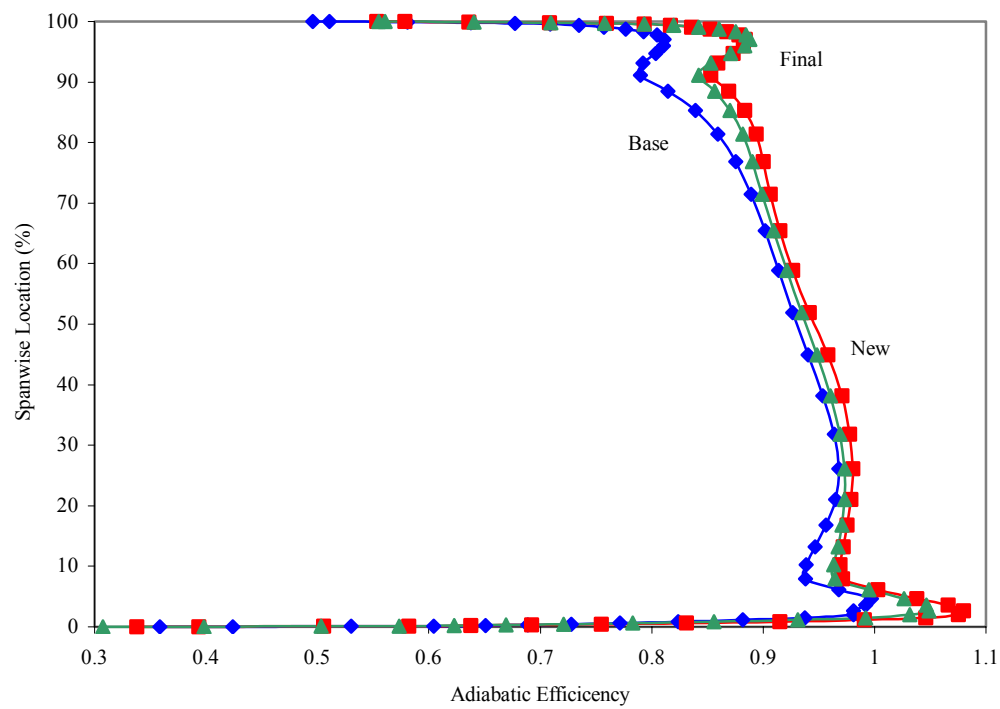


Figure 76. Rotor 67 – Adiabatic Efficiency

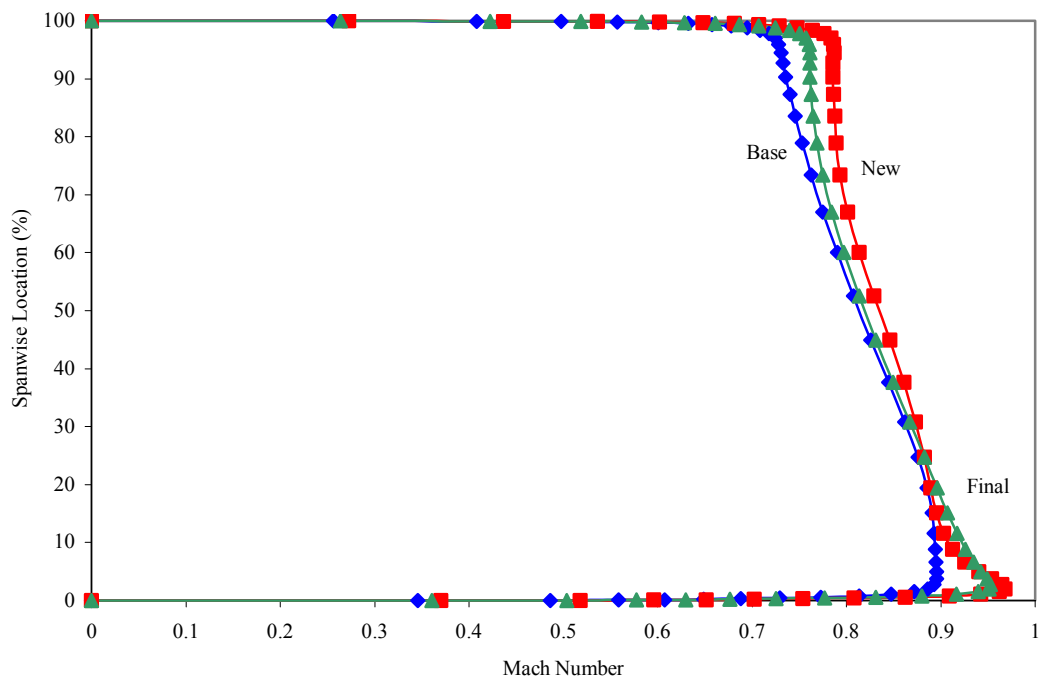


Figure 77. Rotor 67 – Absolute Exit Mach Number

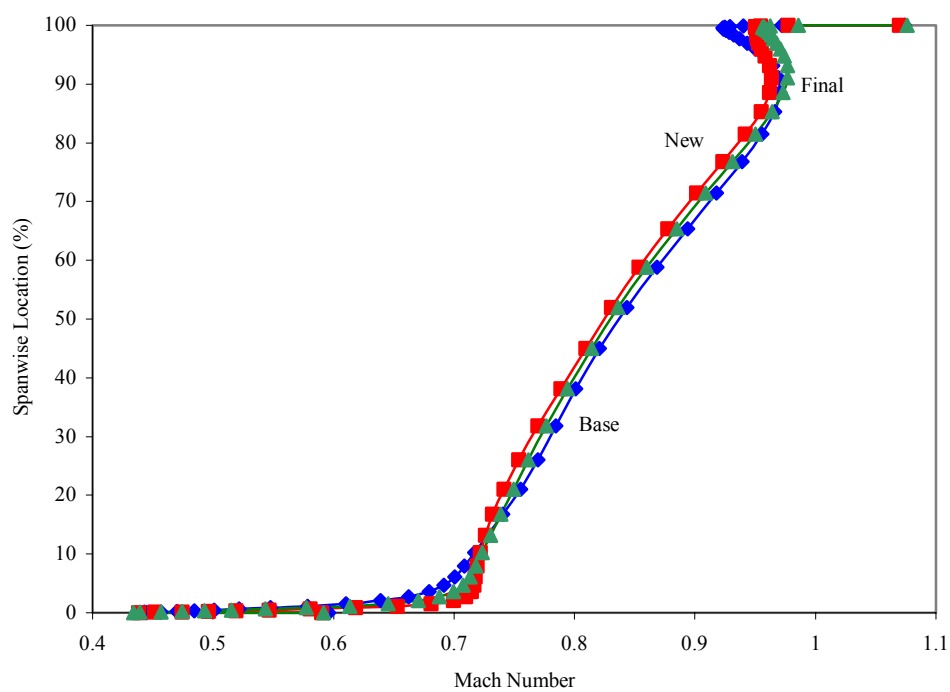


Figure 78. Rotor 67 – Exit Relative Mach Number

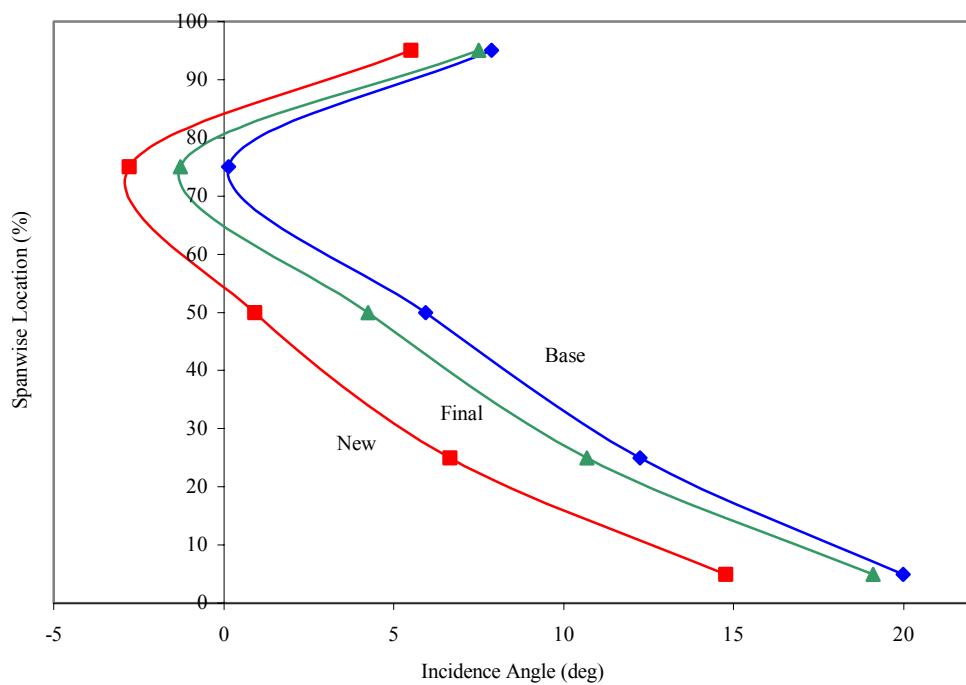


Figure 79. Rotor 67 – Incidence Angle

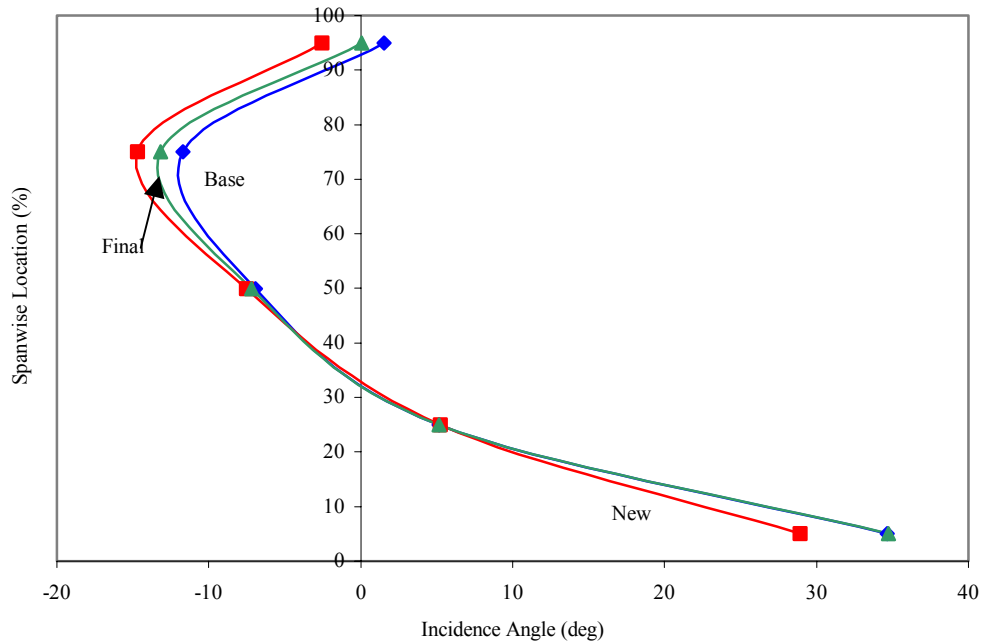


Figure 80. Rotor 67 – Deviation Angle

The changes in the flow field parameters for Rotor 67 were very similar to those observed for the Sanger rotor. Absolute inlet Mach number increased along with mass flow rate, total pressure ratio increased to a higher degree than did total temperature ratio with the accompanying effect on efficiency. As with the Sanger, incidence and deviation angles decreased with the associated positive effects on the flow field. One particular area should be noted. In almost all of these flow field parameter charts, substantial improvements in the values can be observed in both redesigned blades in the hub region. The reason for this is that the baseline Rotor 67 design is very highly cambered at the hub and the camber changes rapidly with span in the inner one third of the blade. This leads to an area of separated flow and high losses in the hub case wall region which can easily be seen in Figure 81, Mach contour maps which compare the flow over the baseline blade to that over the new aerodynamically redesigned blade.

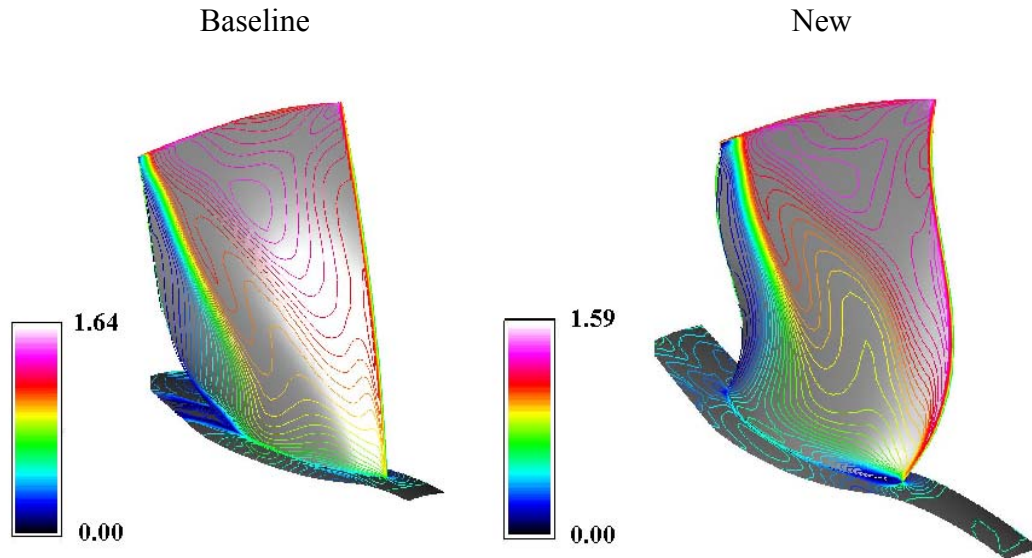


Figure 81. Rotor 67 – New vs. Baseline, Geometry and Mach Number Distribution

The first obvious feature of the new blade is the dramatic change in shape caused by the application of the forward sweep scheme indicated by the optimization process. The large amount of sweep can be seen at the one third span point on the blade along with the tangential translation previously described. The sweep at the tip is much more noticeable here than it was on the Sanger rotor, because it is larger and because it changes less gradually over the span. In any case, the huge region of separated flow near the inner case wall of the baseline blade is easily seen in this view, along with the fact that it is largely absent in the new blade. As mentioned, the camber of the new blade changes more gradually with span, and the translation effect contributes as well. While there are still regions of very low speed flow near the trailing edge of the new blade, and even some near the leading edge at the hub, the effects are not as significant as those observed for the separated region in the baseline. It is interesting to note the resemblance of this new blade to a commercial fan blade introduced by Rolls Royce in 1998. Although the Rolls Royce blade is actually swept aft, the similarity in the contour of the leading edge is striking. This blade is pictured in Figure 82.

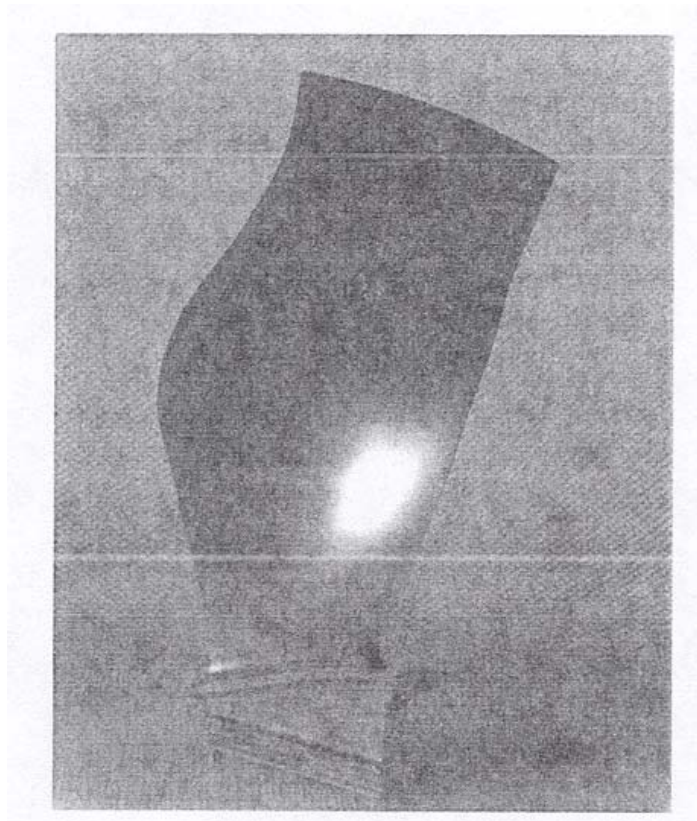


Figure 82. Rolls Royce Commercial Fan Blade (From Ref. 4)

Further comparison of the flow field between the baseline Rotor 67 geometry and the new blade are contained in Figures 83 through 87.

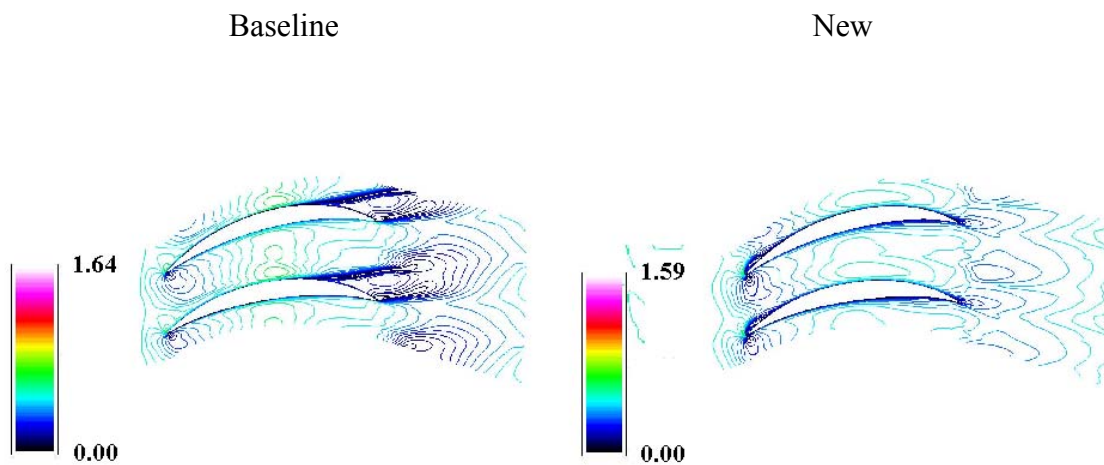


Figure 83. Rotor 67 – New vs. Baseline, Mach Contours near the Hub

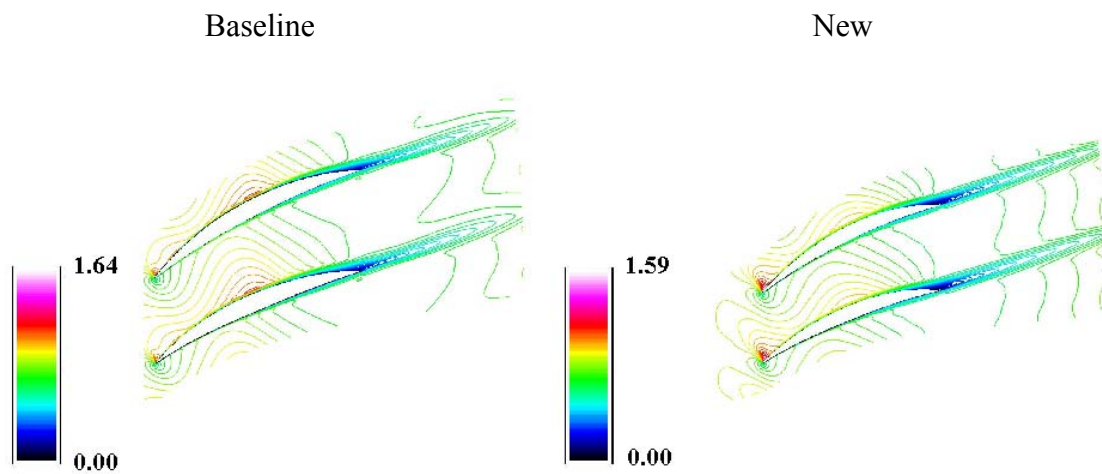


Figure 84. Rotor 67 – New vs. Baseline, Mach Contours at 30% Span

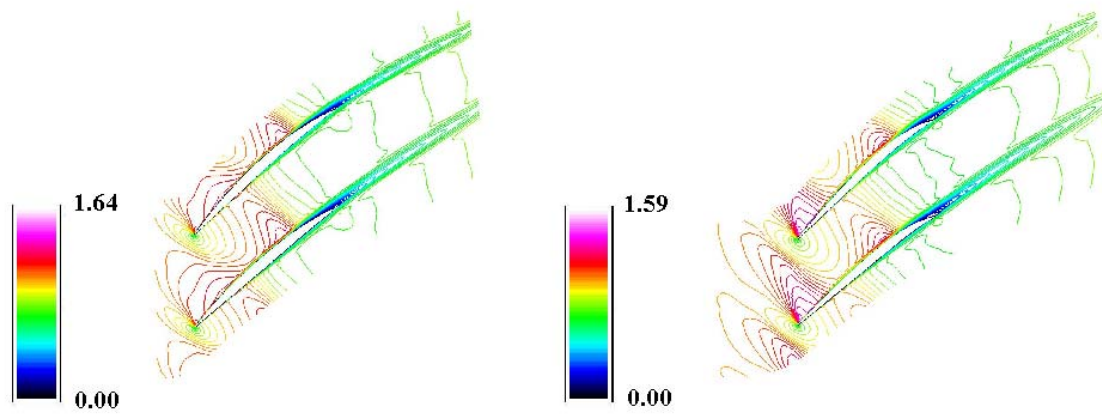


Figure 85. Rotor 67 – New vs. Baseline, Mach Contours at Midspan

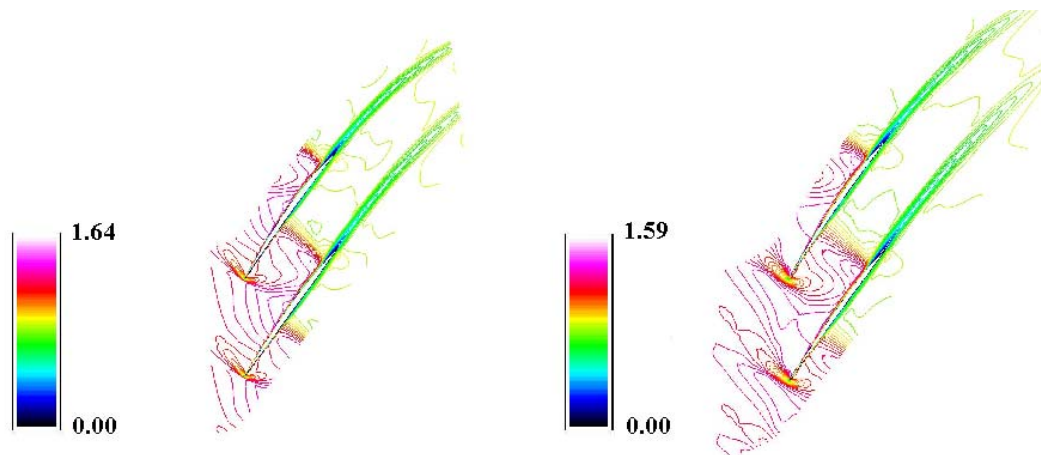


Figure 86. Rotor 67 – New vs. Baseline, Mach Contours at 70% Span

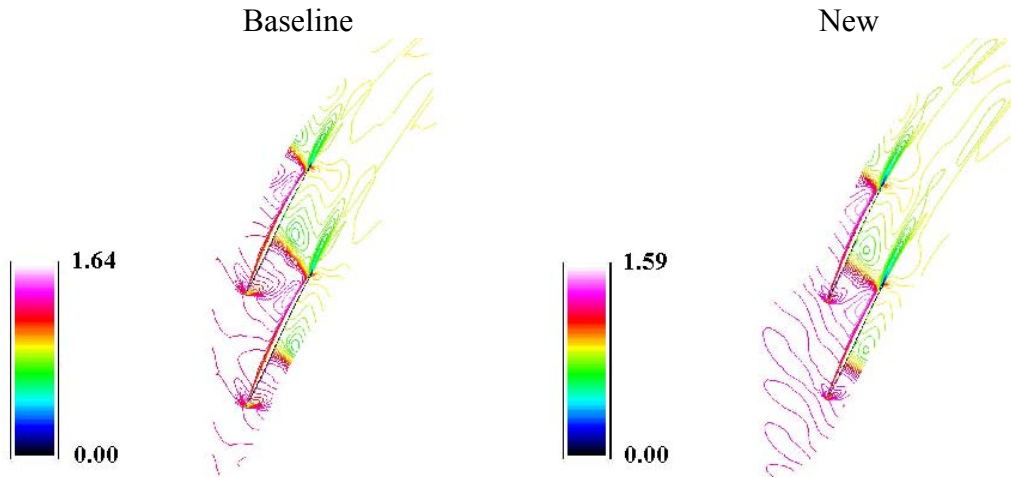


Figure 87. Rotor 67 – New vs. Baseline, Mach Contours near the Tip

In addition to the large wake near the hub, other flow features which contribute to improved performance in the new blade can be observed. First, the overall Mach number is lower which, as with the Sanger rotor, implies a weaker shock structure. Secondly, the passage shock develops more slowly with span in the new blade, and can be seen to be weaker near the tip, where the contour lines are farther apart than in the baseline blade. Finally, the incidence angle near the tip appears to be smaller and it looks like the flow is smoother and more aligned, which would lead to fewer losses in the boundary layer. A contour map of the final design as compared to the baseline blade is shown in Figure 88.

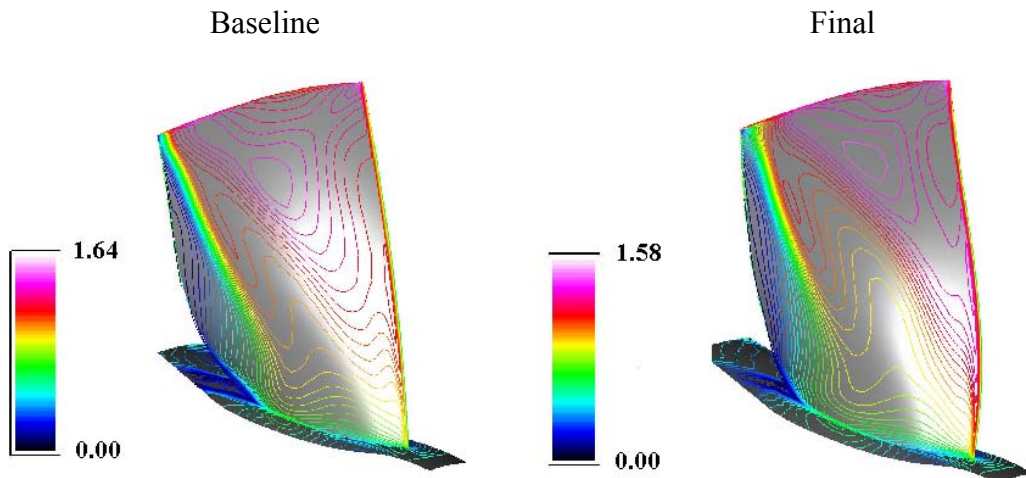


Figure 88. Rotor 67 – Final vs. Baseline, Geometry and Mach Number Distribution

While it is clear that the final design retains some of the forward sweep applied to the new blade, it is obviously far less dramatic, and the overall flow field more closely resembles that of the baseline blade as was indicated by the previous examination of the performance parameters. The overall Mach number is lower, but the region of separated flow is again present at the hub although not to the degree observed for the baseline blade. As with the new blade, the passage shock appears to develop slower with span and is considerably weaker in the tip region. The regions of low speed flow near the trailing edges appear similar in both blades, with the exception of the hub region; although in the baseline blade, it appears to extend a little farther toward the tip thereby contributing to slightly higher viscous losses. Figures 89 through 93 complete the picture of the final design flow field.

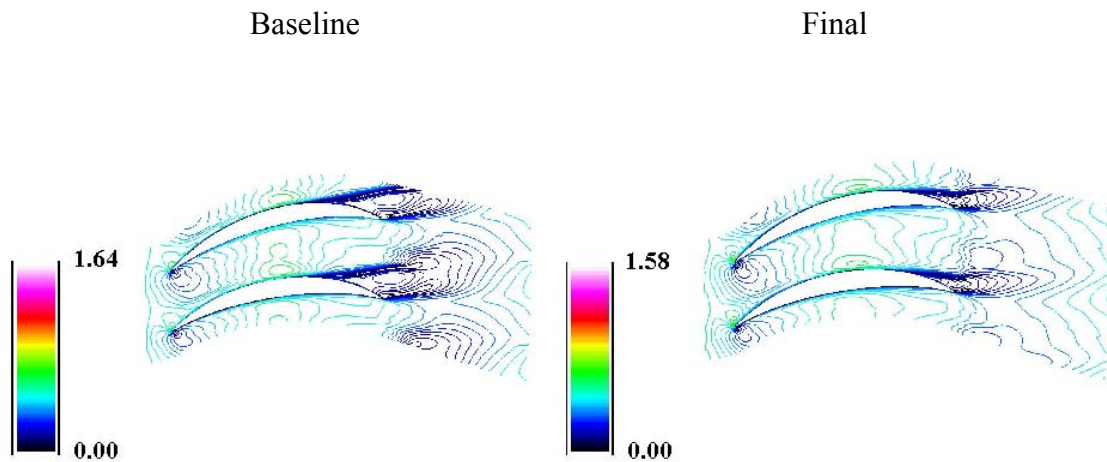


Figure 89. Rotor 67 – Final vs. Baseline, Mach Contours near the Hub

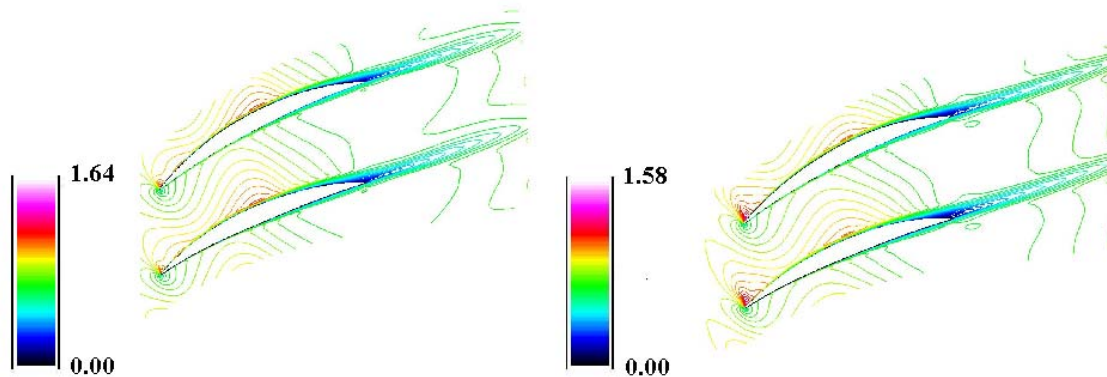


Figure 90. Rotor 67 – Final vs. Baseline, Mach Contours at 30% Span

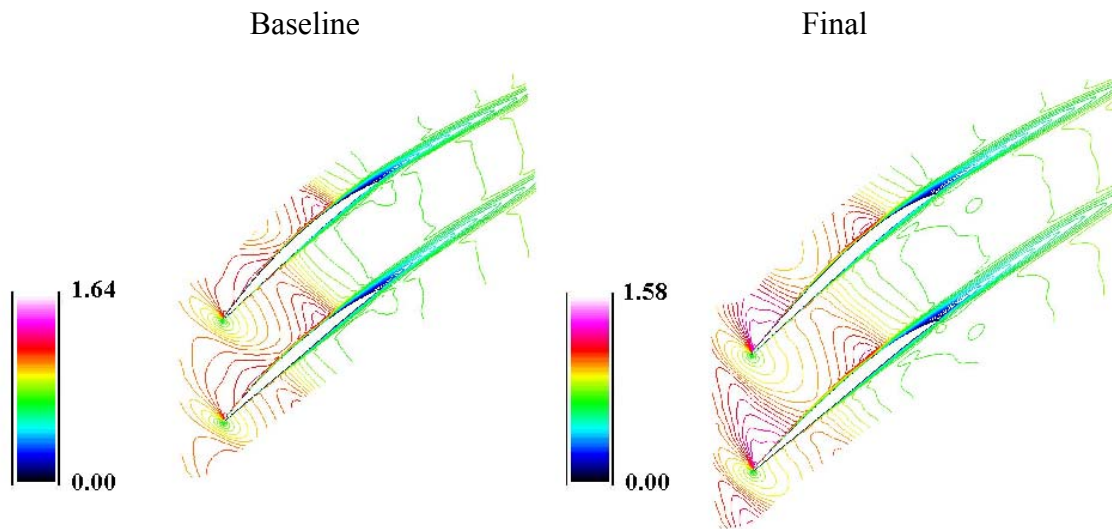


Figure 91. Rotor 67 – Final vs. Baseline, Mach Contours at Midspan

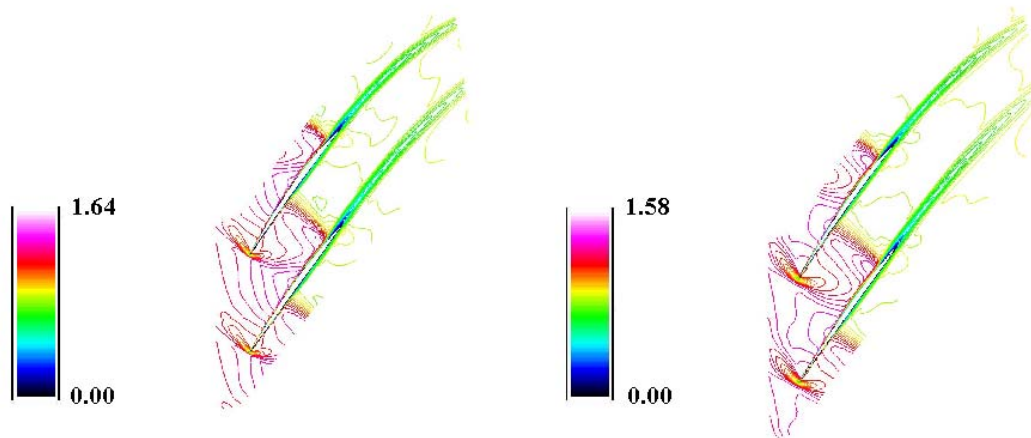


Figure 92. Rotor 67 – Final vs. Baseline, Mach Contours at 70% Span

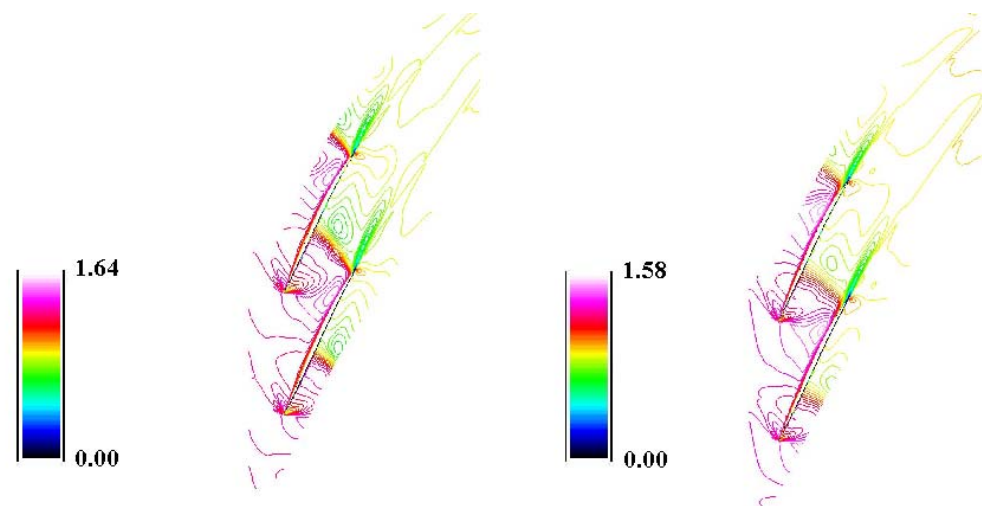


Figure 93. Rotor 67 – Final vs. Baseline, Mach Contours near the Tip

5. Structural Comparison

a. Finite Element Analysis

Finite element analyses were performed for the Rotor 67 baseline, new and final configurations in accordance with the procedures discussed in Section IV. As previously mentioned, the steady stresses in the new blade were found to be far too high and therefore the design was rejected out of hand. The final design was arrived at by removing the majority of forward sweep from the new blade as discussed. The results of the structural analysis for the baseline and final designs are presented in Figures 94 and 95.

Maximum Steady Stress – 115,000 psi
Maximum Deflection - .214 in.

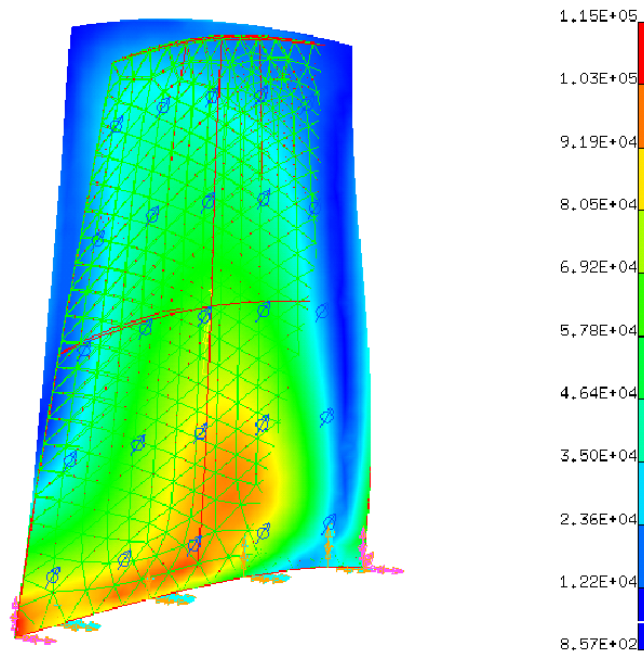


Figure 94. Rotor 67 – Structural Analysis, Baseline Blade

Maximum Steady Stress – 132,000 psi
Maximum Deflection - .241 in.

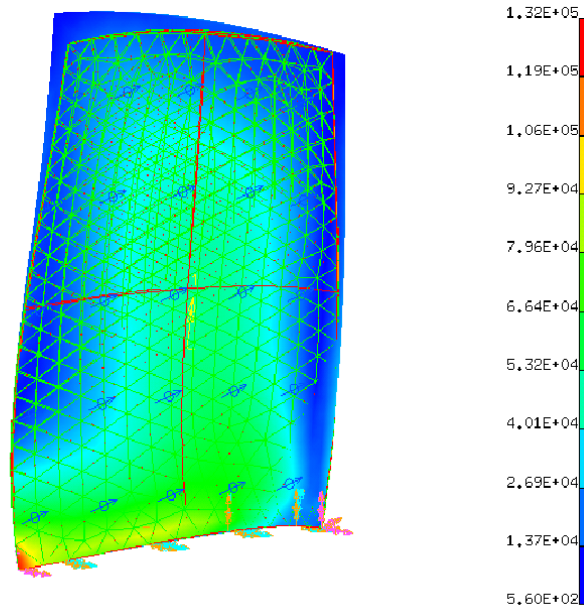


Figure 95. Rotor 67, Structural Analysis, Final Blade

Although the peak stress in the final design is higher than the allowable 120,000 psi, it can be seen that there is just a very small area in the leading edge hub region where this stress occurs. In almost all other areas of the blade, the stress levels are no higher than 100,000 psi which is well below the limit. It is believed that this high stress region can be treated as a stress concentration and is correctible with a slight redesign of the hub-blade interface at the leading edge. The maximum deflections are similar in both blades and are larger than what was observed in the Sanger rotor. This is to be expected since the Rotor 67 blades are heavier, with a much higher aspect ratio and therefore a considerably larger bending moment than the Sanger blades.

b. Cold Shape Correction

A cold shape correction procedure was performed on the Rotor 67 final design in order to find the ‘predeflected’ shape that would produce the aerodynamic design intent when loaded. The result is illustrated in Figure 96.

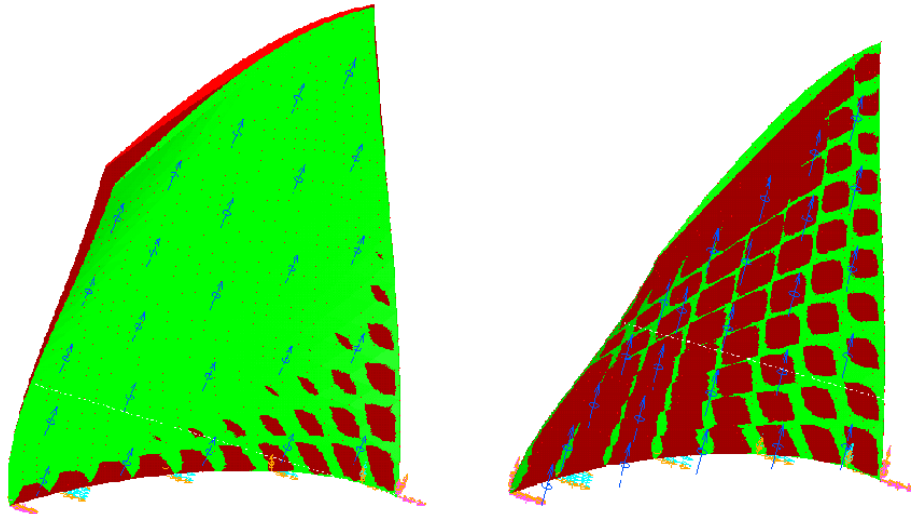


Figure 96. Rotor 67 - Cold Shape Correction

The image on the left shows the aerodynamic design in red and the predefined cold shape (finite element model) in green. The image on the right shows the two superimposed after the finite element model has been placed under the appropriate load. The mottled red-green effect is evidence that the two shapes coincide in the second image. A history of the iterative process required to achieve the proper cold shape is presented in Figure 97. The vertical axis measures the deflection beyond the desired shape during each iteration.

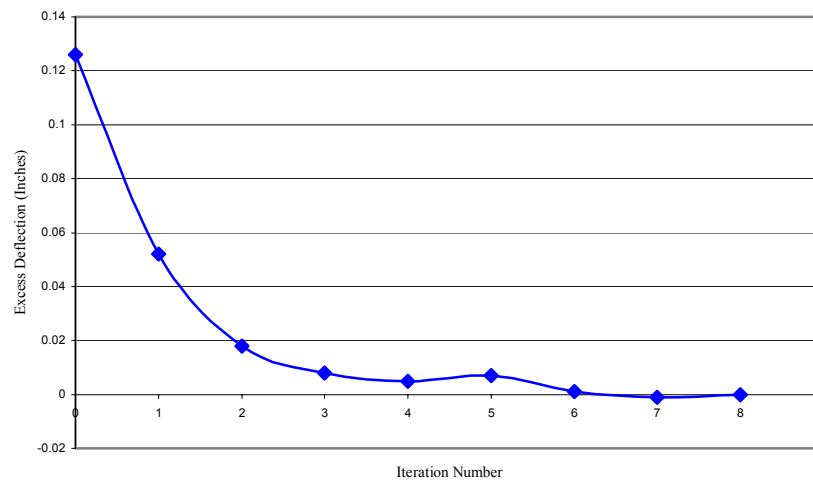


Figure 97. Rotor 67 - Cold Shape Correction History

VI. CONCLUSIONS

The purpose of this study was to evaluate the potential of the BLADE-3D Bezier geometry package in helping to facilitate the development of an automated design optimization process for turbomachinery blades. The work was performed on axial transonic fan blades specifically and involved adapting traditional optimization techniques into a methodology or algorithm which took advantage of the compact blade geometry representation to produce true 3-D shape changes, and then evaluated the performance using high-level CFD software and finite element structural analysis. The author more or less blindly followed the procedure where it led thereby exercising little human judgment in the design decisions normally required in turbomachinery design. This was considered important to the concept of fully automated computerized design.

It is recognized that use of BLADE-3D in the traditional design procedure might limit a designer's ability to make small geometry changes in targeted areas, thereby effectively limiting the design space. This is certainly a limitation of the Bezier geometry representation, but one that is offset by its advantages to the optimization and manufacturing processes. The Bezier representation produces geometries that are inherently smoother than those produced by manipulating individual section profiles thus making them easier to machine. An additional advantage is that since less data is required to fully represent the blade, input files for manufacturing control programs can be smaller and less prone to error.

Although an effective optimization procedure for compressor blades was demonstrated, it is acknowledged that compressors are not designed in a vacuum. The compressor is simply one among several major engine components that must work together to accomplish the overall engine design goal. It may be that optimizing a fan or compressor using the methodology developed here would not necessarily produce the best design for a given application. That should not necessarily diminish the value of the procedure. It does represent a useful tool that a designer may put in his toolkit to use as appropriate.

It is believed that the research was successful in achieving its goal. The blade designs produced herein meet design requirements within the scope of the exercise. While the practicality of the product blades themselves may be questioned further, particularly in the areas of dynamics response and aeroelasticity, the more important point is that the methodology used to design them is viable; it appears to hold promise for incorporation into current design sequences, especially in the final design phase where improving the performance of a preexisting preliminary design is the goal. With more work, particularly in the area of programming, the algorithm presented here could be developed into a complete and automated software package which could take initial blade configurations and transform them into useful final designs with highly tailored performance objectives

A longer range goal of future work would be to adapt the algorithm to include a method to initiate a design. This might mean adapting a Crouse-like capability as an upfront module to the process perhaps using only three axisymmetric streamtubes to produce the four spanwise elements needed to define the initial Bezier geometry.

VII. RECOMMENDATIONS

Abdelhamid made a series of recommendations at the conclusion of Reference 1, two of which were addressed by this work. First of all, it was recommended that a method of calculating traditional design parameters, in conjunction with the use of the Bezier geometry package, be developed and that was done to a partial extent here. Secondly, he recommended that the utility of the package in a design optimization process, to include aerodynamic and structural considerations, be investigated; and again that was accomplished herein. His other recommendations were:

1. That a 3-D grid generator which is fully compatible with the Bezier representation be created. Do not necessarily concur. The MERIDL-like output of BLADE-3D is quite compatible with TCGRID and other similar grid generation programs. It appears that using those tools in conjunction with BLADE-3D poses no threat to its capability.
2. That a technique to start a new blade design using BLADE-3D be developed. Concur.
3. That a graphical user interface be developed to make the geometry package easier to use. Definitely concur. As discussed in Section III, learning and using the package in its current C++ format, particularly with no documentation, was a tedious and time-consuming process. A menu-driven, Windows-based implementation would be especially useful and facilitate future interface with other software programs.

In addition, the following recommendations are made:

4. That further work be performed in the area of structural analysis to incorporate dynamic response, aeroelastic effects and fatigue analysis into the optimization process.
5. That an effort be made to streamline the procedures associated with transferring information between the various software resources utilized in the process up to

and including an overarching computer program to achieve a fully automated capability.

6. That the next extension of this work be to attempt to design a blade from scratch utilizing this optimization process in the final design stage. The intent of the exercise should be to achieve a practical design which could then be built and tested in the lab as further validation of the algorithm and any future enhancements.

APPENDIX A. MODAL ANALYSIS AND FLUTTER

A brief dynamic modal analysis was performed for the blade designs obtained in order to make an initial assessment of the potential for vibration and flutter. The first ten dynamic modes were calculated in I-DEAS for the baseline and new/final designs for both rotors and the results are shown in Table 7.

<u>Normal Mode</u>	<u>Frequency (Hz)</u>			
	<u>Sanger Rotor</u>		<u>Rotor 67</u>	
	<u>Baseline</u>	<u>New</u>	<u>Baseline</u>	<u>Final</u>
1	768.0	353.9	285.9	275.5
2	2780.5	1155.7	777.2	707.3
3	2932.2	1567.9	1323.5	1289.5
4	5242.2	2097.2	1797.7	1680.0
5	5577.4	2564.4	2120.6	1977.8
6	6603.4	2788.3	2477.2	2283.9
7	7876.2	3475.2	2865.3	2797.1
8	9210.8	4084.8	3486.1	3102.7
9	9754.7	4407.0	3724.5	3356.9
10	10211.8	4601.7	3831.5	3608.7

Table 7. Normal Modes and Frequencies

Frequency vs. mode plots were generated for each blade and linear extrapolations performed to obtain approximate values for the higher modes. Since the stator for the Sanger stage contains 27 blades, it was decided that modal excitations could occur, at a minimum, in the regions of 1EO and 27 EO for the Sanger design and those were examined specifically. The same was done for Rotor 67 and the results for both are shown in Figures 98 through 101. The first engine order plots depict frequency vs. mode number for clarity while the 27th engine order plots are traditional Campbell diagrams.

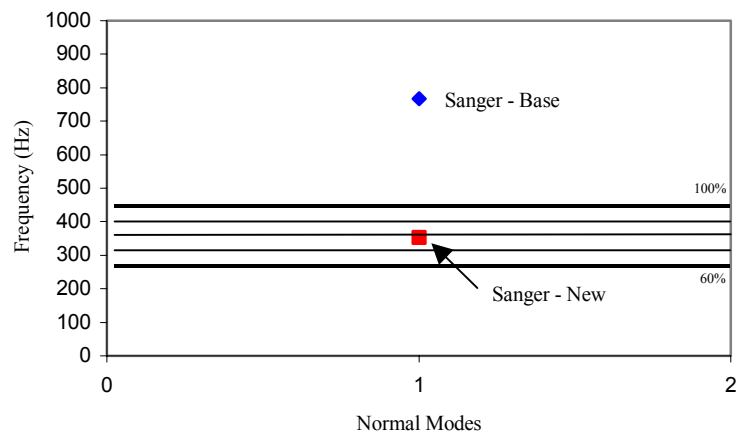


Figure 98. Sanger Rotor - First Engine Order

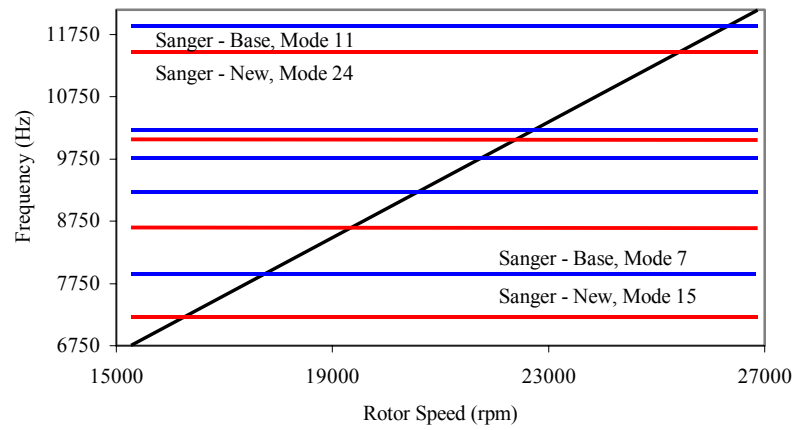


Figure 99. Sanger Rotor - 27th Engine Order

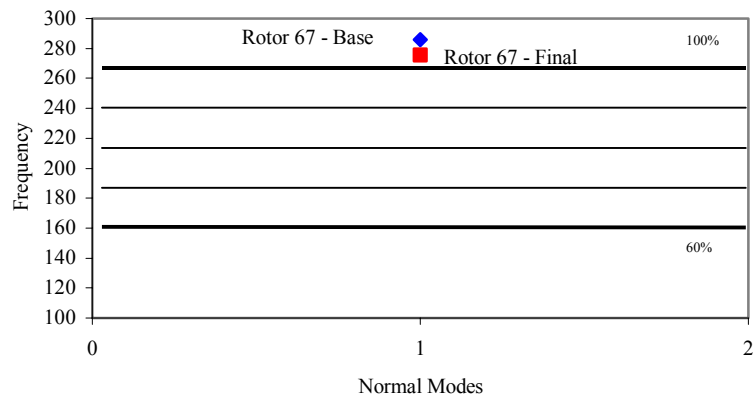


Figure 100. Rotor 67 – First Engine Order

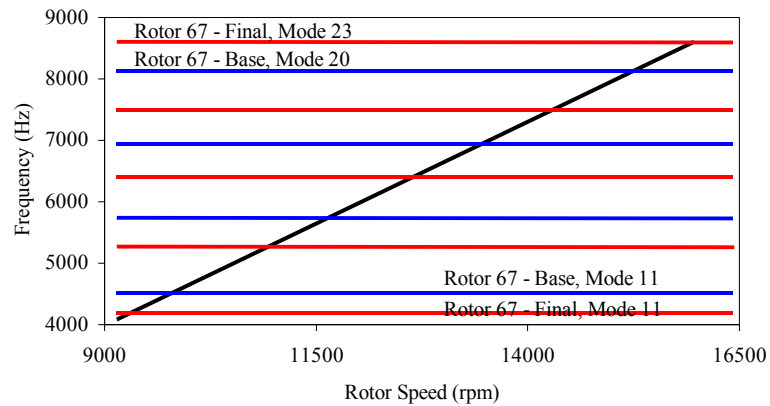


Figure 101. Rotor 67 – 27th Engine Order

The modal analysis shows that in both designs, the frequencies associated with a given structural mode are reduced. For the Sanger rotor, the reduction for each mode was greater than 50% which leads to a problem in the first engine order. It can be seen that the first structural mode for the new Sanger design falls at about the 80% speed point which indicates that the new design has a potential for partial-speed vibration which might be excited by rotor imbalance or upstream flow disturbances. Such increased potential for vibration at the lower structural modes seems intuitive for a very thin blade design. The final Rotor 67 frequencies, while slightly lower than the baseline, create no such problems in the first engine order. The redesign of both rotors might be expected to behave better in the 27th engine order since given frequencies correspond to higher structural modes which are normally more difficult to excite. The difference is much more pronounced in the Sanger design than in Rotor 67.

Aeroelastic characteristics of fan and compressor blades are much more difficult to analyze and predict. A great deal of research has been devoted to more fully understanding the nature of unsteady flow in turbomachines and trying to predict the effects of various design features on the susceptibility to flutter [Ref. 43]. Figure 109 shows different types of flutter and the operating regions where they might be expected to occur in an axial compressor.

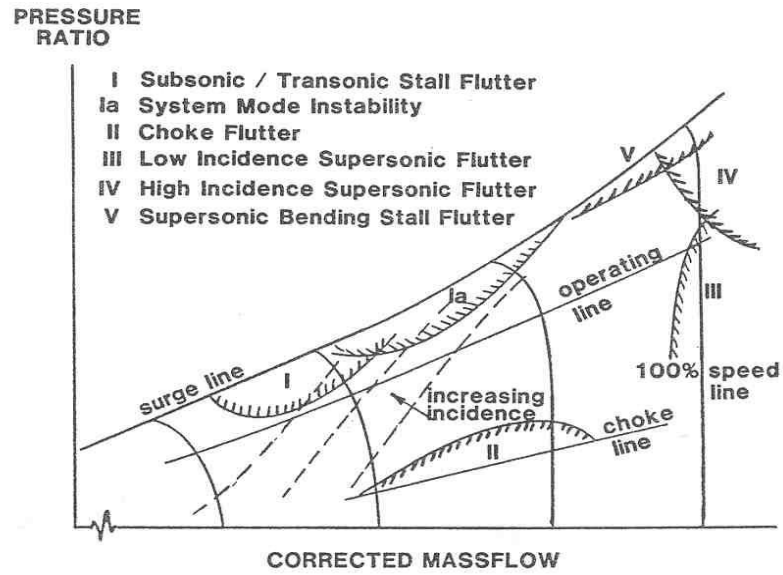


Figure 102. Flutter Boundaries in an Axial Compressor (From Ref. 43)

For the operating regime examined during this study, it appears that the resulting designs would be most susceptible to flutter associated with regions III and IV - supersonic flutter near the 100% speed line. The prominent design features in the optimized blades, thinness and forward sweep, might be expected to have an effect. It is intuitive that thinner blades would most likely be more susceptible to flutter given their increased deflection under load and lower modal response frequencies. It is less appropriate and more difficult to speculate on the effect of forward sweep alone. While forward sweep has been demonstrated to have a detrimental effect on flutter characteristics in external flows, a similar effect has not been shown for fan and compressor blades. There is currently no methodology to predict susceptibility to flutter based simply upon the sweep of the blades. Flutter measurements have been performed on forward swept blades and compared with results produced by CFD [Ref. 44]. The work validated the use of CFD as a tool to predict flutter although no conclusion was drawn as to the contribution of the forward sweep to the flutter mechanisms examined.

Reference 44 demonstrates the idea that structural damping in flutter regions is tied to the location of the passage shock on the blade surfaces. Having the shock near the midchord on the pressure surface is stabilizing while having the shock

near the midchord on the suction surface is destabilizing. It would appear that design changes that cause the passage shock to move forward result in lighter damping and therefore increased susceptibility to flutter. Examination of Figures 92 and 93 show that for the final Rotor 67 design, the passage shock, while weaker, does in fact move forward slightly at 70% and near the tip. This would indicate that the final Rotor 67 design might be more susceptible to flutter but whether it is due primarily to forward sweep needs further study.

APPENDIX B. CALCULATION OF BASIC PARAMETERS

1. Pressure Ratio, Mass Flow Rate and Efficiency

Total pressure ratio, mass flow rate and efficiency are calculated directly from data produced by RVC3D (Appendix F). The output file provides tables of numerous flow properties at both the inlet and exit planes of the computational grid, and in both the absolute and relative frames of reference. Values are provided at the individual grid lines which define the blade span and as average values across the span. The values in the table are those resulting from circumferential averaging of the flow properties and provide an axisymmetric picture of the flow field.

Values for average absolute total pressure vs. reference total pressure at both the inlet and exit planes are obtained from the output. These were used to calculate the total pressure ratio across the rotor. Total temperature ratio was determined in a similar manner. From these, adiabatic efficiency, η , was calculated using the following relationship:

$$\eta = \frac{\pi^{\frac{\gamma-1}{\gamma}} - 1}{\tau - 1} \quad (1)$$

where π is total pressure ratio, τ is total temperature ratio and $\gamma = 1.4$ for air. For a given π , the corresponding total temperature ratio is defined as:

$$\tau = \pi^{\frac{\gamma-1}{\gamma e}} \quad (2)$$

where e is the polytropic efficiency which relates a differential enthalpy change with pressure to that of the ideal process. If total pressure ratio and total temperature ratio are known, polytropic efficiency may be calculated with Equation (2).

Mass flow rate at the inlet can be expressed as:

$$\dot{m} = \rho A V \quad (3)$$

where ρ is the local air density, A is the cross-sectional area of the flow passage and V is the uniform axial flow velocity. A more useful expression for understanding compressor performance is:

$$\dot{m} = \frac{P_t A}{\sqrt{\gamma R T_t}} \gamma M \left[1 + \frac{\gamma - 1}{2} M^2 \right]^{\frac{-(\gamma + 1)}{2(\gamma - 1)}} \quad (4)$$

where P_t , T_t , A , and M are inlet values of total pressure, total temperature, annulus area and flow Mach number respectively. Mass flow rate was computed from Equation (4) using the average absolute inlet Mach number obtained from the RVC3D output. Since reference total temperature and pressure as well as inlet annulus area are constant, the inlet absolute Mach number is a direct indication of the variation in mass flow rate with changes in the blade geometry.

3. Chord Angle, Camber Angle, Incidence and Deviation Angles

Figure 103 is a depiction of blade chord angle (ζ), which was calculated from the MERIDL representation of the blade geometry. It was determined simply by constructing a straight line from the very first MERIDL point describing a blade section profile to the midpoint in that data set, the first point being the trailing edge and the midpoint representing the leading edge in MERIDL. The angle between that line and a line defining the axial direction of the flow was determined from the coordinates of the endpoints.

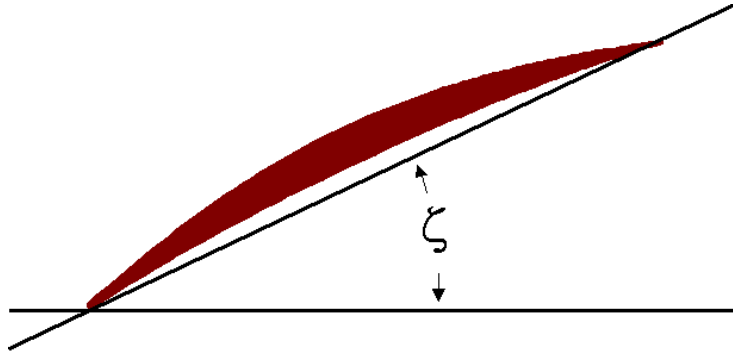


Figure 103. Chord Angle (ζ)

Camber angle is illustrated in Figure 104 and was calculated in the following manner. The first few MERIDL points immediately aft of the leading edge on both the pressure and suction surfaces of the blade are essentially linear. Straight lines were constructed through both sets of points and then the angle between each of these lines and the axial direction was determined in the same manner described for finding the chord angle. The camber-line-to-chord angle (ϕ_{le}) is found by taking the average of these two angles and then subtracting the chord angle. A similar procedure was performed at the trailing edge to determine ϕ_{te} . The sum of these two angles for the leading and trailing edge gave the camber angle (ϕ).

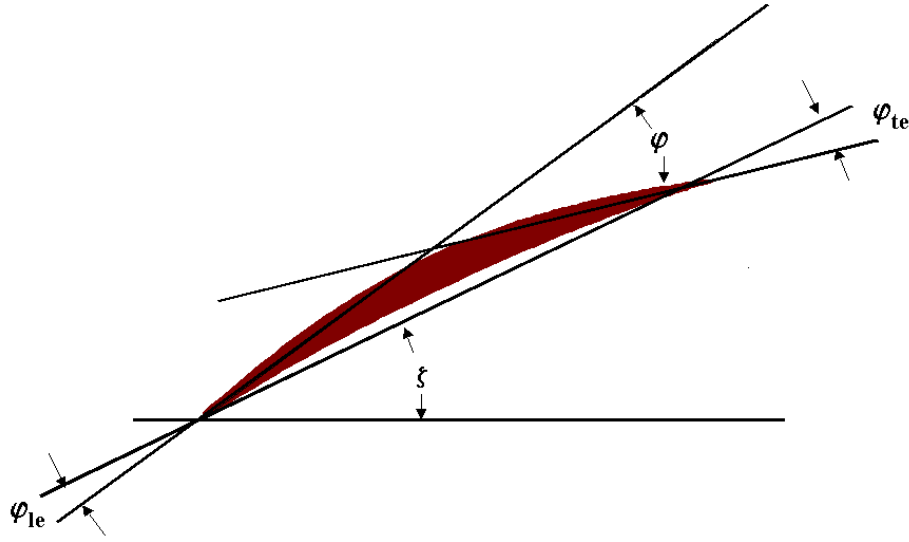


Figure 104. Camber Angle (ϕ)

Incidence (i) and deviation (δ) angles, as shown in Figure 105, were determined using chord angle, camber angle, and data from the RVC3D output file. The output file provides flow angle to the axial at both the inlet (β_1) and exit (β_2) planes. The incidence and deviation angles were calculated using the following relationships:

$$i = \beta_1 - \zeta - \phi_{le} \quad (5)$$

$$\delta = \beta_2 - \zeta + \phi_{te} \quad (6)$$

The sign of the incidence angle is similar to that of angle-of-attack in external flows – positive if the flow is from below the leading edge and negative if from above. The sign of the deviation angle is positive if the flow departs upward (suctionward) from the trailing edge and negative otherwise.

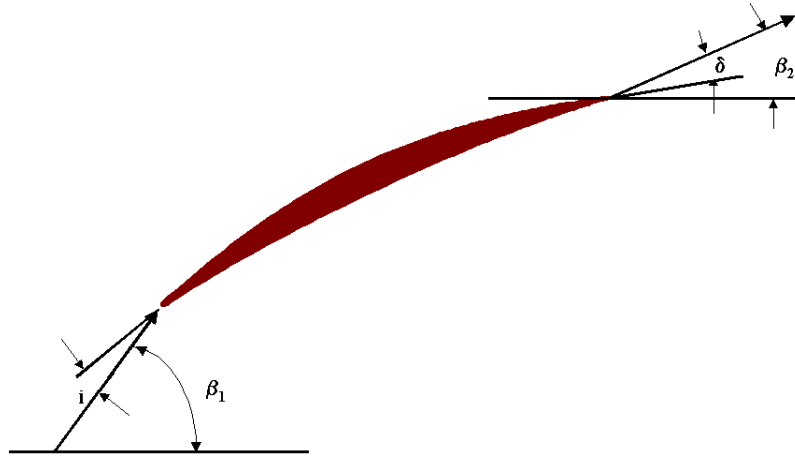


Figure 105. Incidence (i) and Deviation (δ) Angles

3. Blade Thickness

Blade thickness calculations were made in a relatively coarse manner since no precise constraints were placed on thickness other than the requirement that it could not be negative. The process is illustrated in Figures 106 and 107. A good approximation to the actual thickness was computed by first finding the midpoint between a MERIDL pressure surface point and that of its geometric counterpart on the suction surface. That is, if the blade section profile was composed of 50 points, then point 1 would be subtracted from point 50, point 2 from point 49, and so on. Once the midpoint was determined, the closest point on each blade surface was found by way of a sorting procedure. The distance between these two points was then calculated thereby producing a reasonably close estimate of the thickness. The higher the number of points used to define the blade section, the more accurate is the procedure. For this study, 147 surface points were used to describe the blade sections in MERIDL format, with 60 points each on the Bezier pressure and suction surfaces. This provided a reasonably good level of

fidelity in calculating blade thickness. Locations of minimum and maximum thicknesses (d) as a percentage of chord were determined by taking the midpoint defined above for both the minimum and maximum thicknesses, calculating the distances from the leading edge and then taking the cosine along the blade chord.

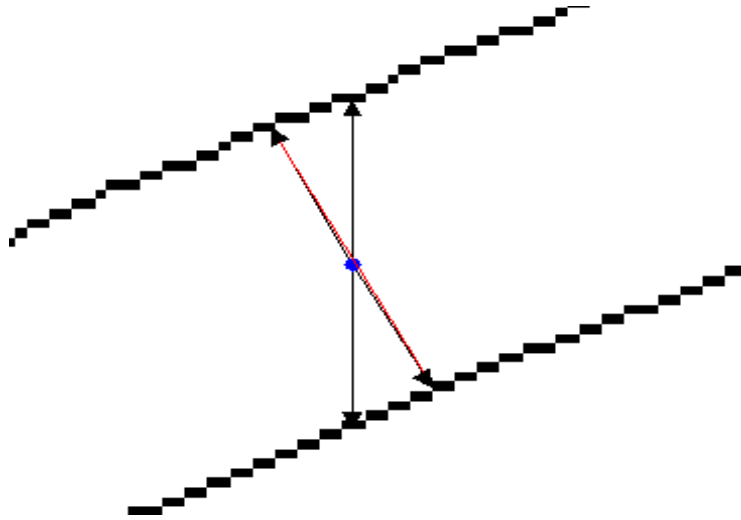


Figure 106. Calculation of Blade Thickness

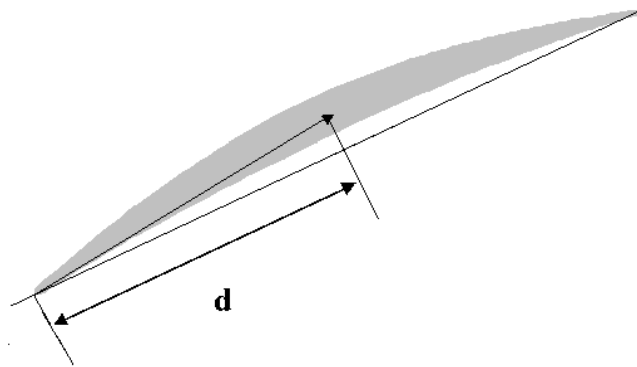


Figure 107. Location of Maximum or Minimum Thickness (d)

As stated, the only constraint applied to blade thickness in the present study was that it not be negative. I-DEAS provided a double check on this constraint in that negative thickness could be easily seen when viewing the blade in the solid modeling

phase of the structural analysis. Of equal utility was the fact that if the blade did not have positive thickness everywhere, then the meshing routine simply would not work, and continuation of the finite element modeling procedure was impossible.

A FORTRAN routine, BPARAM, was developed to calculate the design parameters outlined in this section and may be found in Appendix G.

APPENDIX C. OPTIMIZATION THEORY AND TECHNIQUE

The concept of design optimization involves improving the performance of a system by attempting to maximize or minimize the value of some objective function which is dependent, most often, on the values of multiple design variables [Ref. 45]. For example, it may be desired to maximize the amount of lift generated by a particular wing design where lift is influenced by the size of the wing, its camber, the size and shape of lift enhancing devices along the leading and trailing edges, and many other parameters. Increasing the size of the wing also increases the drag which results in the requirement for more thrust and a bigger, heavier engine. The lift increase achieved by making the wing larger is offset by the weight increase of the wing itself and also by that of the larger engine. The goal of design optimization is to find the right combination of such design variables to achieve the best possible result for the objective function.

Optimization problems come in various shapes and sizes. The given objective may be a function of only one variable, or of very many. The problem may not be subject to constraints in which case the optimization process would proceed to a true maximum or minimum of the objective function. Most design problems are multivariable problems that are constrained by the values of other functions besides the objective. In our example above, the overall weight of the aircraft design is most likely fixed; therefore changes to the size of the wing which result in exceeding this maximum weight would not be allowed. In such optimization problems, the actual maximum or minimum of the objective function is rarely achieved and improvements are limited by the presence of the constraints.

In some problems, there are many variables each of which may assume a wide range of specific values. Ideally, one would wish to look at all the possible combinations of the variables to find the one that provides the absolute maximum or minimum of the objective function. Unfortunately, this is usually not possible. Take for example a problem with three variables each of which may assume one of ten different values. This doesn't sound like a very large problem but there are in fact 1000 different combinations of the variables to consider, a sizeable number even though it would take seconds to solve the problem with a high-speed computer. What if there were 48 variables again with 10 possible values? In that

case, there would be 10^{48} potential combinations, a number that would most certainly require years of computer time to solve. In such problems, the Monte Carlo or random combination technique has proven useful in streamlining the process [Ref. 46]. This procedure generates randomly chosen values of the design variables, combines them and then evaluates the effect on the objective function. For functions with well-defined maxima or minima, a computerized routine to perform this technique can normally get close in a matter of minutes, even for problems with very large numbers of possible solutions. It is used in a variety of optimization applications.

In general, an optimization procedure consists of establishing a starting condition, choosing a direction in which to search for a maximum or minimum of the objective function, and then figuring out how far in that direction to proceed. The starting point may be defined as a vector whose components are the initial values of the design variables under consideration, \mathbf{X}^q , where q is the iteration or run number. The direction of search may be defined as a vector \mathbf{S} whose components are predetermined increments of the design variables. These increments are usually chosen by a sensitivity analysis which changes the values of the individual design variables in turn and then evaluates the effect on the objective function. Both \mathbf{X} and \mathbf{S} are n -dimensional vectors where n is the number of design variables that define the problem. The optimization procedure can then be stated as:

$$\mathbf{X}^q = \mathbf{X}^{q-1} + \alpha_q \mathbf{S}$$

Where α is a measure of how far the process goes in the direction of \mathbf{S} . The value of α is determined by assigning it ever increasing values, substituting it into the above equation and finding the objective function generated by \mathbf{X}^q . The objective function may be plotted against α to find the value that produces the maximum desired improvement. Figure 108 illustrates this process where the objective function is being minimized.

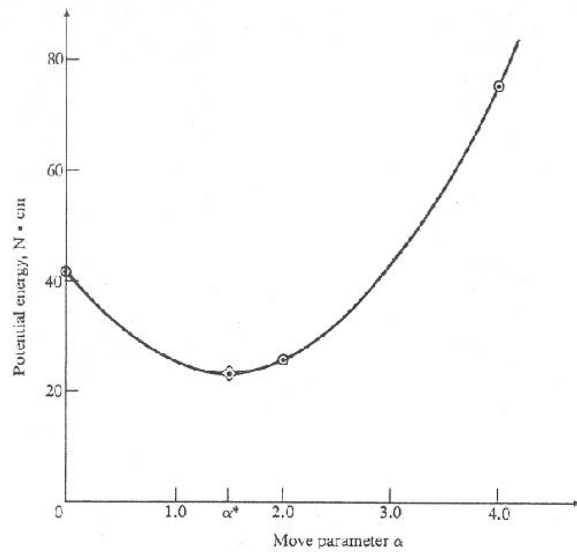


Figure 108. Finding the Search Distance (From Ref. 45)

The procedure outlined above is known as a one-dimensional search. An overview of the results of the process for a two-dimensional minimization problem is shown in Figure 109.

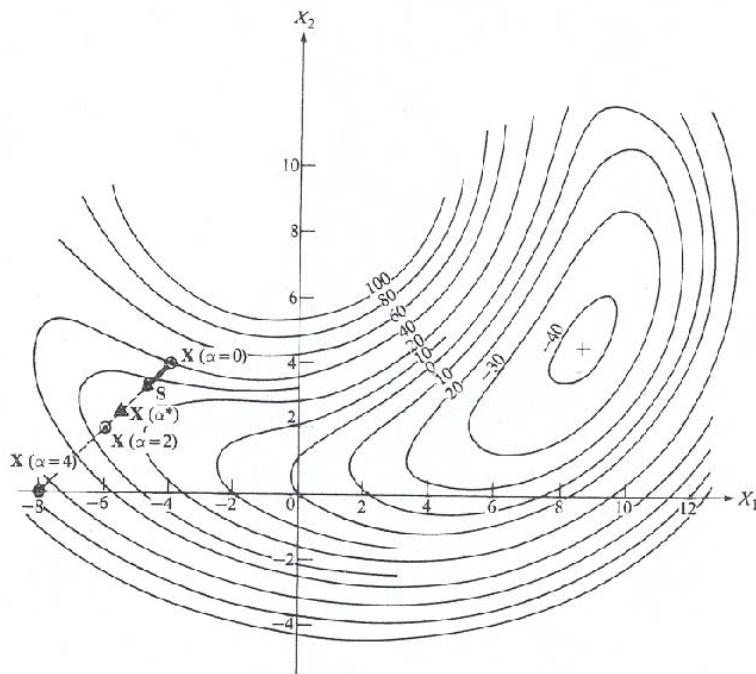


Figure 109. The One-Dimensional Search (From Ref. 45)

For the procedure shown above, the direction vector \mathbf{S} was chosen to be $\begin{pmatrix} -1 \\ -1 \end{pmatrix}$ (perhaps a better choice would have been $\begin{pmatrix} +1 \\ -1 \end{pmatrix}$) and it can be seen that the maximum α determined in the previous figure corresponds to the point at which the search line crosses the contour closest to the minimum. At this point, a new search direction would be determined, most likely something like $\begin{pmatrix} 1 \\ 0 \end{pmatrix}$, and the next iteration or run would be performed. It is clear that several such iterations would arrive at a point very near the minimum. The vector \mathbf{S} may be defined in various ways. The one shown in this example used no gradient information and therefore this particular example is for what is known a zeroth-order optimization method. Methods that use gradient information to establish the magnitude of the components of \mathbf{S} are called first-order methods and there are second-order methods that use second derivative information as well. Second-order methodology was not used in the present study.

Convergence criteria for optimization problems may be expressed in sophisticated mathematical terms but generally consist of checking the gradient of the objective function to ensure that it goes to zero at the optimum. In most practical problems, the end of the process is signaled by the potential for violating a preset constraint if the procedure is continued. Such was the case in the optimization procedures used in the present work.

Numerical optimization can be a very useful design tool. It has some definite advantages but it is acknowledged that there are accompanying disadvantages. Among the positive features are that computerized optimization methods are not biased by intuition and experience in engineering. The possibility of obtaining better, nontraditional designs is enhanced and optimization virtually always leads to some improvement in performance. On the down side, computational time increases as the number of design variables increases and sometimes, the methods become numerically ill-conditioned. Because there is no stored experience or intuition, outcomes are limited by the range of applicability of the underlying analysis program. Finally, it is difficult to guarantee that a process has converged to a true maximum or minimum. For constrained engineering problems, as mentioned, this is not so much of an issue.

APPENDIX D. MERIDL VS. BLADE-3D

1. The following is the MERIDL3 geometry definition for the Sanger rotor.

11	23	22					
0	0.000514	0.002301	0.005027	0.008746	0.013525	0.019448	0.025568
0.031878	0.038395	0.045135	0.052088	0.059237	0.066568	0.074067	0.081719
0.089506	0.097415	0.104086	0.10947	0.113531	0.116248	0.116636	
0.00136	0.001751	0.003532	0.006238	0.009908	0.014595	0.020362	0.026281
0.03235	0.038563	0.044956	0.051567	0.058387	0.065405	0.072609	0.079987
0.087529	0.095222	0.10174	0.107019	0.111013	0.113692	0.114041	
0.002013	0.002353	0.004135	0.006837	0.010492	0.015144	0.020848	0.026682
0.032644	0.038731	0.044945	0.051351	0.057968	0.064787	0.071798	0.078992
0.086358	0.093887	0.100278	0.105463	0.109392	0.112029	0.112356	
0.002617	0.002913	0.004692	0.007384	0.011017	0.015627	0.021259	0.027
0.032848	0.0388	0.044857	0.051036	0.057417	0.064001	0.07078	0.077748
0.084894	0.092212	0.098434	0.10349	0.107325	0.109902	0.110207	
0.003875	0.004123	0.005878	0.008529	0.012096	0.016608	0.022099	0.027672
0.033327	0.039064	0.044881	0.050778	0.056765	0.062939	0.069314	0.075885
0.082643	0.089584	0.095503	0.100323	0.103986	0.10645	0.106724	
0.007383	0.007577	0.009239	0.011743	0.015099	0.019322	0.02443	0.029584
0.034782	0.040025	0.045312	0.050643	0.056018	0.061437	0.066995	0.072754
0.078711	0.084862	0.090132	0.094442	0.097727	0.099942	0.100171	
0.010925	0.011094	0.01264	0.014965	0.018075	0.02198	0.026692	0.03143
0.036196	0.04099	0.045811	0.050659	0.055534	0.060436	0.065366	0.070365
0.075575	0.081001	0.085687	0.089541	0.092492	0.094488	0.09469	
0.012591	0.012749	0.014226	0.016447	0.019417	0.023145	0.027641	0.032161
0.036707	0.041277	0.045871	0.05049	0.055133	0.0598	0.064492	0.06921
0.074074	0.079161	0.083566	0.087197	0.089983	0.091869	0.092059	
0.014092	0.014243	0.015665	0.017803	0.020663	0.024255	0.028587	0.032945
0.037327	0.041734	0.046166	0.050623	0.055105	0.059611	0.064143	0.068699
0.073344	0.078207	0.082428	0.085913	0.088589	0.090402	0.090584	
0.014068	0.014213	0.015624	0.017747	0.020588	0.024157	0.028465	0.0328
0.037163	0.041553	0.045971	0.050417	0.05489	0.05939	0.063918	0.068472
0.073071	0.077861	0.082024	0.085465	0.088111	0.089904	0.090081	
0.014718	0.014854	0.016226	0.018291	0.021057	0.024535	0.028737	0.032972
0.037239	0.041537	0.045868	0.05023	0.054624	0.05905	0.063508	0.067997
0.072518	0.077153	0.081192	0.084538	0.087114	0.088863	0.089032	
0.22289	0.223164	0.224119	0.225574	0.22756	0.230111	0.233273	0.236541
0.23991	0.243389	0.246988	0.250699	0.254516	0.25843	0.262434	0.266519
0.270677	0.274899	0.278461	0.281335	0.283503	0.284954	0.285162	
0.251549	0.251717	0.252483	0.253645	0.255222	0.257236	0.259714	0.262257
0.264864	0.267534	0.270281	0.273121	0.276052	0.279067	0.282162	0.285332
0.288573	0.291878	0.294678	0.296946	0.298663	0.299814	0.299964	
0.267527	0.267655	0.268328	0.269348	0.270728	0.272485	0.274639	0.276842
0.279093	0.281391	0.283738	0.286156	0.288655	0.29123	0.293877	0.296593
0.299375	0.302218	0.304631	0.306589	0.308072	0.309068	0.309192	

0.284586	0.284683	0.285263	0.28614	0.287324	0.288826	0.290661	0.292532
0.294438	0.296378	0.298351	0.300365	0.302444	0.30459	0.306799	0.30907
0.311399	0.313784	0.315811	0.317459	0.318709	0.319549	0.319648	
0.309498	0.309561	0.310012	0.310694	0.311611	0.31277	0.314181	0.315614
0.317067	0.318542	0.320037	0.321552	0.323091	0.324678	0.326317	0.328005
0.329743	0.331527	0.333048	0.334287	0.335228	0.335861	0.335932	
0.357485	0.357513	0.357749	0.358105	0.358582	0.359182	0.359909	0.360641
0.36138	0.362126	0.362877	0.363635	0.364399	0.36517	0.36596	0.366779
0.367626	0.3685	0.369249	0.369862	0.370329	0.370644	0.370677	
0.398682	0.398694	0.3988	0.398959	0.399173	0.399441	0.399764	0.40009
0.400417	0.400746	0.401077	0.40141	0.401744	0.402081	0.402419	0.402763
0.40312	0.403493	0.403815	0.404079	0.404282	0.404419	0.404433	
0.418757	0.418763	0.418826	0.41892	0.419046	0.419204	0.419394	0.419585
0.419778	0.419971	0.420166	0.420362	0.420558	0.420756	0.420955	0.421154
0.42136	0.421576	0.421762	0.421916	0.422034	0.422114	0.422122	
0.428363	0.428368	0.428414	0.428484	0.428578	0.428696	0.428837	0.42898
0.429124	0.429268	0.429413	0.429559	0.429706	0.429853	0.430002	0.430151
0.430303	0.430462	0.4306	0.430714	0.430802	0.430861	0.430867	
0.441651	0.441654	0.441683	0.441726	0.441784	0.441857	0.441945	0.442033
0.442122	0.442211	0.442301	0.442392	0.442483	0.442575	0.442667	0.44276
0.442854	0.442951	0.443036	0.443106	0.44316	0.443197	0.443201	
0.455686	0.455687	0.455696	0.455711	0.45573	0.455754	0.455783	0.455812
0.455841	0.455871	0.455901	0.455931	0.455961	0.455992	0.456023	0.456054
0.456085	0.456117	0.456145	0.456168	0.456186	0.456198	0.456199	
0	0.00313	0.013824	0.029582	0.050062	0.074802	0.103219	0.13024
0.15586	0.179937	0.202284	0.222896	0.241772	0.258919	0.27435	0.288078
0.300126	0.310517	0.31793	0.323057	0.32644	0.328478	0.328755	
0.003128	0.005248	0.014776	0.028894	0.047394	0.069991	0.096331	0.121816
0.146442	0.170204	0.192927	0.214376	0.234537	0.253398	0.270953	0.287196
0.302128	0.315751	0.326106	0.333741	0.33909	0.342478	0.342908	
0.00604	0.00778	0.016799	0.030195	0.047807	0.069419	0.09476	0.119448
0.143479	0.16685	0.189543	0.211273	0.231916	0.251457	0.269884	0.287186
0.303358	0.318393	0.330054	0.338813	0.34505	0.34905	0.349537	
0.007812	0.009253	0.017833	0.030604	0.047445	0.068195	0.092652	0.116621
0.140101	0.163087	0.185579	0.207502	0.228555	0.24869	0.267892	0.286148
0.303448	0.319781	0.33265	0.342455	0.349523	0.354099	0.35463	
0.009343	0.010493	0.0186	0.030696	0.046703	0.066514	0.089999	0.113166
0.136014	0.15854	0.180744	0.202624	0.224143	0.245014	0.26516	0.284567
0.303219	0.321104	0.335414	0.346469	0.354528	0.35979	0.360368	
0.012457	0.013335	0.020849	0.032095	0.047041	0.065645	0.087855	0.109937
0.131892	0.15372	0.175419	0.196989	0.21843	0.239739	0.260729	0.281254
0.301299	0.320851	0.336758	0.349226	0.358424	0.364482	0.365102	
0.015765	0.016553	0.023727	0.034476	0.048786	0.066639	0.088013	0.109331
0.130593	0.1518	0.17295	0.194043	0.21508	0.23606	0.256983	0.277785
0.298246	0.318337	0.334786	0.347746	0.357349	0.363693	0.364329	
0.017368	0.018125	0.025166	0.035718	0.049774	0.067318	0.088335	0.109313
0.130251	0.151148	0.172006	0.192823	0.2136	0.234336	0.255031	0.275683
0.296131	0.316262	0.332787	0.345836	0.355522	0.36193	0.362568	
0.017681	0.018424	0.025428	0.035926	0.049911	0.06737	0.088289	0.109172

0.130021	0.150833	0.17161	0.192351	0.213056	0.233725	0.254357	0.274953
0.295433	0.315629	0.332229	0.345354	0.355104	0.361559	0.362199	
0.020481	0.021191	0.028075	0.038395	0.05214	0.069302	0.089865	0.110394
0.130889	0.15135	0.171776	0.192168	0.212524	0.232846	0.253132	0.273383
0.293579	0.313542	0.329959	0.342944	0.352593	0.358983	0.359607	
0.022265	0.022938	0.029745	0.039948	0.053539	0.070507	0.090839	0.111137
0.131402	0.151632	0.171829	0.191991	0.212119	0.232212	0.25227	0.272292
0.292279	0.312138	0.328482	0.341417	0.351034	0.357405	0.358014	
0.01214	0.013271	0.015723	0.020605	0.026613	0.03327	0.040423	0.04693
0.052625	0.056725	0.058821	0.058171	0.055174	0.050923	0.04564	0.039421
0.032344	0.024471	0.017334	0.011261	0.0065	0.003227	0.002754	
0.008415	0.009086	0.011001	0.015115	0.0203	0.02614	0.032514	0.038449
0.043927	0.048565	0.051401	0.05221	0.050709	0.047455	0.043005	0.037468
0.030935	0.023484	0.01662	0.010724	0.006074	0.002868	0.002444	
0.006996	0.007507	0.009179	0.012944	0.017738	0.023178	0.029159	0.034788
0.04008	0.044786	0.048184	0.049451	0.048574	0.045817	0.041758	0.036547
0.030278	0.023035	0.016306	0.010494	0.005897	0.002722	0.002323	
0.005881	0.006264	0.00769	0.011089	0.01547	0.020478	0.026017	0.031279
0.03631	0.040932	0.044751	0.046737	0.046556	0.044468	0.040876	0.036021
0.030002	0.02291	0.016238	0.010429	0.005811	0.002612	0.002229	
0.004812	0.005074	0.00621	0.009149	0.013	0.017449	0.022407	0.02716
0.031787	0.036186	0.04008	0.043052	0.044156	0.043004	0.040114	0.035758
0.030056	0.023107	0.016429	0.010538	0.005816	0.002528	0.002158	
0.003883	0.004038	0.004859	0.007093	0.010122	0.013734	0.017867	0.021901
0.025897	0.029809	0.033485	0.036674	0.03904	0.039943	0.038515	0.035235
0.030241	0.023646	0.016996	0.010959	0.00603	0.002559	0.002193	
0.003711	0.003821	0.004584	0.006259	0.008616	0.011596	0.015185	0.018781
0.022355	0.025837	0.029117	0.032043	0.034427	0.036053	0.036581	0.034767
0.030549	0.024341	0.017731	0.011542	0.006395	0.002729	0.002349	
0.003711	0.003803	0.004605	0.006016	0.00804	0.010721	0.014083	0.017523
0.020946	0.024251	0.027322	0.030037	0.032265	0.033869	0.034707	0.03394
0.030501	0.024674	0.018166	0.011918	0.006638	0.002844	0.002453	
0.003764	0.003847	0.004695	0.006003	0.007894	0.010468	0.013774	0.017194
0.020602	0.023871	0.02688	0.029512	0.031656	0.033208	0.034068	0.033707
0.030752	0.02508	0.018572	0.012234	0.006836	0.002934	0.002534	
0.003647	0.003714	0.004599	0.00571	0.007335	0.009645	0.012724	0.015971
0.019214	0.0223	0.025098	0.027502	0.029426	0.030807	0.031601	0.031609
0.029519	0.024393	0.018209	0.012062	0.006763	0.002905	0.002513	
0.003567	0.003619	0.004576	0.005519	0.00691	0.009001	0.011916	0.015057
0.018207	0.021177	0.023823	0.026041	0.027763	0.02896	0.029632	0.029767
0.028414	0.024014	0.018085	0.012047	0.006772	0.002905	0.002519	

2. This is the BLADE-3D representation.

11	60	15	10
0.02	0.01		
0.116426	0.0915974	0.269938	
0.0814964	0.0749555	0.256755	
0.0258405	0.0291749	0.237413	
0.0011103	-2.787E-05	0.223518	
0.110617	0.115474	0.296665	
0.0861021	0.0863615	0.304139	
0.0094634	0.0127973	0.268077	
0.0003368	0.0020513	0.27911	
0.0880483	0.152075	0.395773	
0.0824019	0.13402	0.39411	
0.0300771	0.0307192	0.453349	
0.0149014	0.0060386	0.423515	
0.0889173	0.159072	0.427576	
0.0697966	0.117683	0.444517	
0.0318585	0.0471745	0.456041	
0.0154538	0.0109658	0.455618	
0.000524	0.0021362	0.22314	
0.0349709	0.0535454	0.239784	
0.0625972	0.0795338	0.242945	
0.115355	0.092138	0.269125	
0.0005038	0.0028901	0.283852	
0.0120356	0.0230912	0.232444	
0.0732094	0.101217	0.332275	
0.110846	0.113342	0.292469	
0.0142932	0.0070067	0.424733	
0.0245537	0.0215171	0.446428	
0.0777159	0.158137	0.399354	
0.0888766	0.151865	0.391967	
0.0149953	0.0115811	0.455572	
0.0332974	0.0527988	0.456682	
0.06239	0.130432	0.440037	
0.0884033	0.159698	0.427377	

APPENDIX E. INPUT FILES

1. TCGRID

```
&nam1 merid=0 im=185 jm=50 km=49 itl=20
    icap=16 &end
&nam2 nle=15 nte=10 dsle=3.5e-4 dste=2.5e-4 dshub=1.5e-5 dstip=1.5e-5
    dswte=3.5e-4 dswex=.010 dsthr=.39 dsmin=1.2e-5 dsmax=.002
    dsin=.010 clear=.00000 rcorn=.008 ktip=50 &end
&nam3 iterm=50 idbg=0 0 0 0 0 0 0 0 aabb=.6
    cadd=.2 &end
&nam4 zbc=-0.100 -0.040 0.2000 -0.1000 -0.0400 0.2000
    rbc= 0.220 0.220 0.2800 0.4560 0.4560 0.4560 &end
"NPGS TRANSONIC DESIGN -GENER. FROM V8FBND13 INCDP-BASE=DEC13 INMER"
```

```
32 14
-.833 -.667 -.5833 -.50 -.4583 -.425 -.40833 -.3917
-.3333 -.25 -.16666 -.0833 0. .0833 .1 .1167
.125 .133 .14167 .15 .1583 .16666 .175 .183
.19166 .208 .25 .3333 .41666 .5 .667 .8333

.00083 .00083 .00083 .00083 .001667 .00625 .01083 .01667
.04467 .08937 .13405 .17873 .2234 .2681 .277 .286
.2904 .29333 .295583 .297667 .29933 .30033 .30166 .3025
.303333 .304166 .306083 .306083 .306083 .306083 .306083 .306083

-.8333 -.7637 -.666666 -.5 -.33333 -.2083 -.1239 -.04167
.0529 .2167 .3083 .5 .66666 .83333

.4583 .4583 .4583 .4583 .4583 .4583 .4583 .4583
.4583 .4583 .4583 .4583 .4583 .4583
```

(Blade geometry follows in MERIDL0 format)

2. RVC3D

```
'MY ROTOR 1'
&n11 im=185 jm=50 km=49 itl=20 iil=85 ktip=48 &end
&n12 nstg=4 cfl=5 avisc1=0 avisc2=1.0 avisc4=.5 irs=1 epi=0.65 epj=0.75 epk=0.75 ivdt=1
itmax=2000 &end
&n13 ibcin=1 ibcex=3 ires=10 icrnt=50 iresti=0 &end
&n14 om=-2.54 prat=1.19 emxx=.46 alex=52 igeom=1 &end
&n15 ilt=2 iltin=2 renr=6.651e6 tw=0 vispwr=.6667 cmutm=14 jedge=25 kedge=18 srtip=0
xrle=-.2 xrte=0.3 dblh=0.001 dblt=0.02 &end
&n16 &end
```


3. I-DEAS (IGES 5.3)

								S	1
1H,,1H;,7H128-000,11H128-000.IGS,9H{unknown},9H{unknown},16,6,15,13,15,	G							G	1
7H128-000,1.,1,4HINCH,8,0.016,15H19970830.165254,0.0001,0.,	G							G	2
21Hdennette@wiz-worx.com,23HLegacy PDD AP Committee,11,3,	G							G	3
13H920717.080000,23HMIL-PRE-28000B0,CLASS 1;	G							G	4
128 1 0 1 0 0 0 000000001D								D	1
128 0 2 9 0 0 0 D								D	2
128 10 0 1 0 0 0 000000001D								D	3
128 0 2 9 0 0 0 D								D	4
128,3,3,3,3,0,0,1,0,0,0.,1.,1.,1.,2.,2.,2.,3.,0.,1.,1.,1.,2.,2.,	1P							1P	1
2.,3.,1.,1.,1.,1.,1.,1.,1.,1.,1.,1.,1.,1.,1.,1.,3.540936,	1P							1P	2
0.831252,4.575072,2.598936,1.068960,4.484556,0.947748,0.638412,	1P							1P	3
3.969480,0.00000,-0.006696,3.764868,3.422976,2.402880,6.158856,	1P							1P	4
1.754448,0.829080,5.646060,1.967568,1.115340,6.072624,0.299376,	1P							1P	5
-0.097188,6.153444,2.778948,2.669868,7.321752,2.515044,2.573928,	1P							1P	6
8.483112,0.948936,0.410616,8.545572,0.634176,-0.258492,7.700604,	1P							1P	7
2.587080,3.192696,9.218760,1.969404,2.205792,9.654720,1.538328,	1P							1P	8
1.113924,10.011072,0.978336,0.037524,10.060440,0.,3.,0.,3.;	1P							1P	9
128,3,3,3,3,0,0,1,0,0,0.,1.,1.,1.,2.,2.,2.,3.,0.,1.,1.,1.,2.,2.,	3P							3P	10
2.,3.,1.,1.,1.,1.,1.,1.,1.,1.,1.,1.,1.,1.,1.,1.,0.000000,	3P							3P	11
0.032568,3.764736,0.967416,1.078572,3.918900,2.594664,1.447536,	3P							3P	12
4.37328,3.540876,0.866592,4.567932,0.279456,-0.047028,6.058584,	3P							3P	13
1.739280,1.703844,6.444588,1.728276,1.043052,5.132292,3.388200,	3P							3P	14
2.458620,6.189600,0.646344,-0.22752,7.775244,0.934500,0.331344,	3P							3P	15
8.151299,2.469780,2.904432,8.754601,2.786352,2.667948,7.300128,	3P							3P	16
0.978336,0.070224,10.060247,1.48944,1.277724,10.027116,1.94364,	3P							3P	17
2.524860,9.563437,2.575476,3.202704,9.217404,0.,3.,0.,3.;	3P							3P	18
S 1G 4D 4P 18 T 1									

APPENDIX F. RVC3D OUTPUT

```

1
-----
RVC3D: Rotor Viscous Code 3-D, version 208
R. V. Chima, NASA Lewis Research Center
-----
MY ROTOR 1
-----

***** namelist input

      &nl1 - grid parameters
      im      jm      km      itl      iil      ktip
      185     50     49     20     85     48

      &nl2 - algorithm parameters
      nstg     cfl     avisc1     avisc2     avisc4
      4       5.00000  0.00000  1.00000  0.50000
      irs      eps     epi      epj      epk      itmax
ivdt          1      0.00000  0.65000  0.75000  0.75000      2000
1

      &nl3 - boundary condition & code control
      ibcin     ibcex     isymt     ires     icrnt     iresti
iresto         iqin     mioe
1              1         3         0         10         50         0
1              0         3

      &nl4 - flow parameters
      igeom     ga      om      prat     emxx     emty
emrz          expt     alex
0.00000       1       1.40000  -2.54000  1.19000  0.46000  0.00000
0.00000  0.00000  52.00000

      &nl5 - viscous parameters
      ilt      renr      prnr      tw      vispwr      prtr
cmutm        jedge     kedge
14.00000     2 6651000.0  0.70000  0.00000  0.66670  0.90000
25          18

      iltin     dblh     dblt     srtip     xrle     xrte
2      0.00100  0.02000  0.00000  -0.20000  0.30000

      &nl6 - output control
      nko
      0

```

***** annular geometry, pitch = -0.286 radians

```

***** ibcin=1, inlet vt & merid. angle specified
***** ibcex=3, radial equil. spanwise, constant p b-b
***** inlet profile calculated from input
***** initial conditions generated internally
***** time step limit

```

```

          cfl      dtmin      imin      jmin      kmin
        5.000  1.52E-05      165       2       30

```

1

```

-----
theta-direction averaged quantities on inlet
primitive variables, absolute system
approximate energy average
notation: rr=rho0ref, cr=c0ref, er=rr*cr**2, pr=p0ref,
tr=t0ref, alpha=atan(vth/u), phi=atan(vr/u)
-----

```

e/er	k	distance	% mdot	rho/rr	u/cr	vth/cr	vr/cr
	ps/pr	p0/pr	ts/tr	t0/tr	Mach		
	1	0.20572	0.00000	0.91288	0.00000	-0.51293	0.00000
1.66445	0.86484	1.04496	0.94738	1.00000	0.52698		
	2	0.20574	0.00000	0.90115	0.05973	-0.44472	0.00000
1.63512	0.86486	0.99868	0.95973	1.00000	0.45804		
	3	0.20576	0.00002	0.88766	0.17616	-0.31178	0.00000
1.60137	0.86489	0.94723	0.97435	1.00000	0.36279		
	4	0.20580	0.00007	0.88517	0.26404	-0.21148	0.00000
1.59513	0.86491	0.93792	0.97711	1.00000	0.34223		
	5	0.20586	0.00015	0.88576	0.29265	-0.17894	0.00000
1.59661	0.86492	0.94010	0.97647	1.00000	0.34713		
	6	0.20593	0.00028	0.88699	0.32021	-0.14765	0.00000
1.59967	0.86493	0.94462	0.97513	1.00000	0.35708		
	7	0.20604	0.00049	0.88901	0.34967	-0.11428	0.00000
1.60470	0.86495	0.95213	0.97293	1.00000	0.37295		
	8	0.20620	0.00082	0.89227	0.38383	-0.07566	0.00000
1.61284	0.86495	0.96438	0.96939	1.00000	0.39734		
	9	0.20643	0.00134	0.89719	0.42259	-0.03196	0.00000
1.62514	0.86496	0.98311	0.96408	1.00000	0.43162		
	10	0.20676	0.00215	0.90157	0.45056	0.00000	0.00000
1.63609	0.86496	1.00000	0.95940	1.00000	0.46000		
	11	0.20723	0.00335	0.90157	0.45056	0.00000	0.00000
1.63609	0.86496	1.00000	0.95940	1.00000	0.46000		
	12	0.20791	0.00507	0.90157	0.45056	0.00000	0.00000
1.63609	0.86496	1.00000	0.95940	1.00000	0.46000		
	13	0.20887	0.00753	0.90157	0.45056	0.00000	0.00000
1.63608	0.86496	1.00000	0.95940	1.00000	0.46000		
	14	0.21024	0.01107	0.90157	0.45056	0.00000	0.00000
1.63609	0.86496	1.00000	0.95940	1.00000	0.46000		
	15	0.21219	0.01612	0.90157	0.45056	0.00000	0.00000
1.63608	0.86496	1.00000	0.95940	1.00000	0.46000		

	16	0.21494	0.02333	0.90157	0.45056	0.00000	0.00000
1.63608		0.86496	1.00000	0.95940	1.00000	0.46000	
	17	0.21878	0.03357	0.90157	0.45056	0.00000	0.00000
1.63609		0.86496	1.00000	0.95940	1.00000	0.46000	
	18	0.22410	0.04801	0.90157	0.45056	0.00000	0.00000
1.63608		0.86496	1.00000	0.95940	1.00000	0.46000	
	19	0.23135	0.06821	0.90157	0.45056	0.00000	0.00000
1.63609		0.86496	1.00000	0.95940	1.00000	0.46000	
	20	0.24102	0.09607	0.90157	0.45056	0.00000	0.00000
1.63608		0.86496	1.00000	0.95940	1.00000	0.46000	
	21	0.25357	0.13376	0.90157	0.45056	0.00000	0.00000
1.63609		0.86496	1.00000	0.95940	1.00000	0.46000	
	22	0.26927	0.18338	0.90157	0.45056	0.00000	0.00000
1.63609		0.86496	1.00000	0.95940	1.00000	0.46000	
	23	0.28805	0.24634	0.90157	0.45056	0.00000	0.00000
1.63609		0.86496	1.00000	0.95940	1.00000	0.46000	
	24	0.30933	0.32251	0.90157	0.45056	0.00000	0.00000
1.63608		0.86496	1.00000	0.95940	1.00000	0.46000	
	25	0.33203	0.40953	0.90157	0.45056	0.00000	0.00000
1.63609		0.86496	1.00000	0.95940	1.00000	0.46000	
	26	0.35473	0.50274	0.90157	0.45056	0.00000	0.00000
1.63609		0.86496	1.00000	0.95940	1.00000	0.46000	
	27	0.37601	0.59599	0.90157	0.45056	0.00000	0.00000
1.63609		0.86496	1.00000	0.95940	1.00000	0.46000	
	28	0.39478	0.68323	0.90157	0.45056	0.00000	0.00000
1.63609		0.86496	1.00000	0.95940	1.00000	0.46000	
	29	0.41047	0.75992	0.90157	0.45056	0.00000	0.00000
1.63609		0.86496	1.00000	0.95940	1.00000	0.46000	
	30	0.42301	0.82379	0.90157	0.45056	0.00000	0.00000
1.63609		0.86496	1.00000	0.95940	1.00000	0.46000	
	31	0.43268	0.87464	0.90157	0.45056	0.00000	0.00000
1.63609		0.86496	1.00000	0.95940	1.00000	0.46000	
	32	0.43993	0.91356	0.90095	0.44691	0.00000	0.00000
1.63454		0.86496	0.99761	0.96005	1.00000	0.45611	
	33	0.44525	0.94176	0.89694	0.42219	0.00000	0.00000
1.62451		0.86496	0.98214	0.96435	1.00000	0.42992	
	34	0.44909	0.96111	0.89285	0.39522	0.00000	0.00000
1.61430		0.86496	0.96658	0.96876	1.00000	0.40154	
	35	0.45184	0.97415	0.88955	0.37181	0.00000	0.00000
1.60606		0.86496	0.95414	0.97235	1.00000	0.37706	
	36	0.45378	0.98289	0.88692	0.35187	0.00000	0.00000
1.59948		0.86496	0.94430	0.97524	1.00000	0.35631	
	37	0.45515	0.98874	0.88471	0.33411	0.00000	0.00000
1.59395		0.86496	0.93609	0.97767	1.00000	0.33790	
	38	0.45612	0.99264	0.88276	0.31749	0.00000	0.00000
1.58906		0.86496	0.92887	0.97984	1.00000	0.32074	
	39	0.45679	0.99524	0.88096	0.30138	0.00000	0.00000
1.58458		0.86496	0.92228	0.98183	1.00000	0.30416	
	40	0.45726	0.99695	0.87929	0.28541	0.00000	0.00000
1.58039		0.86496	0.91615	0.98371	1.00000	0.28776	
	41	0.45759	0.99808	0.87770	0.26935	0.00000	0.00000
1.57641		0.86496	0.91036	0.98549	1.00000	0.27133	
	42	0.45782	0.99882	0.87618	0.25301	0.00000	0.00000
1.57262		0.86496	0.90486	0.98720	1.00000	0.25465	
	43	0.45798	0.99931	0.87472	0.23618	0.00000	0.00000
1.56897		0.86496	0.89960	0.98884	1.00000	0.23751	

	44	0.45809	0.99962	0.87330	0.21854	0.00000	0.00000
1.56543		0.86496	0.89451	0.99045	1.00000	0.21959	
	45	0.45816	0.99982	0.87191	0.19959	0.00000	0.00000
1.56194		0.86496	0.88952	0.99203	1.00000	0.20039	
	46	0.45822	0.99993	0.86796	0.13152	0.00000	0.00000
1.55208		0.86496	0.87551	0.99654	1.00000	0.13174	
	47	0.45826	0.99998	0.86584	0.07119	0.00000	0.00000
1.54677		0.86496	0.86804	0.99899	1.00000	0.07123	
	48	0.45829	1.00000	0.86506	0.02413	0.00000	0.00000
1.54482		0.86496	0.86531	0.99988	1.00000	0.02413	
	49	0.45830	1.00000	0.86496	0.00000	0.00000	0.00000
1.54457		0.86496	0.86496	1.00000	1.00000	0.00000	

----- overall averages -----

	50	0.35522	0.00965	0.90078	0.44585	-0.00451	0.00000
1.63411		0.86496	0.99694	0.96024	1.00000	0.45501	

1

theta-direction averaged quantities on exit

primitive variables, absolute system

approximate energy average

notation: rr=rho0ref, cr=c0ref, er=rr*cr**2, pr=p0ref,
tr=t0ref, alpha=atan(vth/u), phi=atan(vr/u)

e/er	k	distance	% mdot	rho/rr	u/cr	vth/cr	vr/cr
	ps/pr	p0/pr	ts/tr	t0/tr	Mach		
	1	0.30384	0.00000	1.22080	0.00000	0.00000	0.00000
2.36111	1.32222	1.32222	1.08308	1.08308	0.00000		
	2	0.30386	0.00001	1.22080	0.05525	-0.05317	0.00000
2.36470	1.32222	1.32725	1.08307	1.08425	0.07368		
	3	0.30389	0.00005	1.22080	0.16050	-0.15445	0.00000
2.39140	1.32222	1.36511	1.08307	1.09300	0.21403		
	4	0.30392	0.00014	1.22080	0.23988	-0.23086	0.00000
2.42877	1.32222	1.41939	1.08307	1.10524	0.31990		
	5	0.30397	0.00031	1.22080	0.26606	-0.25604	0.00000
2.44433	1.32222	1.44245	1.08307	1.11034	0.35480		
	6	0.30404	0.00056	1.22080	0.29151	-0.28054	0.00000
2.46102	1.32222	1.46746	1.08307	1.11581	0.38875		
	7	0.30414	0.00095	1.22080	0.31905	-0.30704	0.00000
2.48079	1.32222	1.49750	1.08307	1.12229	0.42548		
	8	0.30428	0.00155	1.22080	0.35151	-0.33828	0.00000
2.50638	1.32222	1.53702	1.08307	1.13067	0.46876		
	9	0.30447	0.00248	1.22080	0.38914	-0.37450	0.00000
2.53915	1.32222	1.58872	1.08307	1.14141	0.51895		
	10	0.30474	0.00390	1.22080	0.41693	-0.40123	0.00000
2.56548	1.32222	1.63114	1.08307	1.15004	0.55600		
	11	0.30511	0.00593	1.22080	0.41693	-0.40123	0.00000
2.56548	1.32222	1.63114	1.08307	1.15004	0.55600		
	12	0.30564	0.00878	1.22080	0.41693	-0.40123	0.00000
2.56548	1.32222	1.63114	1.08307	1.15004	0.55600		

	13	0.30637	0.01276	1.22080	0.41693	-0.40123	0.00000
2.56548	1.32222	1.63114	1.08307	1.15004	0.55600		
	14	0.30738	0.01828	1.22080	0.41693	-0.40123	0.00000
2.56548	1.32222	1.63114	1.08307	1.15004	0.55600		
	15	0.30879	0.02595	1.22080	0.41693	-0.40123	0.00000
2.56548	1.32222	1.63114	1.08307	1.15004	0.55600		
	16	0.31072	0.03651	1.22080	0.41693	-0.40123	0.00000
2.56548	1.32222	1.63114	1.08307	1.15004	0.55600		
	17	0.31335	0.05097	1.22080	0.41693	-0.40123	0.00000
2.56548	1.32222	1.63114	1.08308	1.15004	0.55600		
	18	0.31689	0.07058	1.22080	0.41693	-0.40123	0.00000
2.56548	1.32222	1.63114	1.08307	1.15004	0.55600		
	19	0.32158	0.09681	1.22080	0.41693	-0.40123	0.00000
2.56548	1.32222	1.63114	1.08307	1.15004	0.55600		
	20	0.32767	0.13130	1.22080	0.41693	-0.40123	0.00000
2.56548	1.32222	1.63114	1.08307	1.15004	0.55600		
	21	0.33536	0.17555	1.22080	0.41693	-0.40123	0.00000
2.56548	1.32222	1.63114	1.08307	1.15004	0.55600		
	22	0.34475	0.23066	1.22080	0.41693	-0.40123	0.00000
2.56548	1.32222	1.63114	1.08307	1.15004	0.55600		
	23	0.35576	0.29682	1.22080	0.41693	-0.40123	0.00000
2.56548	1.32222	1.63114	1.08307	1.15004	0.55600		
	24	0.36805	0.37280	1.22080	0.41693	-0.40123	0.00000
2.56548	1.32222	1.63114	1.08307	1.15004	0.55600		
	25	0.38107	0.45584	1.22080	0.41693	-0.40123	0.00000
2.56548	1.32222	1.63114	1.08307	1.15004	0.55600		
	26	0.39408	0.54183	1.22080	0.41693	-0.40123	0.00000
2.56548	1.32222	1.63114	1.08307	1.15004	0.55600		
	27	0.40637	0.62602	1.22080	0.41693	-0.40123	0.00000
2.56548	1.32222	1.63114	1.08307	1.15004	0.55600		
	28	0.41738	0.70404	1.22080	0.41693	-0.40123	0.00000
2.56548	1.32222	1.63114	1.08307	1.15004	0.55600		
	29	0.42678	0.77267	1.22080	0.41693	-0.40123	0.00000
2.56548	1.32222	1.63114	1.08307	1.15004	0.55600		
	30	0.43447	0.83033	1.22080	0.41693	-0.40123	0.00000
2.56548	1.32222	1.63114	1.08307	1.15004	0.55600		
	31	0.44056	0.87692	1.22080	0.41693	-0.40123	0.00000
2.56548	1.32222	1.63114	1.08307	1.15004	0.55600		
	32	0.44525	0.91324	1.22080	0.41326	-0.39770	0.00000
2.56190	1.32222	1.62533	1.08307	1.14887	0.55111		
	33	0.44879	0.94014	1.22080	0.38866	-0.37403	0.00000
2.53872	1.32222	1.58802	1.08307	1.14127	0.51831		
	34	0.45142	0.95904	1.22080	0.36218	-0.34855	0.00000
2.51533	1.32222	1.55102	1.08307	1.13361	0.48299		
	35	0.45335	0.97210	1.22080	0.33946	-0.32669	0.00000
2.49660	1.32222	1.52182	1.08307	1.12747	0.45270		
	36	0.45476	0.98109	1.22080	0.32031	-0.30825	0.00000
2.48174	1.32222	1.49894	1.08307	1.12260	0.42715		
	37	0.45578	0.98726	1.22080	0.30339	-0.29197	0.00000
2.46933	1.32222	1.48003	1.08307	1.11853	0.40458		
	38	0.45651	0.99148	1.22080	0.28766	-0.27683	0.00000
2.45840	1.32222	1.46351	1.08307	1.11495	0.38361		
	39	0.45703	0.99436	1.22080	0.27251	-0.26225	0.00000
2.44842	1.32222	1.44854	1.08308	1.11168	0.36341		
	40	0.45741	0.99631	1.22080	0.25758	-0.24788	0.00000
2.43911	1.32222	1.43469	1.08307	1.10863	0.34349		

	41	0.45768	0.99763	1.22080	0.24264	-0.23351	0.00000
2.43033	1.32222	1.42170	1.08307	1.10576	0.32358		
	42	0.45787	0.99852	1.22080	0.22753	-0.21896	0.00000
2.42198	1.32222	1.40941	1.08307	1.10302	0.30342		
	43	0.45801	0.99911	1.22080	0.21204	-0.20406	0.00000
2.41397	1.32222	1.39772	1.08307	1.10039	0.28277		
	44	0.45810	0.99950	1.22080	0.19589	-0.18851	0.00000
2.40623	1.32222	1.38647	1.08307	1.09786	0.26123		
	45	0.45817	0.99975	1.22080	0.17862	-0.17189	0.00000
2.39862	1.32222	1.37548	1.08307	1.09536	0.23820		
	46	0.45822	0.99990	1.22080	0.11716	-0.11275	0.00000
2.37725	1.32222	1.34496	1.08307	1.08836	0.15624		
	47	0.45826	0.99997	1.22080	0.06326	-0.06088	0.00000
2.36582	1.32222	1.32882	1.08307	1.08462	0.08437		
	48	0.45829	0.99999	1.22080	0.02142	-0.02062	0.00000
2.36165	1.32222	1.32298	1.08307	1.08325	0.02857		
	49	0.45830	1.00000	1.22080	0.00000	0.00000	0.00000
2.36111	1.32222	1.32222	1.08308	1.08308	0.00000		
----- overall averages -----							

	50	0.38882	0.00840	1.22080	0.41202	-0.39651	0.00000
2.56070	1.32222	1.62338	1.08307	1.14847	0.54945		

1

***** convergence history for variable number 1

jmax	kmax	iter	rrms	rmax	mdot_err	t0ex	p0ex	imax
		1	5.01E-05	4.38E-01	0.09876	1.09198	1.55570	165
2	41	10	2.64E-05	1.65E-01	0.04257	1.12451	1.57642	91
10	12	20	1.99E-05	1.06E-01	0.00793	1.14001	1.57848	162
2	5	30	1.61E-05	1.01E-01	-0.03570	1.13991	1.58216	161
8	2	40	1.53E-05	6.83E-02	-0.07606	1.14243	1.58244	158
2	2	50	1.41E-05	8.50E-02	-0.12709	1.14477	1.58408	160
2	2	ÖÖÖÖ..						
30	32	2000	2.33E-08	2.87E-04	-0.00073	1.15491	1.59899	88

***** cpu time = 0.000 seconds

***** mass flow error (1-mdot_ex/mdot_in) = -0.00073

***** time step limit

cfl	dtmin	imin	jmin	kmin
5.000	2.11E-05	21	2	2

```

-----
theta-direction averaged quantities on inlet
derived variables, absolute system
approximate energy average
notation: rr=rho0ref, cr=c0ref, er=rr*cr**2, pr=p0ref,
tr=t0ref, alpha=atan(vth/u), phi=atan(vr/u)
-----

```

	k	distance	% mdot	vtot/cr	alpha	phi	ps/pr
p0/pr	ts/tr	t0/tr	Mach	ad.effic			
	1	0.20572	0.00000	0.51457	-90.00000	-88.00816	0.85924
1.03875	0.95069	1.00365	0.52775	0.00000			
	2	0.20574	-0.00001	0.45592	78.74520	28.19649	0.86076
0.99868	0.95843	1.00000	0.46570	0.00000			
	3	0.20576	-0.00001	0.31874	-79.39626	28.19973	0.88156
0.94723	0.97968	1.00000	0.32203	0.00000			
	4	0.20580	0.00002	0.27068	-54.85330	28.20066	0.89069
0.93792	0.98535	1.00000	0.27268	0.00000			
	5	0.20586	0.00008	0.28635	-42.24608	28.19919	0.88724
0.94010	0.98360	1.00000	0.28872	0.00000			
	6	0.20593	0.00018	0.30507	-32.11046	28.19683	0.88450
0.94462	0.98139	1.00000	0.30795	0.00000			
	7	0.20604	0.00035	0.32990	-22.73231	28.19233	0.88154
0.95213	0.97823	1.00000	0.33355	0.00000			
	8	0.20620	0.00063	0.36146	-13.64993	28.18539	0.87902
0.96438	0.97387	1.00000	0.36628	0.00000			
	9	0.20643	0.00109	0.39497	-5.26114	28.17407	0.87987
0.98311	0.96880	1.00000	0.40128	0.00000			
	10	0.20676	0.00181	0.42040	0.00000	28.15654	0.88165
1.00000	0.96465	1.00000	0.42803	0.00000			
	11	0.20723	0.00288	0.43113	0.00000	28.12954	0.87582
1.00000	0.96282	1.00000	0.43938	0.00000			
	12	0.20791	0.00444	0.43179	0.00000	28.08779	0.87546
1.00000	0.96271	1.00000	0.44007	0.00000			
	13	0.20887	0.00668	0.43098	0.00000	28.02304	0.87591
1.00000	0.96285	1.00000	0.43921	0.00000			
	14	0.21024	0.00989	0.43074	0.00000	27.92438	0.87604
1.00000	0.96289	1.00000	0.43896	0.00000			
	15	0.21219	0.01449	0.43093	0.00000	27.77480	0.87594
1.00000	0.96286	1.00000	0.43916	0.00000			
	16	0.21494	0.02105	0.43109	0.00000	27.54907	0.87585
1.00000	0.96283	1.00000	0.43933	0.00000			
	17	0.21878	0.03039	0.43105	0.00000	27.21214	0.87587
1.00000	0.96284	1.00000	0.43929	0.00000			
	18	0.22410	0.04363	0.43081	0.00000	26.71443	0.87600
1.00000	0.96288	1.00000	0.43903	0.00000			
	19	0.23135	0.06223	0.43059	0.00000	25.98974	0.87611
1.00000	0.96292	1.00000	0.43881	0.00000			
	20	0.24102	0.08808	0.43095	0.00000	24.95691	0.87592
0.99999	0.96286	1.00000	0.43918	0.00000			
	21	0.25357	0.12347	0.43242	0.00000	23.53522	0.87510
0.99999	0.96260	1.00000	0.44074	0.00000			

	22	0.26927	0.17080	0.43497	0.00000	21.66935	0.87369
0.99998	0.96216	1.00000	0.44344	0.00000			
	23	0.28805	0.23196	0.43771	0.00000	19.35690	0.87215
0.99996	0.96168	1.00000	0.44635	0.00000			
	24	0.30933	0.30732	0.43960	0.00000	16.67617	0.87108
0.99994	0.96135	1.00000	0.44835	0.00000			
	25	0.33203	0.39474	0.44035	0.00000	13.79533	0.87064
0.99991	0.96122	1.00000	0.44914	0.00000			
	26	0.35473	0.48940	0.44052	0.00000	10.94363	0.87050
0.99986	0.96119	1.00000	0.44933	0.00000			
	27	0.37601	0.58477	0.44082	0.00000	8.33513	0.87028
0.99980	0.96114	1.00000	0.44964	0.00000			
	28	0.39478	0.67430	0.44184	0.00000	6.11686	0.86963
0.99971	0.96095	1.00000	0.45073	0.00000			
	29	0.41047	0.75311	0.44384	0.00000	4.35130	0.86841
0.99960	0.96060	1.00000	0.45285	0.00000			
	30	0.42301	0.81877	0.44637	0.00000	3.01601	0.86690
0.99949	0.96015	1.00000	0.45554	0.00000			
	31	0.43268	0.87105	0.44770	0.00000	2.04724	0.86609
0.99943	0.95991	1.00000	0.45696	0.00000			
	32	0.43993	0.91098	0.44271	0.00000	1.36522	0.86682
0.99703	0.96080	1.00000	0.45165	0.00000			
	33	0.44525	0.93998	0.42551	0.00000	0.89781	0.86274
0.98162	0.96379	1.00000	0.43343	0.00000			
	34	0.44909	0.96003	0.40250	0.00000	0.58371	0.86093
0.96613	0.96760	1.00000	0.40919	0.00000			
	35	0.45184	0.97356	0.38080	0.00000	0.37511	0.86039
0.95374	0.97100	1.00000	0.38644	0.00000			
	36	0.45378	0.98261	0.36238	0.00000	0.23894	0.85997
0.94393	0.97374	1.00000	0.36724	0.00000			
	37	0.45515	0.98864	0.34641	0.00000	0.15020	0.85947
0.93574	0.97600	1.00000	0.35064	0.00000			
	38	0.45612	0.99265	0.33197	0.00000	0.09368	0.85886
0.92854	0.97796	1.00000	0.33569	0.00000			
	39	0.45679	0.99531	0.31858	0.00000	0.05784	0.85811
0.92197	0.97970	1.00000	0.32186	0.00000			
	40	0.45726	0.99705	0.30606	0.00000	0.03598	0.85719
0.91585	0.98127	1.00000	0.30897	0.00000			
	41	0.45759	0.99819	0.29438	0.00000	0.02220	0.85606
0.91008	0.98267	1.00000	0.29696	0.00000			
	42	0.45782	0.99893	0.28338	0.00000	0.01302	0.85476
0.90460	0.98394	1.00000	0.28569	0.00000			
	43	0.45798	0.99939	0.27222	0.00000	0.00739	0.85357
0.89937	0.98518	1.00000	0.27426	0.00000			
	44	0.45809	0.99967	0.25874	0.00000	0.00248	0.85313
0.89434	0.98661	1.00000	0.26049	0.00000			
	45	0.45816	0.99984	0.23564	0.00000	-0.00230	0.85534
0.88944	0.98890	1.00001	0.23696	0.00000			
	46	0.45822	0.99993	0.20221	0.00000	0.00193	0.85078
0.87559	0.99186	1.00004	0.20304	0.00000			
	47	0.45826	0.99998	0.15443	0.00000	0.01039	0.85412
0.86853	0.99540	1.00017	0.15479	0.00000			
	48	0.45829	1.00000	0.10123	0.00000	0.02536	0.86045
0.86665	0.99839	1.00044	0.10132	0.00000			
	49	0.45830	1.00000	0.00000	0.00000	0.00000	0.86291
0.86291	0.99965	0.99965	0.00000	0.00000			

```

----- overall averages -----
-----
50  0.35522  0.00906  0.43620  -0.45092  14.24261  0.87011
0.99665  0.96195  1.00000  0.44474  0.00000
-----

```

1

```

-----
theta-direction averaged quantities on inlet
derived variables, relative system
approximate energy average
notation: rr=rho0ref, cr=c0ref, er=rr*cr**2, pr=p0ref,
tr=t0ref, alpha=atan(vth/u), phi=atan(vr/u)
-----

```

p0/pr	k	distance	% mdot	vtot/cr	alpha	phi	ps/pr
	ts/tr	t0/tr	Mach				
	1	0.20572	0.00000	0.00000	89.72063	-88.00816	0.85924
0.85924	0.95069	0.95069	0.00000				
	2	0.20574	-0.00001	0.12180	-37.91501	28.19649	0.86076
0.87013	0.95843	0.96139	0.12441				
	3	0.20576	-0.00001	0.21225	73.85657	28.19973	0.88156
0.91027	0.97968	0.98869	0.21444				
	4	0.20580	0.00002	0.34619	63.76829	28.20066	0.89069
0.96886	0.98535	1.00932	0.34875				
	5	0.20586	0.00008	0.40263	59.52964	28.19919	0.88724
0.99389	0.98360	1.01602	0.40598				
	6	0.20593	0.00018	0.45331	57.29147	28.19683	0.88450
1.02107	0.98139	1.02248	0.45759				
	7	0.20604	0.00035	0.50576	55.71216	28.19233	0.88154
1.05373	0.97823	1.02939	0.51136				
	8	0.20620	0.00063	0.56366	54.64204	28.18539	0.87902
1.09667	0.97387	1.03741	0.57117				
	9	0.20643	0.00109	0.62339	54.32283	28.17407	0.87987
1.15271	0.96880	1.04652	0.63335				
	10	0.20676	0.00181	0.66570	54.31787	28.15654	0.88165
1.19925	0.96465	1.05328	0.67779				
	11	0.20723	0.00288	0.67345	53.68801	28.12954	0.87582
1.20024	0.96282	1.05353	0.68633				
	12	0.20791	0.00444	0.67520	53.72683	28.08779	0.87546
1.20167	0.96271	1.05389	0.68815				
	13	0.20887	0.00668	0.67658	53.89120	28.02304	0.87591
1.20372	0.96285	1.05440	0.68951				
	14	0.21024	0.00989	0.67915	54.06425	27.92438	0.87604
1.20666	0.96289	1.05514	0.69211				
	15	0.21219	0.01449	0.68313	54.27246	27.77480	0.87594
1.21088	0.96286	1.05619	0.69618				
	16	0.21494	0.02105	0.68872	54.56445	27.54907	0.87585
1.21693	0.96283	1.05770	0.70188				
	17	0.21878	0.03039	0.69642	54.97647	27.21214	0.87587
1.22557	0.96284	1.05984	0.70973				
	18	0.22410	0.04363	0.70706	55.53557	26.71443	0.87600
1.23788	0.96288	1.06287	0.72056				

	19	0.23135	0.06223	0.72181	56.25235	25.98974	0.87611
1.25530		0.96292	1.06712	0.73558			
	20	0.24102	0.08808	0.74215	57.11152	24.95691	0.87592
1.27973		0.96286	1.07301	0.75633			
	21	0.25357	0.12347	0.76952	58.08446	23.53522	0.87510
1.31352		0.96260	1.08104	0.78433			
	22	0.26927	0.17080	0.80469	59.15932	21.66935	0.87369
1.35927		0.96216	1.09167	0.82036			
	23	0.28805	0.23196	0.84725	60.34775	19.35690	0.87215
1.41936		0.96168	1.10525	0.86396			
	24	0.30933	0.30732	0.89562	61.64569	16.67617	0.87108
1.49502		0.96135	1.12178	0.91345			
	25	0.33203	0.39474	0.94743	62.98826	13.79533	0.87064
1.58532		0.96122	1.14074	0.96635			
	26	0.35473	0.48940	0.99973	64.26868	10.94363	0.87050
1.68638		0.96119	1.16108	1.01971			
	27	0.37601	0.58477	1.04940	65.39221	8.33513	0.87028
1.79176		0.96114	1.18138	1.07040			
	28	0.39478	0.67430	1.09392	66.29791	6.11686	0.86963
1.89397		0.96095	1.20029	1.11592			
	29	0.41047	0.75311	1.13182	66.97140	4.35130	0.86841
1.98653		0.96060	1.21680	1.15479			
	30	0.42301	0.81877	1.16256	67.44952	3.01601	0.86690
2.06547		0.96015	1.23046	1.18644			
	31	0.43268	0.87105	1.18608	67.83606	2.04724	0.86609
2.12952		0.95991	1.24127	1.21059			
	32	0.43993	0.91098	1.20150	68.38454	1.36522	0.86682
2.17428		0.96080	1.24952	1.22577			
	33	0.44525	0.93998	1.20805	69.37853	0.89781	0.86274
2.17772		0.96379	1.25566	1.23054			
	34	0.44909	0.96003	1.20944	70.56205	0.58371	0.86093
2.17024		0.96760	1.26015	1.22952			
	35	0.45184	0.97356	1.20907	71.64255	0.37511	0.86039
2.16164		0.97100	1.26337	1.22699			
	36	0.45378	0.98261	1.20815	72.54569	0.23894	0.85997
2.15304		0.97374	1.26566	1.22434			
	37	0.45515	0.98864	1.20682	73.31906	0.15020	0.85947
2.14396		0.97600	1.26728	1.22157			
	38	0.45612	0.99265	1.20513	74.01011	0.09368	0.85886
2.13416		0.97796	1.26843	1.21863			
	39	0.45679	0.99531	1.20317	74.64587	0.05784	0.85811
2.12374		0.97970	1.26922	1.21557			
	40	0.45726	0.99705	1.20108	75.23698	0.03598	0.85719
2.11289		0.98127	1.26978	1.21249			
	41	0.45759	0.99819	1.19897	75.78699	0.02220	0.85606
2.10184		0.98267	1.27017	1.20950			
	42	0.45782	0.99893	1.19688	76.30418	0.01302	0.85476
2.09075		0.98394	1.27044	1.20661			
	43	0.45798	0.99939	1.19469	76.82886	0.00739	0.85357
2.07975		0.98518	1.27063	1.20364			
	44	0.45809	0.99967	1.19196	77.46318	0.00248	0.85313
2.06886		0.98661	1.27077	1.20002			
	45	0.45816	0.99984	1.18736	78.55329	-0.00230	0.85534
2.05803		0.98890	1.27086	1.19400			
	46	0.45822	0.99993	1.18131	80.14370	0.00193	0.85078
2.02629		0.99186	1.27096	1.18615			

	47	0.45826	0.99998	1.17417	82.44238	0.01039	0.85412
2.01001		0.99540	1.27113	1.17688			
	48	0.45829	1.00000	1.16844	85.02962	0.02536	0.86045
2.00544		0.99839	1.27144	1.16938			
	49	0.45830	1.00000	1.16408	90.00000	0.00000	0.86291
1.99807		0.99965	1.27067	1.16428			
	----- overall averages -----						
	50	0.35522	0.00906	1.00124	64.86833	14.24261	0.87011
1.68789		0.96195	1.16244	1.02085			

1

theta-direction averaged quantities on exit
derived variables, absolute system
approximate energy average
notation: rr=rho0ref, cr=c0ref, er=rr*cr**2, pr=p0ref,
tr=t0ref, alpha=atan(vth/u), phi=atan(vr/u)

	k	distance	% mdot	vtot/cr	alpha	phi	ps/pr
p0/pr	ts/tr	t0/tr	Mach	ad.effic			
	1	0.30384	0.00000	0.77208	-90.00000	-89.99994	1.19000
1.69441	1.12221	1.24143	0.72883	0.67352			
	2	0.30386	0.00001	0.73625	-84.53786	3.26619	1.19004
1.64594	1.11658	1.22499	0.69675	0.68007			
	3	0.30389	0.00004	0.71002	-78.83150	3.32580	1.19011
1.61194	1.11345	1.21428	0.67287	0.68207			
	4	0.30392	0.00010	0.69519	-73.92559	3.36751	1.19019
1.59444	1.10931	1.20597	0.66005	0.69226			
	5	0.30397	0.00021	0.68849	-70.25256	3.39254	1.19030
1.58761	1.10528	1.20009	0.65488	0.70561			
	6	0.30404	0.00039	0.68594	-67.42542	3.42889	1.19044
1.58597	1.10171	1.19581	0.65351	0.71931			
	7	0.30414	0.00068	0.68560	-65.04169	3.46420	1.19063
1.58714	1.09831	1.19232	0.65420	0.73360			
	8	0.30428	0.00112	0.68676	-62.79453	3.51209	1.19089
1.59036	1.09486	1.18919	0.65633	0.74923			
	9	0.30447	0.00179	0.68937	-60.41085	3.57491	1.19125
1.59581	1.09091	1.18595	0.66003	0.76828			
	10	0.30474	0.00282	0.69364	-57.73210	3.66468	1.19172
1.60403	1.08612	1.18234	0.66558	0.79269			
	11	0.30511	0.00439	0.69939	-54.77619	3.78876	1.19236
1.61501	1.08033	1.17816	0.67289	0.82383			
	12	0.30564	0.00680	0.70560	-51.74591	3.95255	1.19321
1.62744	1.07386	1.17344	0.68091	0.86079			
	13	0.30637	0.01043	0.71028	-49.00186	4.14799	1.19432
1.63828	1.06761	1.16851	0.68742	0.89889			
	14	0.30738	0.01578	0.71136	-46.86214	4.36538	1.19577
1.64408	1.06271	1.16392	0.69005	0.93117			
	15	0.30879	0.02345	0.70802	-45.42669	4.60134	1.19766
1.64336	1.05976	1.16001	0.68777	0.95299			

	16	0.31072	0.03420	0.70085	-44.56911	4.85960	1.20011
1.63723	1.05861	1.15684	0.68117	0.96441			
	17	0.31335	0.04894	0.69115	-44.06244	5.14202	1.20328
1.62815	1.05870	1.15424	0.67172	0.96887			
	18	0.31689	0.06883	0.68026	-43.69400	5.42956	1.20731
1.61851	1.05952	1.15207	0.66088	0.96986			
	19	0.32158	0.09526	0.66923	-43.30764	5.67932	1.21237
1.61008	1.06083	1.15041	0.64975	0.96921			
	20	0.32767	0.12979	0.65883	-42.80621	5.86198	1.21853
1.60406	1.06247	1.14928	0.63917	0.96834			
	21	0.33536	0.17395	0.64933	-42.16441	5.96499	1.22581
1.60077	1.06425	1.14858	0.62943	0.96836			
	22	0.34475	0.22892	0.64035	-41.42308	5.94477	1.23406
1.59942	1.06631	1.14832	0.62012	0.96819			
	23	0.35576	0.29503	0.63153	-40.62338	5.79998	1.24297
1.59912	1.06868	1.14844	0.61090	0.96696			
	24	0.36805	0.37118	0.62284	-39.80742	5.52936	1.25210
1.59929	1.07122	1.14880	0.60178	0.96486			
	25	0.38107	0.45470	0.61432	-39.03746	5.12910	1.26093
1.59933	1.07390	1.14937	0.59281	0.96124			
	26	0.39408	0.54143	0.60630	-38.34595	4.63337	1.26901
1.59912	1.07657	1.15009	0.58435	0.95638			
	27	0.40637	0.62653	0.59929	-37.77372	4.09863	1.27605
1.59888	1.07916	1.15099	0.57689	0.95034			
	28	0.41738	0.70538	0.59363	-37.40078	3.60337	1.28194
1.59880	1.08192	1.15240	0.57071	0.94142			
	29	0.42678	0.77449	0.58941	-37.35455	3.22991	1.28672
1.59886	1.08529	1.15477	0.56578	0.92709			
	30	0.43447	0.83205	0.58623	-37.76700	3.00870	1.29055
1.59857	1.08990	1.15864	0.56153	0.90413			
	31	0.44056	0.87782	0.58372	-38.66699	2.93353	1.29359
1.59767	1.09598	1.16413	0.55758	0.87277			
	32	0.44525	0.91282	0.58141	-39.94696	2.84844	1.29598
1.59596	1.10304	1.17065	0.55359	0.83735			
	33	0.44879	0.93877	0.57825	-41.42296	2.58634	1.29785
1.59262	1.11051	1.17739	0.54872	0.80168			
	34	0.45142	0.95756	0.57291	-42.90383	2.11006	1.29929
1.58650	1.11793	1.18358	0.54185	0.76782			
	35	0.45335	0.97089	0.56404	-44.23384	1.52557	1.30036
1.57653	1.12483	1.18846	0.53182	0.73703			
	36	0.45476	0.98022	0.55062	-45.31963	1.05000	1.30113
1.56214	1.13079	1.19143	0.51780	0.71005			
	37	0.45578	0.98666	0.53245	-46.13267	0.76914	1.30168
1.54373	1.13550	1.19220	0.49968	0.68721			
	38	0.45651	0.99108	0.51035	-46.68137	0.62674	1.30204
1.52269	1.13882	1.19091	0.47824	0.66865			
	39	0.45703	0.99409	0.48562	-46.98079	0.61278	1.30229
1.50068	1.14079	1.18796	0.45467	0.65425			
	40	0.45741	0.99613	0.45938	-47.05117	0.64154	1.30245
1.47891	1.14161	1.18381	0.42994	0.64355			
	41	0.45768	0.99751	0.43199	-46.93207	0.66607	1.30255
1.45780	1.14154	1.17886	0.40433	0.63571			
	42	0.45787	0.99844	0.40293	-46.68052	0.67480	1.30261
1.43705	1.14088	1.17335	0.37724	0.62966			
	43	0.45801	0.99905	0.37074	-46.34990	0.66577	1.30265
1.41595	1.13987	1.16736	0.34725	0.62427			

	44	0.45810	0.99946	0.33285	-45.97926	0.64196	1.30267
1.39357	1.13863	1.16079	0.31193	0.61858			
	45	0.45817	0.99971	0.28581	-45.59280	0.60914	1.30268
1.36937	1.13719	1.15353	0.26802	0.61207			
	46	0.45822	0.99987	0.22660	-45.20857	0.58041	1.30269
1.34439	1.13547	1.14574	0.21265	0.60542			
	47	0.45826	0.99995	0.15527	-44.84594	0.56488	1.30269
1.32219	1.13341	1.13823	0.14584	0.60093			
	48	0.45829	0.99999	0.07774	-44.53096	0.56083	1.30269
1.30757	1.13143	1.13263	0.07308	0.60038			
	49	0.45830	1.00000	0.00000	0.00000	0.00000	1.30269
1.30269	1.13275	1.13275	0.00000	0.59119			

----- overall averages -----

	50	0.38882	0.00907	0.61729	-40.42720	4.71076	1.25916
1.59899	1.07870	1.15491	0.59434	0.92643			

1

theta-direction averaged quantities on exit

derived variables, relative system

approximate energy average

notation: rr=rho0ref, cr=c0ref, er=rr*cr**2, pr=p0ref,
tr=t0ref, alpha=atan(vth/u), phi=atan(vr/u)

p0/pr	k	distance	% mdot	vtot/cr	alpha	phi	ps/pr
	ts/tr	t0/tr	Mach				
	1	0.30384	0.00000	0.00043	-89.99999	-89.99994	1.19000
1.19000	1.12221	1.12221	0.00040				
	2	0.30386	0.00001	0.08055	29.40941	3.26619	1.19004
1.19489	1.11658	1.11788	0.07623				
	3	0.30389	0.00004	0.15747	29.02394	3.32580	1.19011
1.20877	1.11345	1.11841	0.14923				
	4	0.30392	0.00010	0.21960	28.64588	3.36751	1.19019
1.22681	1.10931	1.11895	0.20850				
	5	0.30397	0.00021	0.26457	28.32641	3.39254	1.19030
1.24391	1.10528	1.11928	0.25166				
	6	0.30404	0.00039	0.29870	28.04660	3.42889	1.19044
1.25930	1.10171	1.11955	0.28458				
	7	0.30414	0.00068	0.32737	27.78958	3.46420	1.19063
1.27396	1.09831	1.11975	0.31238				
	8	0.30428	0.00112	0.35449	27.54193	3.51209	1.19089
1.28935	1.09486	1.12000	0.33878				
	9	0.30447	0.00179	0.38347	27.30064	3.57491	1.19125
1.30749	1.09091	1.12032	0.36715				
	10	0.30474	0.00282	0.41642	27.09776	3.66468	1.19172
1.33031	1.08612	1.12080	0.39957				
	11	0.30511	0.00439	0.45327	27.01892	3.78876	1.19236
1.35878	1.08033	1.12142	0.43609				
	12	0.30564	0.00680	0.49158	27.17959	3.95255	1.19321
1.39198	1.07386	1.12219	0.47437				

	13	0.30637	0.01043	0.52659	27.66360	4.14799	1.19432
1.42594	1.06761	1.12307	0.50965				
	14	0.30738	0.01578	0.55387	28.48264	4.36538	1.19577
1.45534	1.06271	1.12406	0.53728				
	15	0.30879	0.02345	0.57196	29.59894	4.60134	1.19766
1.47705	1.05976	1.12518	0.55560				
	16	0.31072	0.03420	0.58281	30.97500	4.85960	1.20011
1.49198	1.05861	1.12654	0.56644				
	17	0.31335	0.04894	0.58996	32.59510	5.14202	1.20328
1.50370	1.05870	1.12831	0.57337				
	18	0.31689	0.06883	0.59687	34.44785	5.42956	1.20731
1.51617	1.05952	1.13077	0.57986				
	19	0.32158	0.09526	0.60619	36.50470	5.67932	1.21237
1.53269	1.06083	1.13433	0.58856				
	20	0.32767	0.12979	0.61974	38.71963	5.86198	1.21853
1.55577	1.06247	1.13928	0.60125				
	21	0.33536	0.17395	0.63831	41.05375	5.96499	1.22581
1.58697	1.06425	1.14574	0.61875				
	22	0.34475	0.22892	0.66171	43.48964	5.94477	1.23406
1.62670	1.06631	1.15388	0.64080				
	23	0.35576	0.29503	0.68949	45.98344	5.79998	1.24297
1.67500	1.06868	1.16376	0.66697				
	24	0.36805	0.37118	0.72078	48.44361	5.52936	1.25210
1.73124	1.07122	1.17512	0.69641				
	25	0.38107	0.45470	0.75389	50.77121	5.12910	1.26093
1.79319	1.07390	1.18757	0.72749				
	26	0.39408	0.54143	0.78704	52.86593	4.63337	1.26901
1.85794	1.07657	1.20045	0.75854				
	27	0.40637	0.62653	0.81822	54.65438	4.09863	1.27605
1.92155	1.07916	1.21306	0.78764				
	28	0.41738	0.70538	0.84526	56.11245	3.60337	1.28194
1.97891	1.08192	1.22482	0.81262				
	29	0.42678	0.77449	0.86593	57.26380	3.22991	1.28672
2.02406	1.08529	1.23526	0.83121				
	30	0.43447	0.83205	0.87851	58.17978	3.00870	1.29055
2.05165	1.08990	1.24426	0.84149				
	31	0.44056	0.87782	0.88289	58.93644	2.93353	1.29359
2.06041	1.09598	1.25188	0.84334				
	32	0.44525	0.91282	0.88067	59.60746	2.84844	1.29598
2.05400	1.10304	1.25816	0.83853				
	33	0.44879	0.93877	0.87436	60.28106	2.58634	1.29785
2.03846	1.11051	1.26341	0.82971				
	34	0.45142	0.95756	0.86671	61.04679	2.11006	1.29929
2.02009	1.11793	1.26817	0.81972				
	35	0.45335	0.97089	0.86029	61.98390	1.52557	1.30036
2.00437	1.12483	1.27285	0.81115				
	36	0.45476	0.98022	0.85704	63.14535	1.05000	1.30113
1.99516	1.13079	1.27769	0.80595				
	37	0.45578	0.98666	0.85795	64.52814	0.76914	1.30168
1.99436	1.13550	1.28271	0.80513				
	38	0.45651	0.99108	0.86307	66.06685	0.62674	1.30204
2.00218	1.13882	1.28780	0.80876				
	39	0.45703	0.99409	0.87188	67.66674	0.61278	1.30229
2.01779	1.14079	1.29282	0.81630				
	40	0.45741	0.99613	0.88359	69.25406	0.64154	1.30245
2.03996	1.14161	1.29775	0.82697				

	41	0.45768	0.99751	0.89754	70.81252	0.66607	1.30255
2.06765	1.14154	1.30266	0.84006				
	42	0.45787	0.99844	0.91346	72.38483	0.67480	1.30261
2.10050	1.14088	1.30776	0.85520				
	43	0.45801	0.99905	0.93170	74.05852	0.66577	1.30265
2.13953	1.13987	1.31348	0.87267				
	44	0.45810	0.99946	0.95349	75.96132	0.64196	1.30267
2.18792	1.13863	1.32046	0.89356				
	45	0.45817	0.99971	0.98093	78.23614	0.60914	1.30268
2.25157	1.13719	1.32964	0.91986				
	46	0.45822	0.99987	1.01639	80.96326	0.58041	1.30269
2.33856	1.13547	1.34208	0.95383				
	47	0.45826	0.99995	1.06081	84.04350	0.56488	1.30269
2.45565	1.13341	1.35847	0.99643				
	48	0.45829	0.99999	1.11132	87.14172	0.56083	1.30269
2.60014	1.13143	1.37843	1.04478				
	49	0.45830	1.00000	1.16408	90.00000	0.00000	1.30269
2.75997	1.13275	1.40376	1.09375				
	----- overall averages -----						
	50	0.38882	0.00907	0.76355	52.04857	4.71076	1.25916
1.80344	1.07870	1.19530	0.73517				

***** restart file written on unit 3 *****

APPENDIX G. COMPUTER PROGRAMS

1. BLADE-3D Executable

```
#include <iostream.h>
#include <iomanip.h>

#include "surface.h"
#include "bsurface.h"
#include "matrix.h"
#include "blade.h"

main()
{
    int a,b,c,d;
    //int e;
    float f,g;
    //float j,k;
    cin >> a >> b >> c >> d;
    //cin >> e;
    cin >> f >> g;
    //cin >> h >> i;
    //cin >> j >> k;
    blade sangl(a,b,c,d);
    sangl.readBsurf_2();
    //sangl.subdl(0,h,i);
    //sangl.subdt(0,.005,.005);
    //sangl.subdl(1,h,i);
    //sangl.subdt(1,.003,.007);
    //sangl.subdl(2,h,i);
    //sangl.subdt(2,.002,.008);
    //sangl.subdl(3,h,i);
    //sangl.subdt(3,.002,.008);
    sangl.lete(f,g);
    //cout << a << "    " << b << "    " << c << "    " << d << endl;
    //cout << e << endl;
    //cout << f << "    " << g << endl;
    //cout << h << "    " << i << endl;
    //cout << j << "    " << k << endl;
    //sangl.output_f();
    sangl.print();

    return 0;
}
```

2. RANDCP, a program to produce random control point variations

```

      INTEGER NSPAN, NPOINT, NLE, NTE
      REAL LE, TE, XT, YT, RAND
      REAL X(32), Y(32), Z(32), XL(32), XU(32), YL(32),
      YU(32), E1(32), E2(32)
      REAL X1L(16), X1U(16), Y1L(32), Y1U(32), F1(16), F2(16),
      XR(32), YR(32)
      INTEGER X2L(16), X2U(16), Y2L(32), Y2U(32), XN(16), YN(32),
      YB(32)
      OPEN (UNIT = 14, FILE = 'kfile', STATUS = 'OLD')
      READ *, NSPAN, NPOINT, NLE, NTE
      READ *, LE, TE
      DO 10 I=1,32
        READ *, X(I), Y(I), Z(I)
10      CONTINUE
      XT = .117 * .05
      YT = .05 * .05
      DO 70 I=6,7
        XL(I) = X(I) - XT
        XU(I) = X(I) + XT
        YL(I) = Y(I) - YT
        YU(I) = Y(I) + YT
70      CONTINUE
      DO 80 I=10,11
        XL(I) = X(I) - XT
        XU(I) = X(I) + XT
        YL(I) = Y(I) - YT
        YU(I) = Y(I) + YT
80      CONTINUE
      READ (14,*), K
130     DO 110 I=6,7
        X1L(I) = 1/XL(I)
        X1U(I) = 1/XU(I)
        F1(I) = X1U(I)-X1L(I)
        F2(I) = 10/F1(I)
        X2L(I) = INT(X1L(I)*F2(I))
        X2U(I) = INT(X1U(I)*F2(I))
        XN(I) = ABS(X2L(I)) - INT(RAND(K))
120      IF (XN(I).LE.ABS(X2U(I))) THEN
        XN(I) = XN(I) + INT(RAND(K))
        GO TO 120
      END IF
      IF (X2U(I).LT.0) THEN
        XN(I) = -XN(I)
      END IF
      XR(I) = XN(I)/F2(I)
      XR(I) = 1/XR(I)
      Y1L(I) = 1/YL(I)
      Y1U(I) = 1/YU(I)
      E1(I) = ABS(Y1U(I)-Y1L(I))

```

```

      E2(I) = 10/E1(I)
      Y2L(I) = INT(Y1L(I)*E2(I))
      Y2U(I) = INT(Y1U(J)*E2(I))
121  IF (Y2L(I).LT.0) THEN
      YN(I) = Y2L(I) + INT(RAND(K))
      END IF
      IF (Y2L(I).GT.0) THEN
      YN(I) = Y2L(I) - INT(RAND(K))
      END IF
      IF (YN(I).EQ.0) THEN
      GO TO 121
      END IF
      YR(I) = YN(I)/E2(I)
      YR(I) = 1/YR(I)
110  CONTINUE
      IF (XR(7).GT.XR(6)) THEN
      GO TO 130
      END IF
170  DO 140 I=10,11
      X1L(I) = 1/XL(I)
      X1U(I) = 1/XU(I)
      F1(I) = X1U(I)-X1L(I)
      F2(I) = 10/F1(I)
      X2L(I) = INT(X1L(I)*F2(I))
      X2U(I) = INT(X1U(I)*F2(I))
      XN(I) = ABS(X2L(I)) - INT(RAND(K))
150  IF (XN(I).LE.ABS(X2U(I))) THEN
      XN(I) = XN(I) + INT(RAND(K))
      GO TO 150
      END IF
      IF (X2U(I).LT.0) THEN
      XN(I) = -XN(I)
      END IF
      XR(I) = XN(I)/F2(I)
      XR(I) = 1/XR(I)
      Y1L(I) = 1/YL(I)
      Y1U(I) = 1/YU(I)
      E1(I) = ABS(Y1U(I)-Y1L(I))
      E2(I) = 10/E1(I)
      Y2L(I) = INT(Y1L(I)*E2(I))
      Y2U(I) = INT(Y1U(J)*E2(I))
160  IF (Y2L(I).LT.0) THEN
      YN(I) = Y2L(I) + INT(RAND(K))
      END IF
      IF (Y2L(I).GT.0) THEN
      YN(I) = Y2L(I) - INT(RAND(K))
      END IF
      IF (YN(I).EQ.0) THEN
      GO TO 160
      END IF
      YR(I) = YN(I)/E2(I)
      YR(I) = 1/YR(I)
140  CONTINUE
      IF (XR(11).GT.XR(10)) THEN
      GO TO 170
      END IF

```

```

DO 180 I=6,7
    X(I) = XR(I)
    Y(I) = YR(I)
180    CONTINUE
DO 190 I=10,11
    X(I) = XR(I)
    Y(I) = YR(I)
190    CONTINUE
    WRITE (16,30), NSPAN, NPOINT, NLE, NTE
    WRITE (16,50), LE, TE
    DO 100 I=1,32
        WRITE (16, 90), X(I), Y(I), Z(I)
100    CONTINUE
30    FORMAT (I2,I5,I5,I5)
40    FORMAT (I1)
50    FORMAT (F6.4,F7.4)
60    FORMAT (F12.10,F15.10,F15.10)
90    FORMAT (3F15.10, 2I8)
END

*****
*****
*****

FUNCTION RAND(K)

INTEGER K, M, CONST1
REAL G, CONST2, RAND
PARAMETER (CONST1=2147483647, CONST2=.4656613E-9)
SAVE
DATA M /0/

IF (M.EQ.0) M=K
M=M*65539
IF (M.LT.0) M=(M+1)+CONST1
G=M*CONST2
G=1000*G
10  IF (G.GT.10) THEN
    G=G/10
    GO TO 10
END IF
RAND=G
END

```

3. BPARAM, a program to calculate blade design parameters

```

INTEGER NSPAN, NPOINT, NBLADE, LOC, LOC2
REALX(11,147),Y(11,147), Z(11,147),GAMMA(11), CA1, CA2,
PHI(11), TH(74)
REAL CHORD, MIN, MAX, D1, D2, D3, D4, D5, D6, I25, I50, I75,
D25, D50, D75

```

```

REAL CA, S0IN, S0OUT, S25IN, S25OUT, S50IN, S50OUT, S75IN,
S75OUT, POUT
REAL S100IN, S100OUT, I0, D0, I100, D100, TA1, TA2, TA, MA,
PIN, TOUT
REAL PR, EF, MD, PEF, A
READ *, NSPAN, NPOINT, NBLADE
READ *, S0IN, S25IN, S50IN, S75IN, S100IN
READ *, S0OUT, S25OUT, S50OUT, S75OUT, S100OUT
READ *, MA, PIN, TOUT, POUT
DO 10 I=1, 11
  READ *, (X(I,J), J=1,NPOINT)
  READ *, (Y(I,J), J=1,NPOINT)
  READ *, (Z(I,J), J=1,NPOINT)
  XBAR = X(I,147)-X(I,76)
  ZBAR = Z(I,147)-Z(I,76)
  CHORD = SQRT(XBAR*XBAR+ZBAR*ZBAR)
  D2 = SIN(Y(I,147))*Z(I,147)
  D1 = SIN(Y(I,76))*Z(I,76)
  GAM = ATAN((D2-D1)/CHORD)
  GAMMA(I) = GAM/2/3.14159*360
  D4 = SIN(Y(I,57))*Z(I,57)
  D3 = SIN(Y(I,64))*Z(I,64)
  CA1 = ATAN((D4-D3)/(X(I,57)-X(I,64)))
  CA1 = CA1/2/3.14159*360
  D6 = SIN(Y(I,96))*Z(I,96)
  D5 = SIN(Y(I,89))*Z(I,89)
  CA2 = ATAN((D6-D5)/(X(I,96)-X(I,89)))
  CA2 = CA2/2/3.14159*360
  CA = (CA1+CA2)/2
  D4 = SIN(Y(I,16))*Z(I,16)
  D3 = SIN(Y(I,9))*Z(I,9)
  TA1 = ATAN((D4-D3)/(X(I,16)-X(I,9)))
  TA1 = TA1/2/3.14159*360
  D6 = SIN(Y(I,132))*Z(I,132)
  D5 = SIN(Y(I,139))*Z(I,139)
  TA2 = ATAN((D6-D5)/(X(I,132)-X(I,139)))
  TA2 = TA2/2/3.14159*360
  TA = (TA1+TA2)/2
  PHI(I) = CA - TA
  DO 40 K=1, (NPOINT+1)/2
    TH(K) = (SIN(Y(I,NPOINT-K+1))*Z(I,NPOINT-K+1)
#      -SIN(Y(I,K))*Z(I,K))*12
40  CONTINUE
    MIN = 1
    DO 50 L=5, (NPOINT-9)/2
      IF (TH(L).LT.MIN) THEN
        MIN = TH(L)
        LOC = L
      END IF
50  CONTINUE
    MAX = 0
    DO 80 M=5, (NPOINT-9)/2
      IF (TH(M).GT.MAX) THEN
        MAX = TH(M)
        LOC2 = M
      END IF

```

```

80          CONTINUE
          WRITE (*,70), GAMMA(I), PHI(I)
10  CONTINUE
70  FORMAT(F10.3, F10.3, F15.8, I8, F15.8, I8)
      WRITE *, ' '
      WRITE *, ' '
      WRITE *, ' Incidence Angle', ' Deviation Angle'
      I0 = S0IN-((PHI(1)/2)+GAMMA(1))
      D0 = -(S0IN-S0OUT)+PHI(1)+I0
      WRITE (*,90), I0, D0
      I25 = S25IN-((PHI(3)/2)+GAMMA(3))
      D25 = -(S25IN-S25OUT)+PHI(3)+I25
      WRITE (*,90), I25, D25
      I50 = S50IN-((PHI(6)/2)+GAMMA(6))
      D50 = -(S50IN-S50OUT)+PHI(6)+I50
      WRITE (*,90), I50, D50
      I75 = S75IN-((PHI(9)/2)+GAMMA(9))
      D75 = -(S75IN-S75OUT)+PHI(9)+I75
      WRITE (*,90), I75, D75
      I100 = S100IN-((PHI(11)/2)+GAMMA(11))
      D100 = -(S100IN-S100OUT)+PHI(11)+I100
      WRITE (*,90), I100, D100
      WRITE *, ' '
      WRITE *, ' '
      WRITE *, ' '
      WRITE *, ' '
      PR = POUT/PIN
      A = .4/1.4
      EF = ((PR**A)-1)/(TOUT-1)
      MD = (((MA**2)*.4/2)+1)**-3)*MA*159.563
      PEF = (LOG(PR)*.4)/(LOG(TOUT)*1.4)
      WRITE *, 'Pressure Ratio: ', PR
      WRITE *, 'Efficiency: ', EF
      WRITE *, 'Mass Flow Rate: ', MD
      WRITE *, 'Polytropic Efficiency: ', PEF
90  FORMAT (F15.3, F20.3)
      END

```

4. CNODE, a program to calculate the closest finite element node

```

      REAL X(308), Y(308), Z(308), A(9000), B(9000), C(9000)
      REAL F(9000), G(9000), H(9000), K(9000)
      INTEGER NODE(9000), MNODE
      DO 10 I=1,308
          READ (10,*), X(I), Y(I), Z(I)
10  CONTINUE
      DO 20 J=1,4177
          READ (20,60), NODE(J), A(J), B(J), C(J)
20  CONTINUE

```

```

DO 30 I=1,308
  D=10
  DO 40 J=1,4177
    F(J)=ABS(A(J)-X(I))
    G(J)=ABS(B(J)-Y(I))
    H(J)=ABS(C(J)-Z(I))
    K(J)=SQRT(F(J)**2+G(J)**2+H(J)**2)
    IF (K(J).LT.D) THEN
      MNODE=NODE(J)
      D=K(J)
    END IF
  40 CONTINUE
  WRITE (30,50), X(I), Y(I), Z(I), MNODE
30 CONTINUE
50 FORMAT (3F12.8, I6)
60 FORMAT (I4, 3F12.8)
END

```

5. DGEOM, a program to calculate deflected geometry and new cold shape

```

REAL X(308), Y(308), Z(308), E(308), F(308), G(308)
INTEGER MNODE(308)
DO 20 I=1,308
  READ (50,*), X(I), Y(I), Z(I), MNODE(I), E(I), F(I),
    G(I)
20 CONTINUE
DO 30 I=1,308
  WRITE (60,40), X(I)+E(I), Y(I)+F(I), Z(I)+G(I)
30 CONTINUE
DO 80 I=1,154
  WRITE(80,70),
    (X(I)+E(I))/12,(Y(I)+F(I))/12,(Z(I)+G(I))/12,
#    (X(I+154)+E(I+154))/12, (Y(I+154)+F(I+154))/12,
#    (Z(I+154)+G(I+154))/12
80 CONTINUE
DO 50 I=1,308
  READ (10,*), X(I), Y(I), Z(I)
  WRITE (70,40), X(I)-E(I), Y(I)-F(I), Z(I)-G(I)
50 CONTINUE
DO 60 I=1,154
  WRITE (*,70),
    (X(I)-E(I))/12,(Y(I)-F(I))/12,(Z(I)-G(I))/12,
#    (X(I+154)-E(I+154))/12, (Y(I+154)-F(I+154))/12,
#    (Z(I+154)-G(I+154))/12
60 CONTINUE
40 FORMAT (3F11.6)
70 FORMAT (6F10.6)
END

```


LIST OF REFERENCES

1. Abdelhamid, Hazem. F., Incorporation of Sweep in a Transonic Fan Design Using a 3-D Blade-Row Geometry Package Intended for Aero-Structural-Manufacturing Optimization, PhD Dissertation, Naval Postgraduate School, 1997
2. Sanger, Nelson. L., Design of a Low Aspect Ratio Transonic Compressor Stage Using CFD Techniques, Journal of Turbomachinery #118, pp.479-491, 1996
3. Sanger, Nelson L., Design Methodology for the NPS Transonic Compressor, TPL Technical Note 99-01, 1999
4. Wennerstrom, Arthur. J., Design of Highly Loaded Axial-Flow Fans and Compressors, Concepts ETI, Inc., 2000
5. Wu, C. H., A General Theory of Three-Dimensional Flow In Subsonic and Supersonic Turbomachines of Axial-, Radial-, and Mixed-Flow Types, NACA TN 2604, 1952
6. Koch, C. C. and L. H. Smith, Jr., Loss Sources and Magnitudes in Axial Flow Compressors, Journal of Engineering for Power #98, pp. 411-422, 1976
7. Miller, G. R., G. W. Lewis, Jr., and M. J. Hartmann, Shock Losses in Transonic Compressor Blade Rows, Journal of Engineering for Power #83, pp. 235-242, 1961
8. Wennerstrom, A. J. and S. L. Puterbaugh, A Three-Dimensional Model for the Prediction of Shock Losses in Compressor Blade Rows, Journal of Engineering for Gas Turbines and Power #106, pp. 552-560, 1984
9. Vavra, Michael. H., Aero-thermodynamics and Flow in Turbomachines, Robert E. Krieger Publishing Co., Inc. 1974

10. Smith, L. H., Jr., The Radial Equilibrium Equation of Turbomachinery, ASME Journal of Engineering for Power, pp. 1-12, Jan. 1966
11. Silvester, M. E. and R. Hetherington, Three-Dimensional Compressible Flow Through Axial-Flow Turbomachines, *Numerical Analysis – An Introduction*, edited by J. Walsh, Ch. II, Pt. III, pp. 182-189, 1966
12. Wennerstrom, Arthur J., On the Treatment of Body Forces in the Radial Equilibrium Equation of Turbomachinery, Traupel Festschrift, Juris-Verlag, pp.351-357, 1974
13. Jennions, I. K., and P. Stow, A Quasi-Three-Dimensional Turbomachinery Blade Design System, Journal of Engineering for Gas Turbines and Power #107, pp. 301-307, 1985
14. Johnsen, I. A. and R. O. Bullock, eds., Aerodynamic Design of Axial-Flow Compressors, NASA SP-36, 1965
15. Crouse, J. E., D. C. Janetzke, and R. E. Schwirian, A Computer Program for Composing Compressor Blading from Simulated Circular-Arc Elements on Conical Surfaces, NASA Technical Note D-5437, 1969
16. Crouse, J. E. and W. T. Gorrell, Computer Program for Aerodynamic Blading Design of Multistage Axial-Flow Compressors, NASA Technical Paper 1946, 1981
17. Denton, John. D., Designing in Three Dimensions, AGARD Lecture Series #195, 1994
18. Neubert, R. J., D. E. Hobbs, and H. D. Weingold, Application of Sweep to Improve the Efficiency of a Transonic Fan, Journal of Propulsion and Power #11-1, pp. 49-54, 1995
19. Puterbaugh, S. L., W. W. Copenhaver, C. Hah, and A. J. Wennerstrom, A Three-Dimensional Shock Loss Model Applied to an Aft-Swept Transonic Compressor Rotor, Journal of Turbomachinery #119-3, pp. 452-459, 1997

20. Law, C. H. and A. R. Wadia, Low Aspect Ratio Transonic Fan Rotors: Part I – Baseline Design and Performance, Journal of Turbomachinery #115, pp. 218-225, 1993
21. Wadia, A. R., P. N. Szucs, and D. W. Crall, Inner Workings of Aerodynamic Sweep, Journal of Turbomachinery #120-4, pp. 671-682, 1998
22. Verhoff, A., J. Shim, J. Chung, and K. D. Lee, Aerodynamic Design of Cascade Blades Using Asymptotic Solution of Euler Equations, AIAA Paper 2002-0102, Presented at the 40th Aerospace Sciences Meeting and Exhibit - Reno, Nevada, January 2002
23. Chung, J., J. Shim, and K. D. Lee, Design of 3-D Transonic Compressor Blades Using Numerical Optimization, AIAA Paper 2000-0227, Presented at the 38th Aerospace Sciences Meeting and Exhibit – Reno, Nevada, January 2000
24. Chung J., J. Shim, and K. D. Lee, Inverse Design of 3-D Transonic Compressor Blades Using 3-D Navier-Stokes Flow Physics, AIAA Paper 2002-0103, Presented at the 40th Aerospace Sciences Meeting and Exhibit - Reno, Nevada, January 2002
25. Demeulenaere, A. and R. Van Den Braembussche, Three-Dimensional Inverse Method for Turbomachinery Blading Design, Journal of Turbomachinery #120, pp. 247-255, 1998
26. Damle, S. , T. Dang, J. Stringham, and E. Razinsky, Practical Use of Three-Dimensional Inverse Method for Compressor Blade Design, Journal of Turbomachinery #121-2, pp. 321-325, 1999
27. Dornburger, R., D. Buche, and P. Stoll, Multidisciplinary Optimization in Turbomachinery Design, Technical Paper presented at the European Congress on Computational Methods in Applied Sciences and Engineering (ECCOMAS 2000) – Barcelona, Spain, September 2000
28. Farin, Gerald, Curves and Surfaces for Computer Aided Geometric Design: A Practical Guide, Academic Press, 1993

29. Grossman, B. L., Testing and Analysis of a Transonic Axial Compressor, Master's Thesis, Naval Postgraduate School, 1997
30. O'Brien, J. M., Transonic Compressor Test Rig Rebuild and Initial Results with Sanger Stage, Master's Thesis, Naval Postgraduate School, 2000
31. Reid, W. D., Transonic Axial Compressor Design Case Study and Preparations for Testing, Master's Thesis, Naval Postgraduate School, 1995
32. Von Backstrom, T. W., G. V. Hobson, B. L. Grossman, and R. P. Shreeve, Investigation of the Performance of a CFD-Designed Transonic Compressor Stage, AIAA Paper 2000-3205, Presented at the 36th AIAA/ASME/ASEE Joint Propulsion Conference – Huntsville, Alabama, July 2000
33. Chima, Roderick V., TCGRID 3-D Grid Generator for Turbomachinery – User's Manual and Documentation, NASA Lewis Research Center, 1996
34. Sorenson, R. L., A Computer Program to Generate Two-Dimensional Grids About Airfoils and Other Shapes by Use of Poisson's Equation, NASA TM-81198, 1980.
35. Chima, R. V., and J. W. Yokota, Numerical Analysis of Three-Dimensional Viscous Flows in Turbomachinery, AIAA Journal #28-5, pp. 798-806, 1990
36. Chima, Roderick V., Viscous Three-Dimensional Calculations of Transonic Fan Performance, NASA TM-103800, 1991
37. Chima, Roderick V., RVC3D – Rotor Viscous Code 3-D – User's Manual and Documentation, NASA Lewis Research Center, 1992
38. Initial Graphics Exchange Specification 5.3, 1996

39. Lawry, Mark H., I-DEAS Master Series Six – Student Guide, Structural Dynamics Research Corporation, 1999
40. Davis, Stephen R., C++ - Weekend Crash Course, IDG Books Worldwide, Inc., 2000
41. Hermann, Tony, Analysis and Design of the Rotor, Stator, and Nose Cone for the Naval Postgraduate School Transonic Compressor, NASA Lewis Research Center (Internal), 1994
42. Strasizar, A. and M. Ernst, NASA Glenn Research Center, Personal Communication, November 2001
43. Platzer, M. F. and F. O. Carta, eds., AGARD Manual on Aeroelasticity in Axial-Flow Turbomachines, Vols. I and II, AGARD, 1987
44. Panovsky, J., M. A. Bahkle, and R. Srivastava, Flutter Characteristics of a Forward-swept Fan, Technical Paper presented at the 7th National Turbine Engine High Cycle Fatigue Conference, FT Lauderdale, FL, May 2002
45. Vanderplaats, Garrett N., Numerical Optimization Techniques for Engineering Design with Applications, McGraw-Hill Book Company, 1984
46. Conley, William, Optimization: A Simplified Approach, Petrocelli Books, Inc., 1981

INITIAL DISTRIBUTION LIST

1. Defense Technical Information Center
Ft. Belvoir, Virginia
2. Dudley Knox Library
Naval Postgraduate School
Monterey, CA
3. Chairman and Distinguished Professor Max F. Platzer, Code AA/PL
Department of Aeronautics and Astronautics
Naval Postgraduate School
Monterey, CA
4. Professor R. P. Shreeve, Code AA/Sf
Department of Aeronautics & Astronautics
Naval Postgraduate School
Monterey, CA
5. Professor Garth V. Hobson, Code AA/Hg
Department of Aeronautics and Astronautics
Naval Postgraduate School
Monterey, CA
6. Assoc. Professor Richard. M. Howard, Code AA/Ho
Department of Aeronautics and Astronautics
Naval Postgraduate School
Monterey, CA
7. Assoc. Professor Carlos Borges, Code MA/Bc
Department of Applied Mathematics
Naval Postgraduate School
Monterey, CA
8. Professor John Denton
Whittle Laboratory
Cambridge UK
9. Aspi R. Wadia
GE Aircraft Engines
Cincinnati, OH

10. Nicholas Cumpsty
Rolls Royce
Derby UK
11. Arthur J. Wennerstrom
Hot Springs Village, AR
12. Naval Air Warfare Center – Aircraft Division
Propulsion & Power Engineering
ATTN: M. Klein, Code 4.4.7.1, BLDG 106
Patuxent River, MD
13. Naval Air Warfare Center – Aircraft Division
Propulsion & Power Engineering
ATTN: C. Gorton, Code 4.4T, BLDG 106
Patuxent River, MD
14. NASA Glenn Research Center
[ATTN: Tony Strazisar, MS 5-11]
Cleveland, OH
15. NASA Glenn Research Center
[ATTN: R. V. Chima, MS 77-61]
Cleveland, OH
16. NASA Glenn Research Center
[ATTN: Chunill Hah, MS 5-11]
Cleveland, OH
17. Mr. Nelson Sanger
Rocky River, OH
18. CDR James A. Jones, Jr., USN
Annapolis, MD